Late Glacial and Holocene Palaeolake History of the Última Esperanza Region of Southern Patagonia

Stephen J. Roberts[1*], Robert D. McCulloch[2], Joseph F. Emmings[3], Sarah J. Davies[4], Wim Van Nieuwenhuyze[5], Mieke Sterken[5], Katrien Heirman[6], Jeroen Van Wichelen[5,7], Carolina Diaz[8], Evelien Van de Vyver[5,9], Alex Whittle[1], Wim Vyverman[5], Dominic A. Hodgson[1], Elie Verleyen[5]

[1]British Antarctic Survey, Natural Environment Research Council, High Cross, Madingley Road, Cambridge, CB3 0ET, UK.
[2]Centro de Investigación en Ecosistemas de la Patagonia (CIEP), Coyhaique, Chile.
[3]British Geological Survey, Keyworth, Nottingham, NG12 5GG, UK.
[4]Department of Geography and Earth Sciences, Aberystwyth University, Aberystwyth, SY23 3DB, UK.
[5]Protistology and Aquatic Ecology, Ghent University, Krijgslaan 281 S8, 9000 Gent, Belgium.
[6]TNO - Geological Survey of the Netherlands, Princetonlaan 6, NL-3584 CB Utrecht, Netherlands.
[7]Research Institute for Nature and Forest, Herman Teirlinckgebouw, Havenlaan 88 bus 73, 1000 Brussels, Belgium.
[8]Institute of Ecology and Biodiversity (IEB), Universidad de Chile, Las Palmeras 3425, Casilla 653, Santiago, Chile.
[9]Flanders Environment Agency Dokter De Moorstraat 24-26 9300 Aalst Belgium

*** Corresponding author:** Stephen J. Roberts sjro@bas.ac.uk ORCiD: 0000-0003-3407-9127

This is a post print version of a manuscript published in Frontiers in Earth Science as part of the Glaciation and Climate Change in the Andean Cordillera Research Topic. It has been revised after review and accepted for publication. Subsequent versions of this manuscript may differ due to the editorial process. The final version is available via the peer-reviewed publication doi link on EarthArXiv and here: https://doi.org/10.3389/feart.2022.813396.

We welcome all comments and feedback, either posted on EarthArXiv or sent directly to the first/corresponding author, Stephen Roberts (sjro@bas.ac.uk).

Abstract

We undertook multiproxy analyses on two sediment cores from Lago Pato, a small lake basin at 51°S topographically separated from Lago del Toro in Torres del Paine (TdP), to provide insights into glacier dynamics and lake level change in the TdP and Última Esperanza region over the last ~30,000 cal a BP (30 ka). Lago Pato is situated in a region overridden by the Southern Patagonian Icefield during the Last Glacial and in a transitional climatic zone of Southern Patagonia sensitive to seasonal- to millennial-scale changes in the Southern Hemisphere Westerly winds (SWW). Results show that a deep ice dammed and enlarged palaeolake encompassed Lago del Toro and Lago Pato c. 30–20 ka, after ice had retreated from local-Last Glacial Maximum (l-LGM) limits at c. 48–34 ka, and during the build-up to the global-Last Glacial Maximum (g-LGM), c. 26–19 ka. Gaps in both sediment records between c. 20–13.4 ka and c. 20–10 ka suggest hiatuses in sediment accumulation during the g-LGM and Antarctic Cold Reversal (ACR) readvances and/or removal by lake lowering or flushing during the Late glacial–early Holocene. The palaeolake level dropped from >100 m a.s.l. to ~40–50 m a.s.l. towards the end of the ACR c. 13.4–13.0 ka, creating a shallower glaciolacustrine environment dammed by an ice tongue in the Estancia Puerto Consuelo–Última Esperanza fjord. Further lowering of the enlarged palaeolake level occurred when the ice thinned to <40 m a.s.l., eventually isolating Lago Pato from Lago del Toro and glaciogenic sediment input at c. 11.7 ka. After isolation, the ecology and water levels in Lago Pato became sensitive to regional climate shifts. The shallow, stable, and highly anoxic environment that developed after c. 11.7 ka is associated with weaker (or poleward shifted) SWW at 51°S and was replaced at c. 10 ka by an increasingly productive shallow-littoral lake with a variable lake-level and periodic shifts in anoxic-oxic bottom water conditions and ratios of benthic-planktonic diatoms. A more open *Nothofagus* forest, established at c. 8.6–7.5 ka, and more arid conditions c. 7.5–5.7 cal ka BP are linked to another phase of weaker (or poleward shifted) SWW at 51°S. More persistently wet conditions from c. 5.7 ka, with extensive closed *Nothofagus* forests and planktonic diatoms dominant, are associated with stronger (or equatorward shifted) SWW over 51°S. The abrupt return of benthic-to-tychoplanktonic diatoms after c. 3 ka reflects enhanced SWW at 51°S. Increasingly stable lacustrine and littoral wetland conditions established in the last ~500 years reflect weaker SWW and lasted until recent decades.

Keywords: Last Glacial Maximum (LGM), palaeoclimate, palaeolimnology, glaciation, lake level changes, Patagonia, Southern Hemisphere Westerly Winds.

1. Introduction

The Southern Patagonian Ice Sheet reached its local Last Glacial Maximum (l-LGM) at c. 48 ka (48,000 calibrated (cal) years before present (BP), where present is 1950 CE), during Marine Isotope Stage 3 (MIS 3) (Figure 1), with secondary readvances at c. 39 ka and 34 ka (García et al., 2018). Outlet glaciers extended offshore to the west onto the continental shelf of the Pacific, and crossed eastwards into Argentina and eastern valleys and fjords of the Última Esperanza province. Ice lobes from the Cordillera Paine extended out beyond the eastern end of Lago del Toro forming complex terminal moraine systems, scouring deep lake basins such as Lago del Toro while reaching their maximum advance limits at the l-LGM (limit A_1 in Figure 2A) (Sagredo et al., 2011; García et al., 2012; García et al., 2014; García et al., 2018; Davies et al., 2020). At the global Last Glacial Maximum (g-LGM), c. 26.5–19 ka, the Southern Patagonian Ice Sheet was more than 200 km wide and over 1800 km long, yet reached only half its maximum Marine Isotope Stage 3 extent due to milder winters and drier conditions associated with a weaker, broader and equatorward shifted Southern Westerly wind belt that extended into the mid-latitudes (McCulloch and Davies, 2001; Kaplan et al., 2007; Kaplan et al., 2008; García et al., 2014; Darvill et al., 2015; Glasser et al., 2017; García et al., 2018; Davies et al., 2020; McCulloch et al., 2020).

The Southern Hemisphere Westerly winds (SWW) are one of the main drivers of the global climate system, regulating the capacity of the Southern Ocean to absorb or release CO_2 through diffusion and biological uptake at the surface (Hodgson and Sime, 2010; Marshall and Speer, 2012) (Figure 1A). Recent global warming is thought to have led to an intensification and/or poleward shift in the mean annual position of the core SWW belt, and this is either reducing (Le Quere et al., 2007) or increasing (Landschützer et al., 2016) the capacity of surface waters in the Southern Ocean to absorb atmospheric CO_2. The 'reducing hypothesis' is supported by recent observational and palaeo data, which shows a substantial rise in CO_2 during the transition into the Holocene coincident with increased ventilation of carbon from the deep Southern Ocean (Moreno et al., 2010; Fletcher and Moreno, 2012; Saunders et al., 2018), rising global sea levels (Spratt and Lisiecki, 2016), and rapid deglaciation of the South Patagonian Icefield (Davies et al., 2020; Palacios et al., 2020).

Dating of moraines and shorelines, changes in basin topography (García et al., 2012; García et al., 2014; García et al., 2018), multi-proxy, isotopic and pollen analysis of lake and marine sediment records (Huber et al., 2004; Fletcher and Moreno, 2012; Mayr et al., 2013; Zolitschka et al., 2013; Moreno et al., 2018; McCulloch et al., 2020; Moreno et al., 2021) and larger-scale regional data compilations (Glasser et al., 2008; Davies et al., 2020; Palacios et al., 2020) have been used to reconstruct past glacier extent and deglaciation in Patagonia (Figure 3), with many studies linking glacier advance and retreat to past changes in precipitation and SWW intensity and/or latitudinal position over Southern South America (Figure 1).

The Seno Última Esperanza province and the Parque Nacional Torres del Paine has a wide variety of outstanding glacial geomorphological features. Many palaeoenvironmental studies have also been undertaken in the region (Figure 1, 3), but the timing, impact and drivers of Late glacial and Holocene deglaciation remains debated (Moreno et al., 2018; Davies et al., 2020). The lake level history of Lago del Toro and the Holocene vegetational history of the surrounding area is detailed and well-studied (see Figure 3, ref. nos. 7–15 for summary) (García et al., 2012; Solari et al., 2012; García et al., 2014; García et al., 2018; Moreno et al., 2018; Moreno et al., 2021). A large ice-dammed proglacial lake, palaeo-Lago Tehuelche, once covered Lago del Toro and Lago Sarmiento sometime after c. 38 ka but before c. 17.6–16.8 ka; i.e., between the l-LGM and g-LGM (Sagredo et al., 2011; Moreno et al., 2012; García et al., 2014). After the g-LGM, another large ice-dammed palaeolake encompassed Lago del Toro as far south as the southern end of the

Puerto Consuelo–Última Esperanza fjord between c. 18–10.2 ka (but possibly as late as c. 7.1 ka) (locations B_1, B_2 in Figure 2A; Figure 3 reference numbers 7–10). This palaeolake has been associated with local glacier readvance stages B–D (Stage TDP-I–IV), phases of ice retreat linked with Meltwater Pulse 1A c. 14.7 ka, and following readvances during the Antarctic Cold Reversal (ACR: 14.5–12.9 ka; Blunier et al. (1997)) (García et al., 2012; Solari et al., 2012; García et al., 2014; Davies et al., 2020).

Moraines along the northern shoreline of Lago del Toro with maximum cosmogenic isotope ages of c. 24 ka, have been linked to the g-LGM advance, while ages of c. 14.5-12.5 ka from the innermost moraines to the north of Lago Sarmiento imply ice could have also readvanced to the eastern end of Lago del Toro during the ACR (García et al., 2014; Fogwill and Kubik, 2016; García et al., 2018). No post LGM chronology has been established for these moraines or those along the southern margin of Lago del Toro, adjacent to Lago Pato (Figure 2A, B). Glacier advances were driven by the alignment of the SWW over 51–52°S, which persisted between c. 13.4–11.3 ka as ACR glaciers retreated, but then became weaker, more diffuse or poleward shifted during the 'Early Holocene Westerlies Minimum' (Mayr et al., 2013; Quade and Kaplan, 2017; Moreno et al., 2018; Zolitschka et al., 2018; McCulloch et al., 2020; Moreno et al., 2021).

To better understand changes in regional glacier dynamics and the nature and timing of climate changes, including the impact of changing SWW intensity over 51°S during the Late glacial and Holocene, we present new data from two sediment records extracted from Lago Pato (S51°18.020', W72°40.716').

Lago Pato is a small, low altitude basin at 30–35 m a.s.l. located outside, but immediately adjacent to, moraines that run along the southern shoreline of Lago del Toro. It is located approximately mid-way between l-LGM and g-LGM maxima and present-day ice limits, and in a transitional climatic zone east of the Andes (Figure 1, 2). Previous studies and new geomorphological mapping of the area (Figure 2) show that Lago Pato would have been joined to Lago del Toro when lake levels were >40–50 m a.s.l. Using new geomorphological information collected in the field with high-resolution multi-proxy sedimentology and geochemistry (supported by fossil pollen and diatom evidence) from sediment records extracted from the present-day depocentre and a former littoral part of the basin within the catchment area of Lago Pato, we examine how regional deglaciation of the Última Esperanza region drove (palaeo)lake level change within TdP. More specifically, we test the hypothesis that Lago Pato became isolated from Lago del Toro and glaciogenic sediment input when lake levels fell below the retaining sill following deglaciation and sometime after the Antarctic Cold Reversal (ACR: c. 14.6–12.8 ka). As Lago Pato is located within a transitional climatic zone east of the Andes, we also examine how deglaciation and isolation relate to broader climate changes during the Late glacial and Holocene, in particular the variability of the SWW over ~51°S (and southern South America). Our key findings are summarised in Figure 3 (reference no. 15) within the context of the existing glacial and climatic history of Southern Patagonia (reference nos. 1–14)

2. Site Description and Background

Lago Pato is a relatively shallow (~4 m deep), well-mixed ellipsoidal freshwater lake, covering an area of approximately 35,000 m² (~250 x 130 m). It is located just outside the Parque Nacional Torres del Paine and on the eastern slopes of the Andes, on the southern shore of Lago del Toro (Figure 2). Both lakes are located to the east of the southern margin of the Southern Patagonian Icefield and have been overridden and influenced by past glacial advances from the Cordillera Paine massif (Figure 2A).

Several outlet glaciers feed rivers that flow into Lago del Toro, but Lago Pato, at ~33 m a.s.l. is currently an isolated and closed basin system, with no direct glacial meltwater input. It is separated from the glaciolacustrine-influenced Lago del Toro, at 25 m a.s.l., by low-lying ridges at ~25–34 m a.s.l. to the south and east and elevated moraines, at ~ 38 m a.s.l., immediately to the north, northeast and northwest (Figure 2B–D; Table 1). Former shorelines are clearly visible on the adjacent moraines and in the surrounding area on satellite imagery and are marked in the field by notable changes in catchment vegetation cover from grassland to dwarf shrubs (Figure 2B–D). Presently, the lake level in Lago del Toro is between 10–15 m below Lago Pato, depending on seasonal meltwater inputs into Lago del Toro (Figure 2B).

Lago Pato is located ~4–5 degrees south of the region offshore in the Pacific Ocean where the present day Antarctic Circumpolar Current (ACC) splits into equator- and pole-ward flows (Lamy et al., 2010; Caniupán et al., 2017), making it particularly sensitive to regional and spatial variations in the SWW-driven precipitation-evaporation balance over the Andes (Figure 4). Following the post-glacial isolation, Lago Pato would have been a small, responsive lake located at the boundary with the eastern forest-steppe ecotone, and in a transitional climatic zone between 'wet' western and 'dry' eastern Patagonia. Our working hypothesis was that even relatively small changes in wind-driven precipitation in the past led to significant changes in lake level, lake ecology and catchment vegetation cover.

2.1 Climate

Climate data from the Administración PN Torres del Paine Meteorological Station ~25 km from Lago Pato is characterised by a mean annual air temperature of 7.3°C (1964–2011 CE, three years after the LP08 core was taken), with minimum and maximum monthly averages of 3.6°C (in 1976 CE) and 9.1°C (in 1983 CE), a mean annual precipitation of 817 mm a^{-1} and mean annual wind speed (at ground level) of 24 km h^{-1}, predominantly from the W and NW (data from http://www.meteochile.gob.cl). In comparison, the mean annual precipitation along the west coast of Chilean Patagonia and western Andes is up to 7000 mm a^{-1}, but declines to 400 mm a^{-1} on the eastern steppe (Schneider et al., 2013). Temperature and precipitation anomaly profiles for TdP between 1979–2021 CE (compared to the 30-year mean between 1980–2010 CE) are shown in Figure 4A.

The Andean Cordillera creates an orographic barrier to the SWW (currently focussed at ~50–52°S), and a complex spatial (latitudinal) and temporal relationship between wind strength and precipitation (Figure 1C–D, 4B–I). Analysis of weather station data has shown that annual precipitation immediately east of the Andes, around Lago del Toro and Lago Pato was neutral to slightly positively correlated to zonal wind flow over the high Andes (U on P at 850 mbar) over the last ~40 years (Garreaud et al., 2013; Schneider et al., 2013; Moreno et al., 2018). Studies combining weather station data and mesoscale modelling of the eastern Andean slopes have shown a more consistently positive correlation (Moreno et al., 2014; Moreno et al., 2018). Seasonally, there is only marginally more precipitation in the Última Esperanza region compared to winter (June-July-August; JJA) (Figure 4B, D), but the core SWW are stronger and more poleward shifted (south of 50–52°S) over Southern Patagonia during the Austral summer (December-January-February; DJF; Figure 4C, E). Consequently, zonal winds over the Andes have had a consistently neutral to negative correlation with precipitation at Lago Pato between 1979–2017 CE during the Austral summer, and this relationship has become more negative over the last decade (2007–2017 CE; Figure 4F, G). In contrast, during winter, zonal winds over the Andes and precipitation over Lago Pato have been positively correlated over the last decade (Figure 4H), leading to a net neutral to negative annual correlation between precipitation and wind velocity (Figure 4I). At Lago Potrok Aike, ~175 km ESE of Lago Pato at 51°S, where the orographic effect of the Andes is reduced, easterly frontal system incursions are more prevalent, and winter precipitation can also increase when the SWW become weaker and/or when its core

belt widens latitudinally (Garreaud et al., 2009; Fletcher and Moreno, 2012; Zolitschka et al., 2013).

Regionally, longer term changes in climate are controlled by the interplay between the changing strength and influence of interannual–millennial scale climate drivers, such as the El Niño Southern Oscillation (ENSO) and the Southern Annular Mode (SAM), defined as the atmospheric pressure difference between the mid and high latitudes in the Southern Hemisphere (Garreaud et al., 2013). Decadal scale variability in precipitation and temperature is evident in the TdP reanalysis data (Figure 4A). Positive phases of the SAM reflect warmer and drier conditions and higher pressure in the mid latitudes (e.g., Patagonia) with lower pressures and stronger and more poleward shifted SWW (Marshall, 2003; 2007). In essence, the situation is analogous to the seasonal Westerlies (summer/winter) cycle in that the SWW are more intense and focused during positive (warmer) phases of the SAM (the current situation) and weaker, latitudinally broader and less focussed during negative (colder) phases of the SAM (Perren et al., 2020).

Warming in recent decades has led to an increasingly positive Southern Annular Mode and a greater influence of the El Nino Southern Oscillation (Marshall, 2003; Abram et al., 2014), with reduced precipitation and weaker Southern Westerlies in the high to mid latitudes of southern South America (Garreaud et al., 2009). Similar processes are thought to occur over decadal–centennial and longer timescales, with an equatorward core SWW belt maintaining high lake levels in northern and eastern Patagonia between c. 51 ka and 9 ka (Zolitschka et al., 2013; Van Daele et al., 2016; Henríquez et al., 2021). Millennial-scale periodicities recorded in various proxy records are thought to be driven by changes in insolation and solar activity (e.g., the ~2.4–2.5 kyr Hallstatt cycle (Viaggi, 2021)), the planetary radiative imbalance (i.e., the amount of insolation absorbed versus the energy radiated back into space at the top of the atmosphere), internal ice sheet dynamics, and CO_2 outgassing, driven largely by changes in the SWW (Emile-Geay et al., 2007; Steinhilber et al., 2009; Baggenstos et al., 2019; Dickens et al., 2019; Henríquez et al., 2021; Shin et al., 2021; Evans et al., 2022).

2.2 Vegetation and Geology

Vegetation patterns in Southern Patagonia closely follow the sharp west-to-east precipitation gradient across the Andes, superimposed on latitudinal variations (Tuhkanen, 1992). As moisture-laden air masses cross the Andes, the hyper-humid region in the west transitions into a more arid steppe in the east. The western side of the Andes is dominated by Magellanic moorland communities and evergreen *Nothofagus* forests (southern beech), while the eastern slopes, and those close to the Patagonian icefield, are characterized by winter deciduous *Nothofagus* forests. The wider Provincia de Última Esperanza is a diverse eco-climatic region from hyper humid in the west and arid in the east. Southern beech forests occur in western regions with an annual precipitation between ~450–1000 mm a^{-1}, gradually merge into a transition zone of dry scrub and fescue grassland in regions with precipitation regimes below ~450 mm a^{-1}, and finally become Patagonian steppe in drier eastern areas(Tuhkanen, 1992). Lago Pato is located just outside the Parque Nacional Torres del Paine, in the Comuna de Torres del Paine. As part of the Región de Magallanes, it is in an ecological transition zone between the *Nothofagus* dominated and steppe biomes, although the natural vegetation has been altered by agricultural and land management activity in and around Parque Nacional Torres del Paine and Lago Pato. The local geology is dominated by shales, intercalated by marls, sandstones and conglomerates (Altenberger et al., 2003). The glaciated landscape of the Southern Patagonian Ice Sheet dominates the southern Andes and the Cordillera Paine massif to the west and northwest of Lago Pato.

3. Methods

3.1 Geomorphology and limnology

We measured the geoid-corrected elevation above sea level (m a.s.l.) of former lake shorelines and retaining moraine ridges around Lago Pato using a Trimble differential GPS (dGPS) accurate to down to 0.1 m with values quoted as ± 2-sigma errors (Table 1). Other elevations were determined from 'Google Earth', and are on average, 6.7 ± 5.9 m (2-sigma) higher than the geoid-corrected dGPS field measurements; hence, we assigned ± 10 m errors. Standard limnological properties (pH, conductivity, temperature, dissolved oxygen) were measured in and around Lago Pato and other Southern Patagonian lakes with a YSI600 Sonde. Light penetration was measured with a Secchi disc and water samples for diatom and chemical analysis were taken at one metre intervals in the water column.

3.2 Sedimentology, Geochemistry and Chronology

Using a combination of a UWITEC-gravity corer, a Livingston piston corer and a Russian corer, two sediment records were extracted from the deepest point (~3.5 m of water depth) in the lake – the 600 cm long LP08 record (S51° 18'01.2'', W72° 40'43.0'', 32 m a.s.l.) – and from a littoral wetland area – the 295 cm long LP16 record (S51°18'11.3'', W72° 40'53.7'', 33–34 m a.s.l.) (Figure 2A, Table 1). A surface gravity core from the LP08 site was sliced at 0.5 cm (0–20 cm) and 1 cm (20–41 cm) intervals in the field. Livingston piston cores (LP08) and Russian cores (LP16) were retained intact.

Intact cores were split in the laboratory and analysed for physical properties with a Geotek® multi-sensor core logger (MSCL) (Gunn and Best, 1998) to obtain gamma-ray wet density (ɣ-density or GRD), resistivity and magnetic susceptibility (MSκ; SIx10^{-5}) data (Bartington Instruments; LP08: MS2C loop sensor, 2 mm intervals, 10 seconds; LP16: MS2E point sensor, 0.5 mm intervals; 10 seconds) and density-corrected MSχ (κ/ρ; kg m^{-3}). Digital X-radiographs were obtained from split cores using a rotating anode mobile digital Celtic SMR CR computerised X radiography unit at Cambridge University Vet School (48kV; 4 mAs; no grid) and as ITRAX™ digital X-radiographs (45 kV, 50 mA.ms, 200 ms, 60 μm interval) at Aberystwyth University. Contiguous downcore wet-sediment Energy Dispersive Spectrometry (EDS) X-ray fluorescence core scanning (XRF-CS) geochemistry data was obtained using the ITRAX™ XRF core scanner fitted with a Molybdenum (Mo) anode X-ray tube (settings: 30 kV, 50 mA, count time 10 seconds). Machine and sample calibration was undertaken using a synthetic glass standard and XRF fused glass discs from the Ardley Lake and Yanou Lake sediment cores (Roberts et al., 2017) with similar compositional variability at the start and end of each core-site run. Measurements were made at 2 mm contiguous intervals for LP08 (equivalent to mean ± 2-sigma: 4.5 ± 7.0 years), with duplicate scans undertaken at 200 μm intervals for LP08 Unit 1 (1.3 ± 4.2 years) and at 100 μm for the basal LP08 Unit 1 core section. LP16 Units 3-6 were scanned at 500 μm (9.6 ± 17.4 years) and LP16 Units 1-2 at 200 μm (1.1 ± 1.6 years). Data from finely laminated glaciolacustrine sediments in Units 1-2 were measured at, or smoothed to, 200 μm (from 100 μm interval data) before analysis.

Raw count per second (cps) XRF-CS data were analysed using the Q-spec software v8.6.0 (Cox Analytical), with MSE values minimised to optimise the fit of 'as measured' spectra to modelled spectra. Element and scatter cps were normalised by total scatter cps (incoherent (Compton) scatter + coherent (Rayleigh) scatter; inc.+coh.) as element/inc.+coh. (Kylander et al., 2011). Data are presented as percentages of the Total Scatter Normalised ratio sum (%∑TSN or, more simply, %TSN (Roberts et al., 2017)), equivalent to percentages of the cps sum (or %cps), to account for downcore variations in count rate, density, water and organic content and to investigate covariance, closed-sum effects between elements and scatter parameters, and the non-stationarity and equifinality of geochemical responses through time (Tjallingii et al., 2007). Data less than mean minus two-sigma kcps (mainly due to gaps in the core) and greater than MSE plus two-sigma (representing a poor fit between measured to modelled spectra) were filtered before analysis. 'Noisy' and poorly measured elements were eliminated by comparing cps and using

%TSN thresholds of >0.1% mean and >0.5% maximum, and by examining autocorrelation profiles for each element (Bishop, 2021). This left 12 'well measured' elements for the LP08 record (Si, S ,K, Ca, Ti, Mn, Fe, Zn, Br, Rb, Sr, Zr, and inc., coh. scatter) and 17 'well measured' elements for the LP16 record (Si , S, K, Ca, Ti, V, Cr, Mn, Fe, Ni, Zn, As, Br, Rb, Sr, Zr , Ba, and inc., coh. scatter) (see Supplementary Methods for details).

Centred element log ratios (clr) and log element ratios of XRF-CS can produce similar downcore profiles to quantitative (Wavelength Dispersive Spectroscopy, WDS-XRF) analysis of dry and organic free samples (Weltje and Tjallingii, 2008; Davies et al., 2015; Roberts et al., 2017; Dunlea et al., 2020). Therefore, key elements used in interpretations (S, Ca, Ti, Mn, Fe, Br, Sr) are presented as natural log (i.e., log-n or Ln) ratios of cps data or their Z-scores (i.e., centred around the mean, and standardised by subtracting the mean from observed values and dividing by the 1σ). As Al is not well-measured using an ITRAX^{TM} XRF core scanner with a Mo-tube (Löwemark et al., 2011), Ti-normalised log-n ratios were used to estimate elemental variations relative to the background bedrock input (Weltje and Tjallingii, 2008; Kylander et al., 2011; Davies et al., 2015; Roberts et al., 2017; Saunders et al., 2018).

Core sections were aligned into composite records from field depth measurements from visual stratigraphy, bulk density, MS, XRF-CS data, and, for LP08, subsample data (Loss-on-ignition (LOI), and total organic carbon (TOC)) and by using AnalySeries (Paillard et al., 1996).

A chronology for each record was established using Accelerator Mass Spectrometry (AMS) radiocarbon dating of 21 samples from the LP08 record and 15 samples from the LP16 record. Identifiable macrofossils were dated preferentially, but where bulk samples were the only option, we avoided intervals likely to contain significant authigenic carbonate, characterised by exceptionally elevated Ca, Sr and/or Mn in XRF-CS profiles. Calibration of radiocarbon ages was undertaken in OXCAL v.4.4 (Bronk Ramsey, 2016) using the SHCal20.14C Southern Hemisphere atmosphere calibration dataset (Hogg et al., 2016; Hogg et al., 2020)). Radiocarbon ages are reported as conventional radiocarbon years BP (^{14}C years BP) ± 1σ and calibrated ages as 2σ (95.4%) ranges, median and mean calendar years BP (cal a BP and cal ka BP, relative to 1950 CE), rounded to the nearest ten years. Age-depth models for both records were developed using Bayesian age-depth modelling software (BACON v.2.5) (Blaauw and Christen, 2011), incorporating a hiatus of 10,000 years at 470 cm in LP08 and 7,000 years at 110 cm in LP16 between Unit 1 and its overlying deposits (Figure S1) (see Supplementary Materials for details). Ages are rounded to the nearest 10 calendar years (cal a BP) in the results section, and to the nearest 100 years (0.1 cal ka BP) in the discussion, to reflect dating and age-depth modelling uncertainties.

Units with common characteristics were identified using constrained CONISS cluster analysis with broken stick on square root transformed 2 mm and 1 cm interval smoothed %TSN XRF-CS geochemical data, and as measured 1 cm interval diatom and pollen datasets. To establish provenance relationships, the Pearson product-moment correlation coefficient (PPMCC), multivariate principal components analysis (PCA), which reduces correlations between elements to the smallest set of linear combinations possible plotted on dimensionless axes, and discriminant hierarchical (k-means) cluster analysis, which uses a measure of statistical distance (dissimilarity) between multiple elements to generate groups, were applied to 12 'measurable' elements common to LP08 and LP16 (Si, S ,K, Ca, Ti, Mn, Fe, Zn, Br, Rb, Sr, Zr) and incoherent, coherent scatter parameters. Measured %TSN data were log transformed, centred and standardised as Z-scores prior to PCA.

Log-n element/Ti ratio XRF-CS Z-scores were used for time series analysis (Fast Fourier Transform, FFT, periodograms, Lomb-Scargle Power Spectrum, Wavelet Power Spectrum, Peak

Identification using MATLAB; Figure 6, S6) (Grinsted et al., 2004; Trauth, 2015). Equally spaced (10-year and 100-year) time-intervals were generated for time series analysis using Piecewise Cubic Hermite Interpolated Polynomial (PCHIP) datasets, which avoids spline artefacts and preserve the shape of the original XRF-CS data series. Time series data were detrended (polynomial linear best fit) to remove the long-term linear trend. Second order polynomial Locally Weighted Scatterplot Smoothing (LOESS) 100-year smoothing (0.1 sampling interval with outliers removed) was also used to compare datasets to published data.

3.3 Carbon, Diatom, and Pollen analysis

Geochemical and sedimentological interpretations of lake level change in Lago Pato were inferred from multi-proxy analysis of the <10 cal ka BP organic deposits of Unit 6 in the LP08 record. This part of the LP08 was more highly resolved than the LP16 Holocene record and contained sufficient diatoms and pollen for quantitative analysis. Loss-on-ignition (LOI) (12 hrs drying at 110°C, 4 hrs at 550°C (LOI_{550}), and 2 hrs at 950°C for carbonate-proxy (LOI_{950}x1.36) (Heiri et al., 2001)), Total Organic Carbon (TOC, $\%C_{org}$) and total nitrogen (%N) were determined at 1 cm and 4 cm intervals in the LP08 core. Bulk organic carbon isotopic ratios ($\delta^{13}C_{org}$), determined by combustion on a Costech EA interfaced with the VG Triple Trap and Optima IRMS at NIGL (NERC Isotope Geosciences Laboratory), were calculated to the V_{PDB} scale using a within-run laboratory standard calibrated against NBS-19 and NBS-22. Replicate analyses of sample material gave a precision of $\pm$ 0.1 (per mil) for $\delta^{13}C_{org}$ and 10% for C/N. Flux data (g cm^{-2} a^{-1}) were calculated from the product of dry mass accumulation rates (g cm^{-2} a^{-1}) (as dry bulk density (g cm^{-3}) x sedimentation rate (cm a^{-1})) and proxy concentration measurements (Street-Perrott et al., 2007).

Subsamples for diatom and stomatocyst analysis were taken at 4 cm and 8 cm intervals from the LP08 core following standard preparation techniques (Renberg, 1990; Sterken et al., 2012). At least 400 valves were counted per slide and species were identified to at least genus level using taxonomic studies from the region (Rumrich et al., 2000; Guerrero and Echenique, 2002). Where feasible, distinctions were made between different morphotypes of the small benthic fragilariod species (e.g., *Staurosirella* aff. *pinnata*; *Staurosira* aff. *venter*) since this can reflect different environmental conditions (Stevenson et al., 2008). No distinction was made between stomatocyst morphotypes.

Microscopic pollen, charcoal and cryptotephra shards were counted at 8 cm intervals in the LP08 core (Moore et al., 1991) with *Lycopodium* spores of known concentration added for quantification (Stockmarr, 1971). The total pollen sum from each subsample is at least 300 land pollen grains (Total Land Pollen, TLP) above 470 cm in the LP08 record (i.e., above the hiatus between Unit 1 and 5B). Local site indicators (e.g., obligate aquatic plants, moss spores and algae) were calculated as TLP + taxon. Charcoal was classified in five different size classes, <25 µm, 25–50 µm, 50–75 µm, 75–100 µm, and >100 µm, to distinguish between proximal and distal fires, assuming hydrodynamic fractionation at the regional scale. Diatom and pollen data were obtained from the more highly resolved Holocene Unit 5 and 6 sediments of the LP08 record. Both proxies were largely absent from the basal glaciolacustrine deposits in Unit 1 of both records.

Data were analysed and figures constructed in: R v. 4.1.0/Rstudio v. 1.4.1717, using the R packages Vegan, Rioja, Tidyverse (ggplot2), Ggally v. 2.1.2 (Juggins, 2012; Oksanen, 2014; Barret, 2021; Galili, 2021)(and other packages listed in the Figure captions and Supplementary Methods); Sigmaplot v. 14.0, C2 v.1.7.7 (Juggins, 2007); MATLAB v. R2021a and ESRI ArcGIS v. 10.4. The final layout of all figures was achieved in Adobe Illustrator CC v. 2021.

4. Results

4.1 Geomorphology and limnology

The NE shoreline of Lago Pato has a differential GPS (dGPS) ellipsoid corrected elevation of 32.7 ± 1 m a.s.l. (Table 1). Former lake shorelines immediately surrounding the lake are visible on satellite images between ~35-40 m a.s.l., and there are two further prominent shorelines at ~40–45 m a.s.l. and ~45-50 m a.s.l. that delineate the visible break from grassy wetlands to more densely vegetated bushland around the lake and the transition to more barren grassland cover on the surrounding moraine complexes. The LP08 site is the deepest point of the current lake, with a water level at ~32 m a.s.l. (Table 1), while the LP16 core site is located on a slightly elevated (~33–34 m a.s.l.) infilled littoral area of the basin, which is currently a seasonal (ephemeral) wetland, approximately 200 m SW of the LP08 core site (Figure 2B). Lago del Toro, immediately north, has a seasonally dependent water level of ~24 ± 5 m a.s.l.

Retaining shoreline ridges separating Lago Pato from Lago del Toro are ~4–10 metres above the present water level in Lago Pato, suggesting moderately higher lake levels in Lago del Toro could plausibly overspill into Lago Pato (Figure 2B). Our geomorphological data show that Lago Pato would have become an isolated and closed basin once the water level in Lago del Toro was <32–37 m a.s.l. Water column chemistry measured at the Lago Pato depocentre (LP08 coring site) in February 2007 had a pH of 8.87 ± 0.01 (n=3; mean ± 1σ), a specific conductance of 331 ± 2 µS cm^{-1}, and a temperature of 11.81 ± 0.04 °C and dissolved O_2 of 11.92 ± 0.05 mg l^{-1} (equivalent to 372.5 ± 1.7 µM). Visibility was limited to less than 1 m water depth, as a result of relatively high phytoplankton primary production.

4.2 Sedimentology, geochemistry, and chronology

The LP08 and LP16 records were divided into six lithofacies units shown in Figure 5. These are summarised and interpreted in Table 2, the Supplementary Results and Section 5.1. In summary, the littoral record (LP16) contains all six units, but glaciolacustrine Units 2–4 and the more organic subunit 5A were missing from the depocentre (LP08) record (Figure 5, S1). Units 5B–C and 6 (c. 10–5.8 cal ka BP) were preserved at a much higher resolution in the LP08 record, 0–470 cm (Figure 5A) compared to 0–50 cm in LP16 (Figure 5B). Figure 6A shows the transition from glaciolacustrine to full organic sedimentation at the start of the Holocene between Units 2–4 and 6 in LP16 when Lago Pato was isolated from Lago del Toro, and a short-lived return to glaciolacustrine sedimentation between c. 8.9–8.6 ka in Units 5B and 6 in LP08 (Figure 6A). Figure 6B–F, S3D and S6 illustrate the decadal to centennial-scale variability of erosional inputs into the deep glaciolacustrine basin of Unit 1 in the LP08 and LP16 records between c. 20–30 cal ka BP. In LP08, elevated C/N ratios in Units 5 and 6 reflect increased terrestrial organic matter input, with a notable increase in all productivity proxies from c. 5.6 cal ka BP onwards (Figure 5A). Principal components analysis (PCA) summarised in Figure 7 shows that the variance in the both LP08 and LP16 XRF-CS datasets is driven by erosional inputs (characterised most strongly by Ti, Rb, and K along the first PC axis in a positive direction) versus negative PC axis 1 values (inc. and coh. scatter, Br, which reflect organic productivity but not Zr as a matrix affect) (Figure S2, S3, S35).

A complex relationship between Ca, S, Mn, Sr, and to some degree Fe, exists, driven by a mixture of detrital and/or authigenic processes, but mainly redox changes, is represented by the second PC axis. This relationship varies between the two records and between units within each record. For example, in the LP08 record, an inverse correlation between K, Fe, Rb, Zn and to some degree Mn, versus incoherent and coherent scatter and Br, broadly aligns with PC1, while S is strongly correlated with Ca, Mn, and Sr, to a lesser degree, between PC1 and PC2 (Figure 7A, S2C). The PC3 axis reflects an inverse correlation between Mn and Ca, S (Figure 7B, S2E–H). In contrast, the LP16 record has increased variance along the PC2 axis, with Sr and Ca positively correlated with each other yet negatively correlated with all other elements (Figure S3D). In LP16, S is

strongly aligned along PC1, reflecting increased productivity and anoxia within Unit 5A (rather than carbonate), while the PC3 axis describes a positive correlation between Mn and S within Unit 1 (Figure S3) and is most likely related to deep water anoxia and the Mn and S peaks present in Figure 5B.

In both records, all calibrated Unit 1 ages from glaciolacustrine sediments were older than 20 cal ka BP, with basal ages of ~30–27 cal ka BP (Table 3). In LP08, a significant age gap exists between radiocarbon ages from the top of Unit 1 (471 cm: 21,230 ± 510 cal a BP modelled age ± mean 95% confidence interval) and the base of Unit 6 (470 cm: 10,160 ± 2,120 cal a BP), where a sharp (erosional) boundary exists. Units 2–5 appear to be missing and are present in LP16 only. Units 1 and 2 in the LP16 record are separated by a large age gap, defined by a large downshift in MS values at 110 cm and embedded *Myriophyllum* sp. macrofossils into Unit 2, but without a visually obvious sedimentary discontinuity between 115 to 111 cm (20,660 ± 250–20,440 ± 410 cal a BP), and ~110 cm (13,390 ± 440 cal a BP) (Table 3; Figure S1).

Late glacial transition ages in LP16 and Holocene ages from both cores (i.e., Units 2–6) were in broadly stratigraphic order, except for a minor age-reversal at 433 cm in LP08 (Table 2), where sediment reworking within the shallow basin is evident (Figure 5A, S1; Table 3). Ages from Units 2–6 had lower mean ± 2σ 95% confidence ranges (LP08: 300 ± 500 cal years; LP16: 320 ± 280 cal years) than the glaciolacustrine Unit 1 ages (LP08: 890 ± 560 cal years; LP16: 720 ± 440 cal years). Post-bomb calibration ages from an unconsolidated, macrophytic lake mud sample at 1.5–2 cm in the LP08 record, core-top terrestrial vegetation at 0–0.5 cm in the LP16 record and overlapping ages from paired lake-mud and plant macrofossil remains at ~40 cm depth imply that exchange between atmospheric and lacustrine carbon reservoirs have been in equilibrium during the late Holocene.

4.3 Diatom and pollen analysis

Diatom and pollen were largely absent from Unit 1 of the LP08 record, meaning only samples from 470 cm (10,160 ± 2120 cal a BP) upwards (Unit 5B) in the LP08 record had sufficient valves and concentrations of palynomorphs for reliable counting statistics. Although single valves of *Staurosirella* aff. *pinnata* (532.7 cm), *Achnanthes* spp. (530.3 cm) and *Fragilaria capucina* s.l., (486.3 cm) diatoms were found, the minerogenic sediments of Unit 1 and Unit 5 sediments up to 454 cm (>9280 ± 680 cal a BP) were characterized by a near absence of diatoms. Based on cluster analysis, the LP08 core was subdivided into six diatom zones (DZ1–6) between 454–0 cm depth (Figure 8, S7). Diatom concentrations remained low (<50x10^6 valves g^{-1} dry mass) in DZ1 (454–339 cm; 9280 ± 680–6180 ± 560 cal a BP). A diverse benthic diatom community, dominated by *Pseudostaurosira* spp., *Staurosira* aff. *venter*, *Staurosirella* aff. *lapponica*, *Staurosirella* aff. *pinnata*, and *Mastogloia* spp., was already established, supporting geochemical evidence that the first phase of isolation from Lago del Toro (Unit 5A) is missing from the LP08 record. At 416 cm (8150 ± 160 cal a BP), the initially turbulent, shallow-brackish, and nutrient-enriched lacustrine regime of DZ1a was replaced briefly by more stable, and possibly deeper water, indicated by the dominance (~80%) of planktonic species *Discostella stelligera* species 1 (sp.1). More turbulent and shallow-brackish conditions, with benthic *Pseudostaurosira* spp., *Staurosira* aff. *venter*, and *Mastogloia* spp. dominating, returned in DZ1b (Figure S7).

DZ2 and DZ3 (339–228 cm; 6180 ± 380–4520 ± 170 cal a BP) are characterised by the increasing dominance of large and heavily silicified (tycho-)planktonic *Aulacoseira* species and smaller planktonic *Discostella stelligera* s.l., which both indicate an increasingly stable, stratified lake with a shallow epilimnion. There is a dramatic increase in diatom concentration at c. 307 cm (*c.* 5320 ± 210 cal a BP) to >300x10^6 valves g^{-1}, followed shortly after by a significant increase in chrysophyte cyst concentration to >250 cysts g^{-1} (Figure S7). *Aulacoseira ambigua* became

increasingly abundant (>~ 50–60%) at this time implying a less well-stratified water column existed.

While *Aulacoseira ambigua* is absent further up-core, the dominance of planktonic species such as *Discostella stelligera* s.l. and *Aulacoseira granulata* s.l. implies more stable conditions (and perhaps deeper water) persisted in DZ4 and DZ3 (229–83 cm; 4530 ± 180–1960 ± 260 cal a BP). Benthic species such as *Staurosirella* aff. *pinnata* briefly became dominant at ~140 cm (2740 ± 260 cal a BP) within DZ4 when a dramatic reduction in the planktonic *Discostella stelligera* species to <20% abundance occurred. This brief excursion to more unstable conditions coincided with a shift to lower S/Ti ratios, indicative of slightly shallower, less anoxic conditions, a shift to less depleted $\delta^{13}C$ values (~ -30‰), and a short-lived erosional phase in the LP16 record at c. 2700 cal a BP. The return of *Discostella stelligera* s.l. to 60–80% abundance suggests a more stable deeper lake persisted until c. 2000 cal a BP, when an abrupt increase in benthic species (e.g., *Staurosirella* aff. *pinnata*) reoccurred. This and low chrysophyte cyst concentrations between 78–30 cm within DZ5 (DZ5: 83–30 cm; 1960 ± 260–1020 ± 310 cal a BP) are indicative of more turbulent conditions. These conditions persisted during the last c. 1,000 cal a BP (DZ6: 0–30 cm; 1020 ± 310– -60 ± 10), but with *Staurosira* aff. *venter* (>75%) dominating. In contrast, the most recent surface sample (0.25 cm) is dominated by planktonic *Cyclotella meneghiniana* (75%) species.

Above 470 cm (10,160 ± 2120 cal a BP), we identified 13 pollen taxa with a relative abundance of more than 2% and three significant local pollen assemblage zones (PZ 1–3 in Figure 8, S8). Pollen zones 1 and 2 (470–359 and 359–315 cm; 10,160 ± 2120–6890 ± 300 and 6890 ± 300–5400 ± 180 cal a BP), which map broadly onto Units 5B and 5C, are characterized by low total pollen (and diatom) concentrations, and relatively high values of Poaceae that reach a maximum (>60%) at 436 cm depth (8730 ± 270 cal a BP) and decline towards the top of the zone. Poaceae are commonly used as an aridity indicator species in Patagonia (Moreno et al., 2018; Moreno et al., 2021), and are more elevated in Unit 5B of LP08 where Fe/Mn and Mn/Ti are more variable and elevated Ca/Ti and Sr/Ti (carbonate) ratios and S peaks exist. Together, these proxies indicate a very restricted lake system existed in the early Holocene between c. 10,000–7500 cal a BP (Figure 5A, 8). Most notably, *Nothofagus dombeyi* type pollen starts to increase from ~420 cm (c. 8270 ± 240 cal a BP) onwards and there are low percentages of dwarf shrubs and herbs such as *Empetrum rubrum*, Asteraceae, *Acaena* and *Litorella* (Figure 8, S8). *Nothofagus dombeyi* type, which are inversely related to Poaceae, increase towards the top of this zone, while the abundance of Cyperaceae (and Polypodiaceae and *Pediastrum*, not shown in summary Figure 8, S8) remains high throughout.

In local pollen assemblage zone 3 (PZ 3 in Figure 8, S8; 315–0 cm; 5400 ± 180 – -60 ± 10 cal a BP), *Nothofagus dombeyi* type continues to dominate (60–80%), with the total pollen concentration higher than in PZ 1 and 2, indicating a generally more productive (wetter) environment. The hemiparasite *Misodendrum* requires *Nothofagus* as a host for germination and establishment; hence, *Misodendrum* and *Nothofagus dombeyi* are well-correlated (Figure 8). Poaceae abundances were lower (<30%) and oscillated at (sub)millennial timescales, while other dwarf shrubs and herbs almost disappeared from the record until the last 500 years. The decline in Cyperaceae at the start of pollen zone 1 continued until present. The relative abundance of *Pediastrum* is lower than PZ 1, but oscillates, reaching peak values between ~200–100 cm (3920–2220 cal a BP). Small amounts of introduced European taxa (e.g., *Plantago* and *Rumex acetosella*, not show in Figure 8) were present near the top of the core.

5. Discussion

5.1 Lake geochemistry and ontogeny

In the following section, we interpret the main geochemical changes in the LP08 and LP16 records (see Table 2 for summary).

Unit 1 (30–20 ka): The elevated sediment density, magnetic susceptibility and minerogenic input (e.g., K, Ti, Fe, Rb, Sr) and the near complete absence of pollen in Unit 1 are consistent with a high input of fine glacial clay eroded from an enlarged, glaciated and sparsely vegetated catchment (Figure 9). Fine glacial sediment in suspension would have created 'turbid' conditions even within a relatively deep lake, preventing the establishment of photoautotrophic diatom communities (Karst-Riddoch et al., 2009). Prolonged phases of perennial lake-ice cover and increased turbidity are consistent with the low primary production and production proxy values (e.g., $\%C_{org}$, C/N, inc./coh.), the absence of diatoms (Hodgson et al., 2009), and stratification within perennially ice-covered and deep glaciolacustrine lakes (Wennrich et al., 2014).

Fine grey glaciolacustrine sediments are enriched in Fe and Mn but have broadly stable Fe/Mn ratios throughout Unit 1, suggesting an erosional source of glaciogenic sediment into Lago del Toro that did not change substantially until the start of the Holocene. As Fe^{2+} is less stable in anoxic lake sediments and precipitates before Mn^{2+}, elevated Fe/Mn ratios have been used as a proxy for increased stability (and anoxia) in deep, well-ventilated lakes (Kylander et al., 2011). Decadal-scale elevation of Mn and Fe coincides with phases of reduced erosional input (shown by <Ti in Figure 6B) and is associated with manganese carbonate formation, rhodochrosite ($MnCO_3$), commonly found in areas of shale bedrock and anoxic conditions (Melles et al., 2012), but has also been used as indicator of increased oxidation where wind-driven mixing of the water column exists in deep lakes (Moreno et al., 2007; Kylander et al., 2011). In shallow(er) lakes, >Mn can reflect complete overturning (and oxygenation) of stratification, reducing Mn solubility and causing manganese oxides and hydroxides to co-precipitate with iron oxy-hydroxides (Wennrich et al., 2014; Davies et al., 2015).

Comparatively minor increases in Fe/Mn and decreased Mn/Ti in Unit 1 (relative to Unit 5) most likely reflect short-lived bottom water anoxia interspersed with oxidation events linked to minor increases in Mn^{2+} precipitation, and/or secondary mobility between Fe and Mn phases within laminations (Figure 5, 6, 8A). High MS and exceptionally elevated Mn/Ti peaks in LP16 Unit 1 (and 2) reflect increased mixing and oxidation of anoxic Mn^{2+} during lake overturning (Figure 6B–D, 8). A minor component of biogenic magnetite formed under anoxic conditions (Kirschvink and Chang, 1984) could exist, but this is more likely in Unit 5 where strong anti-correlation between these ratios also exists during an early to mid-Holocene arid phase c. 11.8–7.5 ka, extending until c. 5.6 ka (Figure 6A, 8B).

Periodic orangey brown Ti- and Ca- rich bands within Unit 1 imply decadal-centennial scale phases of increased erosion, or erosion from a different local source, perhaps with a degree of secondary diagenetic mobility between Fe and Mn between 29.8–20.5 ka (i.e., the period covered by Unit 1 in Lago Pato) (Figure 6B–F, 9A, S3B, S6). Cycles in Fe/Mn and Mn/Ti profiles within the basal deposits of Unit 1 and across the whole of Unit in LP08 have several significant (>2-sigma) periodicities (Figure 6D, S6E, F). Decadal scale variability is apparent within Unit 1 of both records, notwithstanding its average age model 95% CI of >700 years. The mean prominent peak-peak interval for Ln(Fe/Mn) and Ln(Mn/Ti) in LP08 Unit 1 is 35 ± 19 and 37 ± 22 years (Figure S6C, D) and 34 ± 16 and 37 ± 16 years for LP16 Unit 1 (Figure S6N, O). Decadal scale variations are also apparent in the wavelet analysis shown in Figure 6D–F. Since the data shown have been interpolated to evenly-spaced 10-year intervals, a combination of multiple 8–16-year SAM cycles (Yuan and Yonekura, 2011) could plausibly be responsible for the low frequency ~20–40-year periodicities observed in Unit 1 (Figure 6D–F, S6E–K). At the centennial scale, the 197 year periodicity in Fe/Mn and the 191 year periodicity in Mn/Ti for the LP08 Unit 1 basal deposits (Figure 6D), and the 197/233 year periodicity in Fe/Mn and the 248 year periodicity in

Mn/Ti for the whole of LP08 Unit 1 (Figure S6E,F) are broadly similar to the ~200–250-year solar cycle that is thought to modulate SWW airflow detected in high resolution pollen records from Patagonia and the Falkland Islands (Turney et al., 2016; Moreno et al., 2018). Longer (centennial–millennial) periodicities in Unit 1 deposits of both LP08 and LP16 might reflect 'grand solar cycles' driven by changes in the Sun's magnetic field (Ineson et al., 2015). Due to the short timespans of the sequences examined, we failed to find convincing evidence for the ~2.4–2.5 kyr Hallstatt solar activity cycle (Viaggi, 2021), but it seems likely that millennial- to centennial-scale variations in solar activity (shown in Figure 10A), the SWW, and the SAM (Figure 10B, F), coupled with changes in internal glacier dynamics, drove fluctuations in glacier accumulation, meltwater input and seasonal lake-ice cover between the l-LGM and g-LGM. The latter likely accounts for variations in deep water (in)stability, redox conditions, and lake stratification processes between 29.8–20.5 ka.

Several lines of evidence support Units 2–5A being missing from the LP08 record: 1) the lack of pollen from a cold-steppe scrubland environment and the existence of an already established open landscape with a *Nothofagus* forest (comprising ~30% of TLP) around Lago Pato; 2) the existence of a benthic diatom community in organic sediments of Unit 5B that were deposited unconformably on top of Unit 1 glacial sediments; 3) the presence of shallow water sub-aquatic angiosperm *Myriophyllum* sp., an early coloniser in organic deposits <10 ka (Unit 5 in LP08); 4) the absence of two substantial Volcan Reclus tephras dated to 9320 ± 15 ^{14}C yr BP (10,570–10,300 cal a BP) in the basal glaciolacustrine unit in a record from nearby Lago Eberhard (Moreno et al., 2012) and other lake records in the Última Esperanza region (Sagredo et al., 2011), and the R1 tephra dated to 12,627 ± 48 ^{14}C a BP (15,190–14,610 cal a BP) (Sagredo et al., 2011). The latter is >20 cm thick in the Cerro Benitez area ~31 km S of Lago Pato (McCulloch et al., 2021) and presence in lacustrine deposits indicates that ice had thinned to at least ~ 215 m a.s.l. by 17.5 ka (Sagredo et al., 2011).

Units 2–4 (13.4–11.8 ka): The presence of *Myriophyllum* sp. fragments embedded in the glaciogenic deposits of Unit 2 and a ~10 cm thick *Myriophyllum* sp. layer is evidence of a substantial increase in lake productivity following a dramatic drop in lake level c. 13.4–13.0 ka. Increasing Ca and Sr (but not S) towards the top of Unit 3 and into Unit 4 relates to precipitation of authigenic calcite was likely triggered by increased alkalinity linked to anaerobic degradation of organic matter (Torres et al., 2020) (Figure S3A). The lack of Mn enrichment in units 3 and 4 (characterised by low Mn/Ca, Figure 5B, S3) suggests Mn was not available for fixation during authigenic (early diagenetic) carbonate precipitation (Figure 9B).

Unit 5 (11.6–5.6 ka): Exceptionally elevated and concomitant Ca/Ti and S/Ti and low Mn/Ca in Unit 5 represent localised authigenic carbonate and/or sulphate precipitation, possibly gypsum ($CaSO_4 \cdot 2H_2O$; asterisks in Figure 5) or anhydrite. The presence of large S peaks indicates relatively S-rich lake bottom waters (SO_4 or H_2S, depending on local redox conditions) despite freshwater conditions. Gypsum precipitation implies subaerial exposure (drying), or potentially subaqueous anaerobic oxidation of solid sulphides by Fe^{3+} or Mn^{4+} (Aller and Rude, 1988; Pirlet et al., 2010). This seems plausible since Unit 5 exhibits phases of authigenic enrichment in Mn (exceptionally high Mn/Ti; Figure 5, 8).

Unit 5 of LP16 has two phases of exceptionally elevated Fe/Mn ratios: an initial 'Anoxic Crisis' following isolation from Lago del Toro at the start of the Holocene and a secondary phase between c. 9–7.5 ka. High Fe/Mn and high Fe/Ti in Unit 5 (Figure 5, 8, S6), above the 'background' glaciogenic detrital signal, implies a preference for authigenic enrichment of Fe compared to Mn. Assuming redox conditions analogous to Brownie Lake (Wittkop et al., 2020), fixation of Fe^{2+} was most likely triggered by oxidation of anoxic (Fe-rich) lake waters across the chemocline (Figure 9C). Alternatively, the very high Fe content of Unit 5A might be attributed to

a very shallow, possibly even terrestrial, environment at the littoral LP16 site as peat can becomes highly enriched in Fe^{3+} during more oxic (drier) conditions (Schittek et al., 2015). Fe enrichment also occurs in anaerobic (very shallow) organic lake and peat deposits when organic material breaks down under stable conditions (Damman, 1978). Mn is then reduced from tetravalent MnO_2 to its divalent Mn^{2+} state and removed from organic matter, elevating Mn values and ratios. The near absence of Mn, and low Mn/Ti when Fe/Mn is elevated in Unit 5B/C, implies that the LP08 depocentre remained submerged throughout the Holocene.

More stable conditions associated with reduced SWW between c. 11.6–5.5 ka were interrupted by short-lived phases of instability, most notably at c. 10.5–10.0 ka in LP16, which coincides with the timing of the erosional hiatus in the LP08 record at c. 10.1–10.0 ka. The concomitant reversal in the Fe/Mn profiles of LP08 and LP16 following the 'Early Holocene Anoxic Crisis' (c. 11.7–10.1 ka) in Unit 5A of LP16 (Figure 7, 10G) suggests local redox processes and water depth, rather than regional (climatic) processes, were the main control on the distribution of these metals during the Holocene.

A simple 'oxide model' attributing Mn enrichment to onset of more oxygenated bottom water conditions (Force and Cannon, 1988; Calvert and Pedersen, 1996) is not considered plausible since bottom waters were *least* ventilated at LP08, the lake depocentre, compared to LP16. A more credible explanation invokes Mn-carbonate (most likely rhodochrosite, $MnCO_3$) precipitation immediately beneath the chemocline at LP08, with trapping of Fe-oxides above the chemocline at LP16 (Figure 9B), consistent with redox systematics in analogous lakes (e.g., Brownie Lake; Wittkop et al., 2020). Fixation of Mn in carbonate is supported by increased Mn/Ca in Unit 5B-C at LP08. A fluctuating and complex redox relationship between Fe and Mn in LP08 is evident in orange 'pelletised' deposits with exceptionally elevated MS, Mn, and Mn/Ti ratios in Unit 5B (Figure 6A). These most likely due to co-precipitation of Mn under anoxic conditions (or possibly the formation of rhodochrosite or kutnahorite minerals, particularly where Fe enrichment occurs). The presence of benthic diatoms in Unit 5B implies bottom water conditions at LP08 during the early to mid-Holocene were only intermittently (rather than persistently) anoxic (Figure 7, 8, 9), while the disappearance of benthic diatoms at the base of Unit 5C and through most of Unit 6, until c. 1.5 ka, suggests the development of more permanent anoxia in a deeper and more stable lake between *c.* 7.3–5.6 ka onwards.

Unit 6 (5.6– -0.06 ka): Increasing Ti content and Mn/Ca implies Unit 6 at LP16 was deposited under progressively shallow water (above the chemocline), culminating in a sharp decline in the Fe/Mn profile at LP16 profile c. 500–200 years ago, which mirrors the increasingly anoxic >Fe/Mn trend in the submerged LP08 site (Figure 10G), and implies a shift to terrestrial subaerial conditions at the littoral margins of Lago Pato. At LP08, the continued accumulation of macrophytic organic matter, suggests lacustrine conditions were more favourable for colonisation. Progressively increasing Fe/Mn, a sharp decrease in Mn/Ca and Mn/Ti (Figure 5A, 8), the lack of authigenic enrichment in redox-sensitive metals (e.g., V) and return of benthic diatoms (Figure 8, S7) all suggest bottom waters became progressively more ventilated at the depocentre in the late Holocene, consistent with the well oxygenated modern lake conditions (371 µM O_2 (11.9 mg/l).

To summarise, we have identified six key phases in the history of Lago Pato. In the following sections we relate these five phases to glacier retreat and readvance and lake level change in the Torres del Paine and Última Esperanza region since ~39 ka and, more widely, to hemispheric-global driving mechanisms of paleoclimatic change, in particular, the changing strength and position of the SWW relative to 51°S.

5.2 Local to Regional implications
Local LGM – global LGM and deglaciation (<39 – >14 ka)

The LP08 and LP16 records provide evidence of glaciolacustrine deposition into Lago Pato until c. 11.7 ka (Figure 10G; Table 2 for summary). High volumes of minerogenic erosional inputs and low productivity fluxes throughout lithofacies Unit 1 and in Units 2–4 reflect the proximity of an ice tongue from an expanded Southern Patagonian Icefield following retreat from the l-LGM (c. 37–30 ka) and after the g-LGM (c. 26–19 ka) (Hughes and Gibbard, 2015). A large ice-dammed proglacial lake, palaeo-Lago Tehuelche, covered Lago del Toro and Lago Sarmiento < c. 38 ka and >c. 17.6–16.8 ka, between local and global LGM advances (c. 32–27 ka), and as glaciers withdrew after the g-LGM (García et al., 2012; García et al., 2014; Davies et al., 2020) (locations B_1, B_2 in Figure 2A, 9). Unit 1 in LP08 and LP16 is a preserved fragment of this former palaeolake sedimentary record, with a 'floating chronology', reflecting deposition in a deep palaeo-proglacial lake that existed at Lago Pato between 30–20 ka, prior to g-LGM, and ACR readvances over Lago del Toro and Lago Pato between 14.6–12.9 ka. (Figure 8, 9, 10).

A glaciolacustrine environment existed at Lago Pato between c. 28–20 ka after glaciers had receded from their most advanced (MIS 3) positions along the Río Tres Pasos valley to the south-east, where a terminal moraine has been dated to c. 39-37 ka (location A_2 in Figure 2A). From c. 30 ka onwards, as the Antarctic Ice Sheet and sea-ice grew during the g-LGM, the core belt of SWW became weaker at 51°S as it shifted equatorward to ~40–45°S, north of Lago Pato and its current alignment with the Antarctic Circumpolar Current off the coast of Chile at ~50-52°S (Toggweiler and Russell, 2008; Van Daele et al., 2016; Quade and Kaplan, 2017) (Figure 10B). Reduced precipitation supply in the Última Esperanza region led to glacier retreat and large palaeolakes formed as the main SPI outlet glacier covering Lago del Toro thinned and withdrew eastwards and from its maximum extent along the Río Prat and Río Tres Paso valleys to the south and south-east (Figure 9A) (Sagredo et al., 2011; Solari et al., 2012; García et al., 2014). Palaeolakes in the Puerto Consuelo and Última Esperanza fjords merged, forming a much larger palaeo-Lago Tehuelche–Puerto Consuelo, up to 280 m a.s.l. deep along the Río Prat valley (García et al., 2014; Davies et al., 2020) (Location B_1, Figure 2A, 9A). Ice-dammed deposits and terraces in the Río Prat, Río Tres Paso and Puerto Consuelo valleys between 125–155 m a.s.l. have been dated to c. 18–17 ka (García et al., 2014), suggesting that an ice dam up to 150–200 m a.s.l. existed along the Puerto Consuelo-Última Esperanza fjord at the gLGM.

The absence of deglacial age sediments <20 ka at both coring sites in Lago Pato implies that it was either overridden by readvancing LGM and ACR glaciers or sediments were removed when palaeo-Lago Tehuelche emptied across the Lago Pato spillway sometime between c. 20–13.4 ka, in line with García et al. (2014) (Figure 2B, 9B, 9C). The latter interpretation is more probable as geomorphological evidence and glacial debris associated with glacier advances over Lago Pato are absent. After glaciers had retreated in the early Holocene the removal of Units 2–4 from LP08, and the exceptionally sharp erosional boundary between the glaciogenic sediments of Unit 1 and organic deposits of Unit 6, was created by meltwater emptying across the Lago Pato depocentre at c. 10 ka (Figure 8, 9).

Successive palaeolake lowering after the gLGM occurred sometime before c. 17 ka during Stage I of the Cordillera Paine glaciation scheme (García et al., 2014; García et al., 2018), and after glacial advance stages C and D in the Strait of Magellan that ended between c. 21.7–20.4 ka and c. 17 ka (McCulloch et al., 2005). The oldest minimum radiocarbon ages for ice retreat and the formation of ice-dammed lake deposits in the Lago Sofia-Puerto Consuelo valley area are c. 18–17 cal ka BP (Sagredo et al., 2011; McCulloch et al., 2021) (Figure 2) .

García et al. (2014) associated a small moraine-arc to a former ice-lobe that extended east and southwards into the Río Prat Valley (B_1 in Figure 2A) and the now abandoned outwash sandur plains formed along to the south and east of Lago del Toro with ice-dammed palaeo-Lago Tehuelche. This finally emptied, sometime after c. 16.8 ka, but before the start of the ACR at c.

14.6 ka when a northward latitudinal shift in the SWW drove glacier readvance across this part of Patagonia (Figure 2A) (Pesce and Moreno, 2014; Moreno et al., 2018; Moreno, 2020; Fletcher et al., 2021). The absence of sediment dated between c. 20–13.5 ka from both Lago Pato records is consistent with basal ages of c. 14.6 ka from the Lago Cipreses record (~11 km west WNW of Lago Pato at 51°17'16.43"S, 72°50'12.18"W; Figure 10F) that constrain the initiation of local ice-free and the end ice-marginal glaciolacustrine conditions at ~110 m a.s.l. along the southern shore of Lago del Toro (i.e., ~ 85 m above Lago del Toro at 25 m a.s.l.) (Moreno et al., 2018).

Organic sedimentation in the higher altitude closed basin Lago Cipreses record at 110 m a.s.l. suggests ice covering Lago del Toro had receded by more than 12 km from the end of the lake (and also inward by more than 50%) by 14.6 ka (Moreno et al., 2018). A similar transition is recorded in lake records from the Puerto Consuelo area at ~15.4 ka (80 m a.s.l.) (Pantano Dumestre) implying a stepwise regression of Lago Puerto Consuelo began before the start of the ACR at c. 14.6 ka (Moreno et al., 2012).

Late glacial–Holocene (13.4 – 11.7 ka)
The lower altitude Lago Pato records provide evidence of two further stepwise lowering events during the Late glacial: 1) At c. 13.4–13.0 ka, towards the end of the ACR, when lake levels dropped from >100 m a.s.l. to between 40–50 m a.s.l. (Figure 5B, 8, 9B). This is consistent with the c. 12.8 ka cessation of glaciolacustrine deposition at Lago Eberhard ~ 70 m a.sl. (cf. Moreno et al., 2012); 2) At c. 11.7 ka, when water levels dropped below 40 m a.s.l., Lago Pato became isolated from Lago del Toro (Figure 9C).

The most dramatic reduction in lake level at c. 13.4–13.0 ka is represented in LP16 by the presence of the shallow water *Myriophyllum* sp. layer Unit 3 within glaciogenic sediments and exceptionally elevated Ca (and S, Sr) due to increased deposition of shallow water carbonates (Units 3 and 4) (Figure 8). This post ACR drainage event occurred after Meltwater Pulse 1A at c.14 ka during a phase of rapidly-rising global sea level and oceanic warming (Figure 10L) and before an unprecedented 700-year warming of the Southern Ocean at c. 12 ka (Bereiter et al., 2018). During the Late glacial, an enlarged proglacial lake encompassed Lago Pato, Lago del Toro, Lago Porteño and all the smaller basins and sandur along the Río Serrano (García et al., 2014). This palaeolake was topographically dammed at ~50 m a.sl. in the Río Prat valley and at a similar elevation by the glacier that still occupied the Puerto Consuelo fjord (Figure 9B). A lower-altitude ice tongue in Río Serrano Valley (B_3 in Figure 2A, 9A), at least 25 m a.s.l. along the western outflow of Lago del Toro would have also been necessary to create an ice-dammed palaeolake in contact with the SPI (Marden et al., 1993; García et al., 2014).

Lago Pato is bounded topographically at ~40–50 m a.s.l. to the south and east, and by a broad, undated (probably ACR) moraine complex that runs parallel with the southern present-day shoreline of the Bahía del Bote section of Lago del Toro to the northeast and west (Figure 2A). Since Lago Pato was topographically constrained to the north and east (> ~45 m a.s.l.), and the wetlands and the retaining sill to the south are at a much lower elevation (32–33 m a.s.l.; Table 1), the c. 13.4–13.0 ka lake drainage event, near the end of the ACR, would have passed through the Lago Porteño-Río Prat valley, rather than directly over Lago Pato (Figure 9B). A lower altitude for palaeolake implied by the presence of shallow subaquatic macrofossils in the Lago Pato LP16 record is supported by a lack of glaciolacustrine deposits above 100 m a.s.l. younger than 16.8 cal ka BP in the Última Esperanza–Puerto Consuelo fjords.

As the core SWW belt migrated equatorward past 51°S during the ACR, outlet glaciers were maintained in relatively advanced positions in TdP (Bertrand et al., 2017; Quade and Kaplan, 2017; Fletcher et al., 2021) (Figure 10B, D). Southward movement of the SWW back past 51 °S after the ACR and continued poleward until c. 12 ka (Quade and Kaplan, 2017; McCulloch et al,

2020) and likely drove down precipitation levels, leading to the removal of high-altitude ice dams that had maintained palaeolake Tehuelche-Puerto Consuelo at >100 m a.s.l. (Figure 10B, D)

A second reduction in lake level to between ~30–40 m a.s.l. at c. 11.7 cal ka BP, isolated Lago Pato from Lago del Toro, cutting off the glaciolacustrine sediment supply from erosion of the TdP massif. An enlarged Lago del Toro had remained topographically dammed up to ~50 m a.s.l. along the Río Prat valley until low-level ice dams <~40–50 m a.s.l. in the Puerto-Consuelo fjord area most likely failed. This phase of lake regression is consistent with the minimum age for organic sedimentation of 10.3 ka from the Pantano Antonio Varas lake record at ~ 25 m a.s.l. and a ~30 m terrace constraining ice-dammed lake regression on the southern peninsula of Puerto Consuelo Fjord (Sagredo et al., 2011) (Figure 2A).

Early-mid Holocene (11.7–5.6 ka)

The isolation of Lago Pato from Lago del Toro at the start of Unit 5A, c. 11.7 cal ka BP, is marked by a shift to a shallower lake system dominated by organic-rich lake muds and littoral vegetation. The time period covered by the zonally-coherent Early Holocene Westerlies Minimum (EHWM: 11.5–7.5 ka; Moreno et al., 2021) is characterised, initially, by greater stability in the littoral environment of Lago Pato between c. 11.7–10.1 ka, with exceptionally elevated Fe/Mn during the 'Anoxic Crisis' phase (Figure 10G) and possible peat formation over the LP16 site. Two early Holocene erosional contacts, between Units 1 and 6 at c. 10 ka, and at the boundary between Unit 5B-2 and 5B-3 at c. 8.9–8.6 ka in LP08 (Figure 5A, 6A), coincide with increased oxidation in LP16 sediments (downward arrows 3 and 4 in Figure 10F), suggesting a highly variable lake level, fluctuating at or near the height of the retaining sill during the early Holocene, with occasional flushing through the depocentre (Figure 5, 6, 8, 9B, 10F).

At the start of the Holocene, glaciers along the SPI retreated rapidly to close to their present-day, land-locked, limits, as evidenced by moraines preserved in Río Serrano area ~30 km west of Lago Pato with cosmogenic surface exposure isotope ages of 11.3–10.7 cal ka BP (location C in Figure 2B) (Marden and Clapperton, 1995; Solari et al., 2012; Aniya, 2013). Similar to nearby lake studies (e.g., Lago Cipreses; Figure 10F) (Moreno et al., 2018), we found no evidence of further glacier readvances over Lago Pato during the Holocene.

New data from Lago Pato are consistent with the timing of: 1) forest expansion in and around Última Esperanza from c. 11.9 cal ka BP onwards (Moreno et al., 2012; Moreno and Videla, 2016; Moreno et al., 2018; McCulloch et al., 2021; Moreno et al., 2021); 2) regional fjord deglaciation (Bertrand et al., 2017); and 3) regional pollen and lacustrine records from 52–55°S (Zolitschka et al., 2018; McCulloch et al., 2020; Moreno et al., 2021). Increasingly arid conditions (linked to falling lake levels) have been found in a number of early Holocene terrestrial records from Southern Patagonia (Moreno et al., 2012; Zolitschka et al., 2013; Moreno et al., 2018; Zolitschka et al., 2018; Reynhout et al., 2019; McCulloch et al., 2020; Moreno et al., 2021) and in the wider sub-Antarctic region, e.g., Macquarie Island at 54 °S in the Southern Ocean (Saunders et al., 2018) (Figure 10C, F, G, I, J).

During the transition into the Holocene, the core SWW belt remained strong and possibly more poleward-shifted, but weaker at its northern margins (Toggweiler et al., 2006; Toggweiler and Russell, 2008; Quade and Kaplan, 2017; Moreno et al., 2021). This drove down moisture leading to deglaciation in Patagonia (Quade and Kaplan, 2017; Moreno et al., 2018; Kaplan et al., 2020). A phase of exceptionally positive planetary radiative imbalance following the ACR between c. 12–9 ka (Baggenstos et al., 2019) (Figure 10A) and the shift to an increasing trend in summer insolation at 51 °S from c. 10 ka (Figure 10A) likely resulted in the contraction of the polar vortex, leading to a poleward shift in the SWW and the prolonged period of positive SAM-like conditions between c. 11.5–10 ka (Figure 10F).

Continued lake regression at this time reflects the poleward limit of the SWW (~55° S) and/or a zonally-coherent EHWM (11.5–7.5 ka) between 50–54° S (Saunders et al., 2018; Moreno et al., 2021) and a prolonged phase of increasingly positive SAM-like conditions (Figure 10B–G) (Quade and Kaplan, 2017). Elevated conductivity in a lake record from Macquarie Island at the start of the Holocene, followed by a reduction in conductivity to a minimum between c. 11–10 ka, implies a hemispheric poleward shift of the core SWW to south of ~54°S could have occurred during the EHWM (Saunders et al., 2018). The removal of sediments at c. 10 ka from the Lago Pato depocentre (LP08) occurred as the SWW were starting to move equatorward once more from their most poleward position of the early Holocene (Figure 10B).

A return to glaciolacustrine sedimentation in Lago Pato at c. 8.9 ka implies an isolation breach, most likely due to a precipitation-driven refilling/flushing event during a regionally wetter phase (Figure 6A) (Moreno et al., 2018; Zolitschka et al., 2018), or a short-lived enlargement of Lago del Toro between c. 8.9–8.6 ka, possibly linked to glacier readvance, re-damming and subsequent dam failure at the Río Serrano/Puerto Consuelo Fjord outlet (Figure 2, location B3). Both scenarios are consistent with the core SWW returning northward from ~55–60 °S to ~51 °S between c. 10–8 ka, bringing increased precipitation (Figure 10B) (Quade and Kaplan, 2017; Moreno et al., 2021). The increasing conductivity trend between c. 10–6 cal ka BP in a lake record from Macquarie Island (Saunders et al., 2018) suggests a potential hemispheric equatorward shift in the SWW back over ~54°S at this time.

All proxy evidence from Lago Pato points to more arid conditions with decadal to centennial-scale fluctuations in water column stability (redox) until c. 7.5 ka (Figure 8, 10G). Lower lake levels in Lago Pato (below the overspill ridge limit of ~30–35 m a.s.l. into Lago del Toro) between 9.7–7 cal ka BP are broadly consistent with: 1) an extended period of 'extreme dryness' in the Laguna Potrok Aike, a closed basin ~175 km southeast of Lago Pato, which is not influenced by SPI glacial activity in an area where the local correlation between present day annual wind speed and precipitation is negative (Zolitschka et al., 2013) (Figure 10C); 2) pollen records from Isla Navarino, further south (54–55°S) (McCulloch et al., 2020); 3) an early Holocene dry period in Laguna Azul, south-eastern Patagonia (52°S), between c. 10.1–8.3 cal ka BP (Zolitschka et al., 2018). While higher lake levels at Potrok Aike during the EHWM time period have been associated with phases of incursion of precipitation bearing Easterlies (Ariztegui et al., 2010), consistently drier conditions across all these records likely reflects the increasing trend in summer insolation over 50–55°S and the poleward migration of the core SWW belt south of 52°S and/or phases of reduced Easterlies incursion into eastern Patagonia (Fletcher and Moreno, 2012; Saunders et al., 2018; Moreno et al., 2021) (Figure 10A, B). These interpretations have not yet been reconciled with generally wetter and windier conditions inferred from some records from the west coast of Patagonia (Lamy et al., 2010) and further north in Chile (Van Daele et al., 2016) during the early Holocene.

The Lago Pato pollen record is overwhelmingly dominated by forest taxa (mainly *Nothofagus* pollen) (Figure 8, 10G, S8). Unlike nearby Lago Cipreses (Moreno et al., 2018), and similarly high-resolution pollen records further east (Mayr et al., 2007) and south (McCulloch et al., 2020), we found limited evidence of high frequency or rapid (climate-driven) variability in our pollen data during the Holocene. The more highly resolved lacustrine redox proxies (e.g., Fe/Mn (anoxia) and Mn/Ti (oxidation)) display sub-millennial/centennial scale variability. This is less well-defined than the centennial–millennial scale periodicities in the Fe/Mn in the pre-Holocene LP08 record, but broadly similar to the variability found in pollen data produced by Moreno et al. (2018) from Lago Cipreses (~11 km WNW of Lago Pato), and some other SE Patagonian lakes (Zolitschka et al., 2018).

Several palaeorecords suggest that a highly variable precipitation regime existed in Patagonia well into the mid Holocene (Mayr et al., 2007; Lamy et al., 2010; Moreno et al., 2018; Zolitschka et al., 2018). These include, for example, the occurrence of a grass steppe biome in a pollen record from Cerro Frías (Mancini, 2002; Mancini, 2009), increased fire activity in the Río Rubens region (Huber et al., 2004). These two records were later re-evaluated, with periods of relatively high, but extremely variable, precipitation with extended periods of summer drought between c. 11–5.5 ka (Markgraf and Huber, 2010).Variable redox conditions in Lago Pato during the early–mid Holocene reflect changes in lake stability and are consistent with the variable precipitation and SAM regimes identified between c. 10.8–6.8 ka in the nearby Vega Ñandú (Villa-Martínez and Moreno, 2017) and Lago Cipreses lake records (Moreno et al., 2018) (Figure 10C, F, G). A period of increased early–mid Holocene variability is also consistent with an 'erosive' interval found between c. 10.6–6.6 ka in the Lago Eberhard sediment core (Moreno et al., 2012), attributed to a lake low-stand, warmer/drier conditions and a reduction in SWW influence over the TdP region, and Patagonia more generally, between c. 10.4–7.5 ka either as the SWW migrated poleward again (after 8 ka) or when SWW zonal intensity declined (Figure 10B) (Quade and Kaplan, 2017; Moreno et al., 2021).

From c. 7.4 ka onwards, Lago Pato maintained an organic-rich depositional environment. Even in wetter periods, the maximum water level remained below the retaining sill at ~33 m a.s.l., forming an enlarged and more stable (and increasingly more anoxic) palaeo-Lago Pato that most likely encompassed both the LP08 and LP16 core sites. This is evident in Figure 8 and Figure 10G from increasing similarity between the PC1 and Fe/Mn profiles for both records from c. 7.4 ka onwards and supported by the greater prevalence of pollen and diatom species associated with wetter conditions and forest density from c. 7.7 ka (Figure 8, 9, 10G, H).

Wetter conditions after c. 7.4 ka are consistent with the expansion of a humid-temperate closed forests dominated by mainly *Nothofagus* from c. 7.5 ka in lake records in the Última Esperanza Province and further south after c. 7 ka (McCulloch et al., 2020; Moreno et al., 2021). Progression to wetter and more stable conditions during the mid to late Holocene is also mirrored at localities similar distances from the eastern flank of the Andes, and in palaeo records across a W-E transect at ~51°S (Figure 3, 10). A co-eval readvance of the Cordillera Darwin Icefield occurred between c. 7.3–5.7 ka (Bertrand et al., 2017), with refilling of Laguna Potrok Aike accelerating after c. 7 ka (Zolitschka et al., 2013) (Figure 10C). The shift to a more closed forest, indicative of generally wetter conditions, also began at c. 7.7 ka in records from the eastern shore of Brazo Sur (Wille and Schäbitz, 2008; Markgraf and Huber, 2010), but was delayed until c. 5.1 ka in the Vega Ñandú area (Villa-Martínez and Moreno, 2017). The establishment of a dense *Nothofagus* forest in the Vega Ñandú area also coincided with an abrupt decrease in fire frequency and a shift from minerotrophic to ombrotrophic bog taxa at Río Rubens after c. 5.5 ka (Huber et al., 2004). Increasingly wetter conditions in these records reflects generally wetter conditions in southern Patagonia and the more stable and equatorward expansion of the core SWW belt, and more negative SAM-like conditions after c. 5.7 ka (Figure 10B, F) (Markgraf and Huber, 2010; Moreno et al., 2021). The transition from open to closed forests at Lago Pato coincided with rising temperatures between 60–90 °S from 7.5 ka (Marcott et al., 2013) and the global 'Holocene thermal maximum' centred on 6.5–6.0 ka cal BP, which was 0.7 °C warmer than the pre-industrial 19th Century (Kaufman et al., 2020) (Figure 10H, M).

Mid–late Holocene (5.7–1.9 ka)

Greater hydrological stability with a more stable lake water column and increasing stratification in Lago Pato between c. 5.6–1.9 ka is shown by consistent C/N ratio values (Figure 5A), the increasing dominance of planktonic diatoms, which reflect progressively deeper water levels and a reduced littoral zone, and an increasingly anoxic trend (Figure 5A, 8, 10G, S7). For example, between c. 6.5–3.0 ka, heavily silicified planktonic diatom species (e.g., *Aulacoseira ambigua*,

Aulacoseira granulata s.l., and *Cyclostephanos* cf. *patagonicus*) were relatively abundant, indicating more stable water levels (Figure S7), yet turbulent mixing likely prevented these relatively heavy taxa from sinking out of the photic zone (Kilham and Kilham, 1975; Rioual et al., 2007). A concomitant gradual increase in *Discostella stelligera* s.l., a smaller euplanktonic diatom with an efficient nutrient uptake strategy, implies periodic stratification of the water column (Figure S7A) (Rühland et al., 2003; Tolotti et al., 2007; Rühland et al., 2008; Winder et al., 2009). In TdP, Patagonian steppe pollen (mainly Poaceae), indicating drier conditions, were replaced by increasingly dominant *Nothofagus* pollen suggesting a more closed and dense forest.

The mid–late Holocene stabilisation of Lago Pato is consistent with cooler and wetter conditions at ~51°S that have been attributed to a relatively minor reduction and/or continued equatorward shift in the SWW north of ~51°S into the lower latitudes (Figure 10B) (Lamy et al., 2010; McCulloch et al., 2020; Moreno et al., 2021). The intensification of the SWW over southern Patagonia at this time is thought to have been modulated by an increasing trend in summer insolation, and initiated at c. 7.5 ka (Figure 10A) by a steepening of the pole-to-equator temperature gradient (Lamy et al., 2010). This led to a cooling trend in the South Pacific Ocean (Lamy et al., 2010; Whitlock et al., 2017; Moreno et al., 2018), as well as increased sea-ice and reduced ocean productivity around Antarctica (Mayr et al., 2007; Peck et al., 2015).

Decadal (ENSO-like) to millennial– centennial scale (SAM-like) variability in the SWW during the mid–late Holocene has been detected in several small and sensitive lake systems in Patagonia (Moreno et al., 2018; Reynhout et al., 2019). West of the Andes, wetter conditions are also thought to reflect the increased regional-seasonal variability in SWW intensity (Moreno et al., 2009a; Kilian and Lamy, 2012; Villa-Martínez and Moreno, 2017). Meanwhile, in the east, the equatorward shift in the SWW from c. 5.5 ka led to increasing lake levels as precipitation-laden frontal systems from the Atlantic became more dominant (Lamy et al., 2010; Zolitschka et al., 2013). The increased influence of the ENSO in the last four thousand years is thought to have contributed to minor readvances of glaciers across Southern Patagonia (Moreno et al., 2010; Fletcher and Moreno, 2012; Villa-Martínez and Moreno, 2017; Kaplan et al., 2020; McCulloch et al., 2020).

Between c. 5.6–1.9 ka, proxy data from Lago Pato indicate that net annual precipitation-evaporation was broadly balanced (Figure 8, S7). Since 2010 CE, wind strength in Patagonia has increased during summer, when the core SWW are more focussed and poleward shifted. As austral summer winds have strengthened over the last decade, the correlation between wind strength and precipitation over Lago Pato during the austral summer has become increasingly negative (r=0, 1979–2010 CE; r=-0.2 to -0.4, 2007–2017 CE) (Figure 4F, G). In the austral winter, the SWW are more diffuse, with the core SWW belt driven slightly northwards as the jet stream moves into subtropical latitudes of about 30°S. This equatorward shift broadens and weakens, the core wind-belt, particularly north of ~50°S (Garreaud et al., 2013; Bertrand et al., 2014; Fiers et al., 2019). As a result, winter precipitation is more intense further north of ~35°S (Figure 4D). At Lago Pato, the SWW have become marginally weaker and the correlation between wind and rainfall in the winter consistently positive (r=+0.4–0.6 in 2017) (Figure 4H). A similar scenario in autumn or winter during the mid–late Holocene would have resulted in higher amounts of precipitation and a well-mixed water column in Lago Pato. Less intense SWW and reduced precipitation during the austral summer would have led to smaller phytoplankton taxa blooms as more stable, but nutrient depleted, conditions. For small lake systems such as Lago Pato located in transitional locations between the Andes and eastern Patagonia, even a comparatively small net reduction in SWW and/or warmer temperatures in summer would result in a relatively more stable water column. Additionally, increased precipitation in winter (Figure 4D) would have maintained glaciers and a denser, more closed *Nothofagus* forest ecosystem. This

kind of seasonal response has been inferred from pollen records elsewhere in Torres del Paine (Moreno et al., 2018) and from Isla Navarino at ~54–55°S (McCulloch et al., 2020).

Late Holocene–recent (1.9–0 ka)
Shallower and more turbulent conditions in Lago Pato between c. 1.9–0.5 ka are marked by an increase in benthic diatoms in Diatom Zone 6, Mn/Ti ratios, indicating increased mixing and oxidation, and higher C/N values (Figure 5A, 8, S7), reflecting a greater input of terrestrial material or a higher contribution of macrophytes to lake primary production (Duff and Smol, 1995). In sub-Arctic lakes, planktonic diatoms are rare or absent if the water level is less than five metres deep (Karst-Riddoch et al., 2009). In Lago Pato, previously dominant planktonic taxa were replaced by c. 1.9 ka by assemblages composed of small chain-forming benthic/tychoplanktonic *Fragilariod* species. The latter are common during pioneering turbid and lower nutrient conditions (Bigler et al., 2003) and also occur in lakes with increased alkalinity (Wilson et al., 2012), longer winter lake ice-cover (Smol, 1983), and increased availability of aerophilic habitats (Van Dam et al., 1994).

While further studies are needed to understand the ecological preferences of *Fragilariod* species (Bennion et al., 2010), their abrupt development after c. 1.9 ka coincides with a decline in the total amount of stomatocysts that are mainly formed by euplanktonic chrysophytes (Figure S7A, B). Increased wind-induced detachment from the littoral zone likely brought more benthic diatoms into suspension. Enlargement of the wetland area surrounding Lago Pato and its shallow benthic zone explains the continuous deposition of organic matter at the shallower/littoral LP16 core site throughout the Holocene. The presence of an extensive shallow wetland basin (LP16) with a deeper water zone (LP08) also explains the co-existence of planktonic and benthic diatom communities in the LP08 sediments. This culminated in the (re)deposition of a Sr-rich outwash sand layer (S) in LP08 at c. 1.4 ka and a dramatic increase in oxidation at the LP16 site in the last ~200 years, indicative of recent subaerial exposure of the littoral zone (Figure 5A, 8, 10G).

Declining biological productivity and total land pollen between c. 1.4 ka and the present-day (Figure 8) were driven by predominantly negative SAM-like conditions at ~51°S between c. 2–0.5 ka in South America (Figure 10F) (Abram et al., 2014). The SAM was modulated by increasing SWW at ~51°S and an enhanced ENSO in this interval and, in particular, during the Medieval Climate Anomaly (MCA: c. 1–0.7 ka, 1250–950 CE) (Mann et al., 2009; Abram et al., 2014). Changes linked to a warmer MCA in South America have been inferred from some (Moreno and Videla, 2016), but not all, records in the Última Esperanza region (Moreno et al., 2010; Villa-Martínez and Moreno, 2017; Moreno et al., 2018). The influence of the MCA is not well-represented in the Lago Pato data (Figure 8, 10G).

In the last ~500 years, *Nothofagus* forest cover remained relatively constant, while carbon and nitrogen content rose. The declining benthic diatom community suggests reduced levels of turbulence and catchment instability, consistent with: 1) an equatorward shifted SWW during a 'post-MCA' phase of negative SAM-like conditions; 2) extreme cold 'events' in most Southern Hemisphere palaeorecords (Neukom et al., 2014); 3) minor glacier advances across the Patagonian Icefield and the Northern Antarctic Peninsula (Reynhout et al., 2019; Kaplan et al., 2020; Simms et al., 2021); 4) the Northern Hemisphere 'Little Ice Age' (0.55–0.25 ka, 1400–1700 CE) (Mann et al., 2009; Kaufman et al., 2020; Perren et al., 2020). European weed species, such as *Plantago* and *Rumex acetosella*, became established in the Lago Pato catchment (Figure 8). These species are commonly found in other pollen records from Patagonia and relate to increased human activity, principally pastoral farming, which has converted much of the natural *Nothofagus* forest to a grass-steppe biome. Natural lake infilling processes combined with increased human activity in the TdP area could have led to increased macrophyte development and elevated lake sediment carbon and nitrogen levels observed in Lago Pato (>30% C and ~ 4% N, approximately

double the mid-late Holocene mean N value). Recent increases in *Cyclotella meneghiniana* are also likely to be related to human-induced changes in the lake catchment (Van Dam et al., 1994), rather than (natural) lake ontogeny or warmer conditions.

6. Conclusions

We analysed two sediment core records from Lago Pato, a small lake basin located in a climatically transitional location east of the Andes and topographically separated from Lago del Toro in the Torres del Paine National Park, Southern Chile, to provide insights into changing glacier configurations, lake level change and climate-driven regional vegetation changes in the Última Esperanza region over the last ~30,000 years. Focussing on the last glacial-interglacial transition and Holocene parts of the records that are well-preserved, we undertook detailed geochemical, pollen and diatom analysis to examine the relationship between changes in lake level, water column stability, bottom water redox conditions and precipitation-evaporation balance at the site.

We identified the following five key evolutionary phases in the history of Lago Pato, which we link to deglaciation and palaeoenvironmental change in the Torres del Paine and Última Esperanza region and wider regional to global climate changes during the Late glacial and Holocene:

1) *<39 ka – 13.4 ka:* A deep proglacial lake encompassing Lago del Toro and Lago Pato, with evidence of decadal-centennial scale redox variations, developed between the l-LGM ~38–30 cal ka BP and the g-LGM ~26–19 cal ka BP. This palaeolake was dammed by glacier ice >100 m thick along the Puerto Consuelo– Última Esperanza fjord to the south. Sediments dated between 20–13.4 ka were removed from the Lago Pato littoral record following a large lake drainage event near the end of the ACR.
2) *<13.4–11.7 ka:* Lake levels over Lago Pato were lowered from >~100 m a.s.l. to ~40–50 m by two drainage events. The enlarged palaeolake became shallower as regional glaciers retreated and low altitude ice-dams in the Última-Esperanza fjord failed at c. 13.4 ka and c. 11.7 cal ka BP as the SWW shifted poleward south of 51 °S after the ACR. Lago Pato was isolated from Lago del Toro at 11.7 ka by the second lake lowering event.
3) *11.7–5.6 ka:* A stable, anoxic early Holocene shallow littoral–terrestrial environment was replaced by an increasingly productive and littoral–shallow, and periodically oxidising, lacustrine environment with a variable lake level. The presence of open *Nothofagus* forests and benthic diatom assemblages are consistent with regional aridity associated with more positive SAM-like conditions and poleward SWW south of ~51°S. Two refilling and flushing (erosional) events create a hiatus at c. 10 ka and a brief return to glaciolacustrine sedimentation at c. 8.6–8.4 ka in the LP08 depocentre record due to the enlargement of Lago del Toro as the SWW moved equatorward towards ~51°S between c. 10–8 ka. Lago Pato returned to an isolated and productive regime between 8.4–5.6 ka as the SWW shifted poleward, south of ~51°S again.
4) *5.6–1.9 ka:* Increasing stability and anoxia between c. 4.5–4 cal ka BP in Lago Pato is associated with an equatorward shift in the SWW back past ~51°S as negative SAM-like conditions prevailed during the mid–late Holocene.
5) *1.9–0 ka:* A shallower subaqueous lacustrine phase in the depocentre with increased turbulence reflecting generally increased SWW in the second half of the late Holocene. In the last 500 years, reduced levels of turbulence and catchment instability reflect reduced or equatorward shifted SWW during the 'Little Ice Age' advance in TdP. Vegetational changes in recent centuries and decades most likely relate to increased pastoral farming and human activity in the Torres del Paine area.

Conflict of Interest

The authors declare that the research was conducted in the absence of any commercial or financial relationships that could be construed as a potential conflict of interest.

Author Contributions

SR, RM, JE, SD, WvN and EV conceived the research questions, obtained funding, wrote the manuscript, constructed figures and tables, undertook XRF-CS, pollen, diatom analysis, analysed the data and wrote code; MS and EvdeV identified diatoms and collected diatom samples; SR, MS, KH, JvW, CD, EV, DH, and WV undertook fieldwork. SD, JE, and AW undertook laboratory and data analysis and helped construct figures; all authors edited and commented on the final manuscript.

Data availability

The original contributions presented in the study are included in the article/Supplementary Material , further inquiries can be directed to the corresponding author. Data has been deposited in the NERC EDS UK Polar Data Centre (PDC) as follows: Bathymetric and lake chemistry data: https://doi.org/10.5285/D55D7619-3E07-41B0-929E-C9DA0A4B61AF; LP08 lake sediment record data: https://doi.org/10.5285/C75EA98B-080E-455E-A54F-A9E8CF07AA73; LP16 lake sediment record data: https://doi.org/10.5285/F85EE4EB-8918-4AA4-8E51-6C46F4C812CB; Time series data: https://doi.org/10.5285/6BD95602-F2E3-4968-8622-C4AEB71C214C. Code and data can be found at: https://github.com/stever60/Lago_Pato.

Funding and Acknowledgments

This project was funded by the Natural Environment Research Council (NERC) through the British Antarctic Survey (BAS) and an UGent BOF bilateral collaboration project. RMcC was supported by Programa Regional R17A10002 and R20F0002 (PATSER) ANID. We gratefully acknowledge the University of Magallanes (UMAG) and the University of Santiago (Carolina Diaz) for assistance with fieldwork; the NERC/SUERC AMS Radiocarbon Facility for providing initial range-finder radiocarbon dates; the NERC Isotope Geosciences Laboratory (NIGL, now National Environmental Isotope Facility, NEIF, at the British Geological Survey) and Melanie Lang for stable carbon isotope analysis; Aberystwyth University (David Kelly), Durham University (Neil Tunstall and Christopher Longley) and Edinburgh University (Chris Hayward) for use of their core scanning and microprobe facilities and technical support. We also thank John Turner and Tony Phillips for assistance with ERA-INTERIM analysis, Chris Darvill, Neil Glasser, Mike Kaplan, and Patricio Moreno for access to their published datasets, and Mike Kaplan for permission to use and adapt the SAM-index diagram used in Figure 10F. We are grateful to two anonymous reviewers for their constructive and insightful comments which helped improve the manuscript.

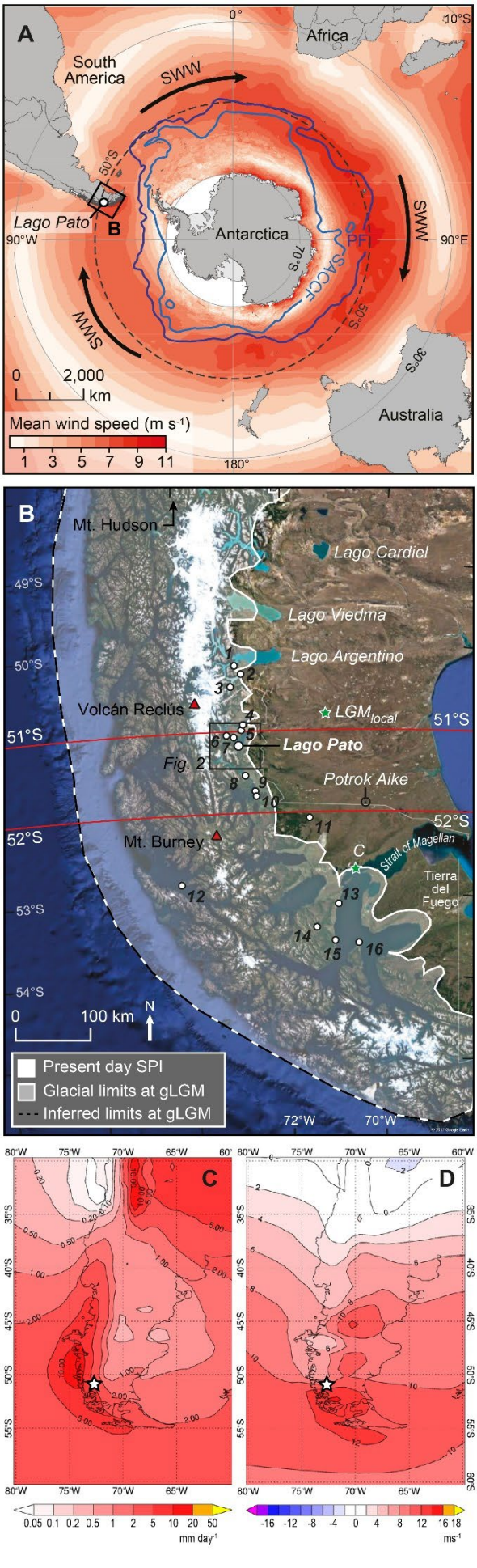
A
South America
Africa
SWW
Lago Pato
B
Antarctica
PF
SACCF
Australia
0 2,000 km
Mean wind speed (m s-1)
1 3 5 7 9 11
B
Mt. Hudson
Lago Cardiel
Lago Viedma
Lago Argentino
Volcán Reclús
LGMlocal
Lago Pato
Fig. 2
Potrok Aike
Mt. Burney
Strait of Magellan
Tierra del Fuego
0 100 km N
Present day SPI
Glacial limits at gLGM
Inferred limits at gLGM
C
D
mm day-1
ms-1

Figure 1. (A) Location of Lago Pato in relation to the Southern Hemisphere Westerly Winds (SWW), the Southern Antarctic Circumpolar Current Front (SACCF), and the Polar Front (PF); **(B)** Location of Lago Pato, the extent of the global Last Glacial Maximum (g-LGM) South Patagonian icefield, c. 20–25 ka (McCulloch et al., 2005; Davies et al., 2020). The green star marked LGM_{local} is the local Last Glacial Maximum (l-LGM) extent c. 48–34 ka (Glasser et al., 2008; García et al., 2014); the green star marked C is the ice-extent of Stage C advance in the Strait of Magellan (McCulloch et al., 2005). Red triangles are major volcanoes active during the Holocene. Key locations mentioned in the text and the sites of previous studies are: 1=Peninsula Avellaneda; 2=Cerro Frías peat sequence; 3=Brazo Sur; 4=Vega Nandú; 5=Pantano Margarita; 6=Lago Guanaco; 7=Meteorological Station; 8=Eberhard Site; 9=Pantano Dumestre; 10=Puerto Natales; 11=Río Rubens; 12=Lake Tamar; 13=Punta Arenas; 14=Puerto del Hambre; 15=Estancia Esmeralda II. 16, Isla Dawson. The background LANDSAT imagery in (B) courtesy of the U.S. Geological Survey (https://www.usgs.gov/centers/eros) generated in Google Earth, © Google.com. **(C, D)** ERA-INTERIM reanalysis (Dee et al., 2011) for (C) mean annual surface precipitation (mm per day; 1/6/1979–1/6/2017) and (D) zonal wind velocity (U on P at 850-hPa over the Andes; ms^{-1}; 1/6/1979–1/6/2017) over southern South America (30–60 °S), covering the period up to when cores were taken from LP16. Lago Pato is located at the white star.

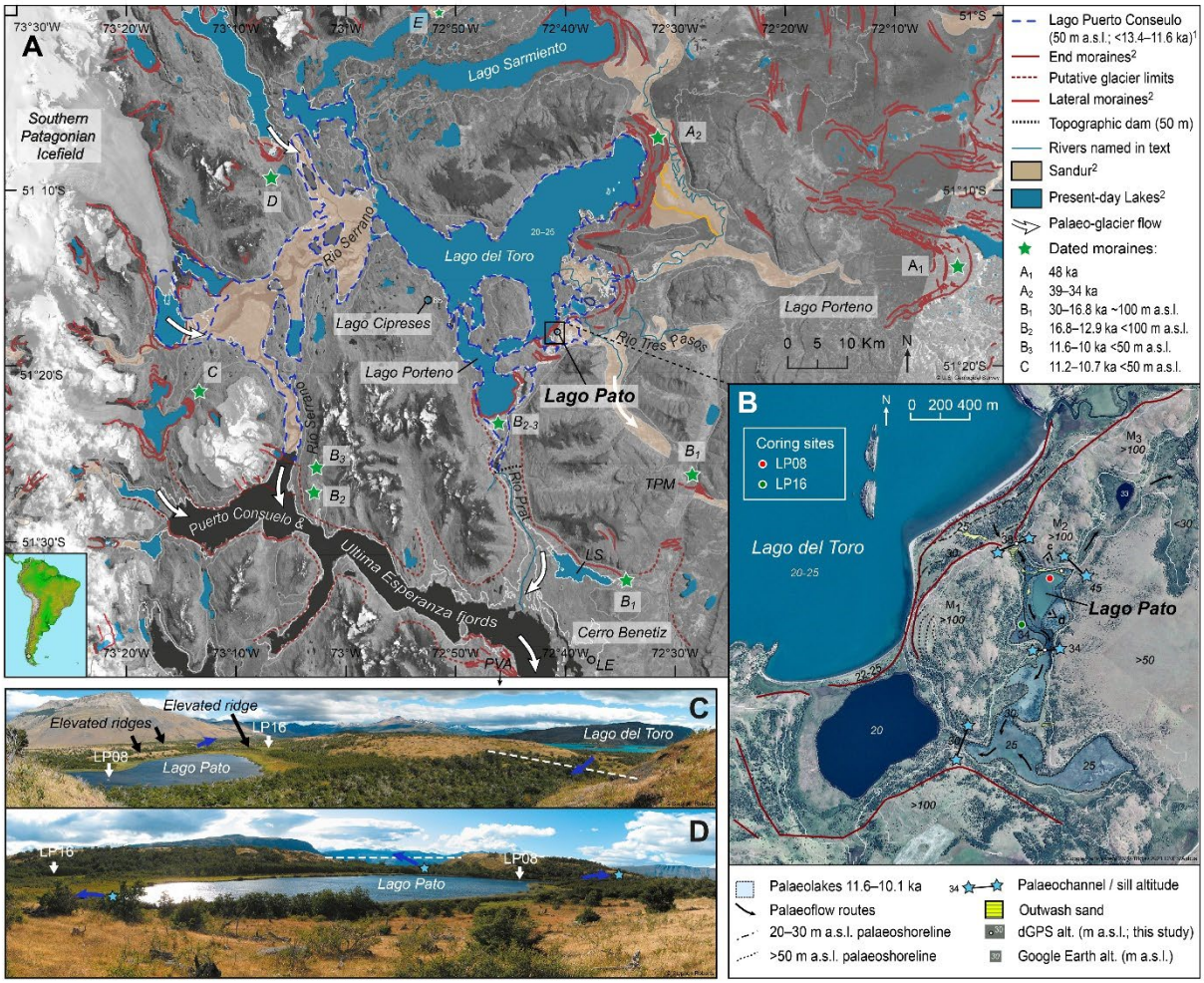

Figure 2. (A) Location map highlighting key geomorphological features in the Torres Del Paine region (based on data in Glasser et al. (2008)). The 50 m a.s.l. contour is shown as a dotted blue line. Green stars summarise the extent and age of former regional glaciations. 1=García et al. (2014; 2=Glasser et al. (2008). The background LANDSAT-8 satellite image was superimposed on the GEOTOP30 DEM in ARC-Map (www.esri.com), both courtesy of the U.S. Geological Survey (https://www.usgs.gov/centers/eros). **(B)** Summary geomorphological sketch showing the

~40 m a.s.l. palaeoshoreline of Lago Pato, and flow pathways and retaining ridges that would isolate Lago Pato from Lago del Toro (blue stars) as follows: 1) in the wetland to the south, separated by a sill elevation of 33.4 ± 0.1 m a.s.l.; 2) at 38.0 ± 0.1 m a.s.l., through a gap filled with outwash sand deposits between the prominent moraine complex that runs parallel with the southern shore of Lago del Toro to the northwest; 3) outflow breaching the northeastern sill at ~40-45 m a.s.l., requiring more substantial lake level rise of >10 m. Once the lake level in Lago del Toro dropped below ~40–38 m a.s.l. the only drainage route from Lago Pato was to the south, over the southern sill at ~32 m a.s.l. into the adjacent lake and Lago del Toro (~20–25 m a.s.l.). Areas to the south and southeast of Lago Pato, mapped as sandurs by Glasser et al. (2008), were visited during coring and interpreted as temporary wetlands that dry up during summer. LS is Lago Sofia, LE is Lago Eberhard, TPM is Tres Pasos Moraine, PVA is Pantano Antonio Varas. The background image was generated in Google Earth, © Google, imagery © CNES/Airbus, Maxar Technologies. **(C)** View from the northern side of Lago Pato showing the coring sites LP08 and LP16 and meltwater channels cut through the elevated moraine ridges on the NW and SE shores. **(D)** View looking towards the NE ridge and meltwater channel from the southern side of Lago Pato.

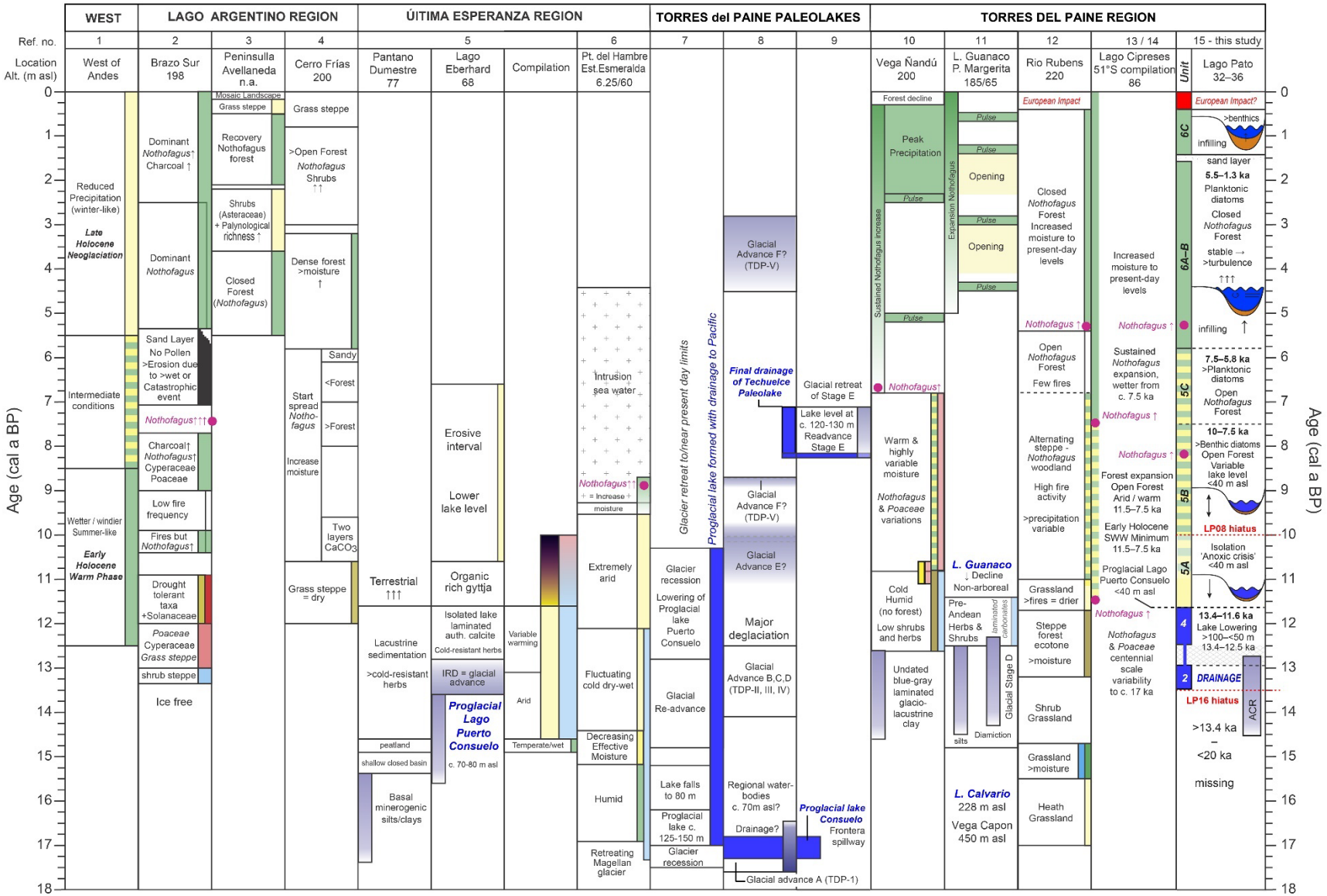
WEST
LAGO ARGENTINO REGION
ÚITIMA ESPERANZA REGION
TORRES del PAINE PALEOLAKES
TORRES DEL PAINE REGION
Ref. no.
Location
Alt. (m asl)
1
West of Andes
2
Brazo Sur 198
3
Peninsulla Avellaneda n.a.
4
Cerro Frías 200
5
Pantano Dumestre 77
Lago Eberhard 68
Compilation
6
Pt. del Hambre Est.Esmeralda 6.25/60
7
8
9
10
Vega Ñandú 200
11
L. Guanaco P. Margerita 185/65
12
Rio Rubens 220
13 / 14
Lago Cipreses 51°S compilation 86
15 - this study
Unit
Lago Pato 32–36
Age (cal a BP)
Reduced Precipitation (winter-like)
Late Holocene Neoglaciation
Intermediate conditions
Wetter / windier Summer-like
Early Holocene Warm Phase
Dominant Nothofagus↑ Charcoal ↑
Dominant Nothofagus
Sand Layer No Pollen >Erosion due to >wet or Catastrophic event
Nothofagus↑↑↑
Charcoal↑ Nothofagus↑ Cyperaceae Poaceae
Low fire frequency
Fires but Nothofagus↑
Drought tolerant taxa +Solanaceae
Poaceae Cyperaceae Grass steppe
shrub steppe
Ice free
Mosaic Landscape
Grass steppe
Recovery Nothofagus forest
Shrubs (Asteraceae) + Palynological richness ↑
Closed Forest (Nothofagus)
Grass steppe
>Open Forest Nothofagus Shrubs ↑↑
Dense forest >moisture ↑
Sandy
Start spread Notho-fagus
Increase moisture
<Forest
>Forest
Two layers CaCO3
Grass steppe = dry
Terrestrial ↑↑↑
Lacustrine sedimentation
>cold-resistant herbs
peatland
shallow closed basin
Basal minerogenic silts/clays
Erosive interval
Lower lake level
Organic rich gyttja
Isolated lake laminated auth. calcite
Cold-resistant herbs
IRD = glacial advance
Proglacial Lago Puerto Consuelo
c. 70-80 m asl
Variable warming
Arid
Temperate/wet
Intrusion sea water
Nothofagus↑↑
= Increase = moisture
Extremely arid
Fluctuating cold dry-wet
Decreasing Effective Moisture
Humid
Retreating Magellan glacier
Glacier retreat to/near present day limits
Proglacial lake formed with drainage to Pacific
Glacier recession
Lowering of Proglacial lake Puerto Consuelo
Glacier Re-advance
Lake falls to 80 m
Proglacial lake c. 125-150 m
Glacier recession
Glacial Advance F? (TDP-V)
Final drainage of Techuelce Paleolake
Glacial Advance F? (TDP-V)
Glacial Advance E?
Major deglaciation
Glacial Advance B,C,D (TDP-II, III, IV)
Regional water-bodies c. 70m asl?
Drainage?
Proglacial lake Consuelo
Frontera spillway
Glacial advance A (TDP-1)
Glacial retreat of Stage E
Lake level at c. 120-130 m Readvance Stage E
Forest decline
Peak Precipitation
Pulse
Sustained Nothofagus increase
Nothofagus↑
Warm & highly variable moisture
Nothofagus & Poaceae variations
Cold Humid (no forest)
Low shrubs and herbs
Undated blue-gray laminated glacio-lacustrine clay
Expansion Nothofagus
Opening
L. Guanaco ↓ Decline Non-arboreal
Pre-Andean Herbs & Shrubs
laminated carbonates
Glacial Stage D
silts
Diamiction
L. Calvario 228 m asl
Vega Capon 450 m asl
European Impact
Closed Nothofagus Forest Increased moisture to present-day levels
Nothofagus ↑
Open Nothofagus Forest Few fires
Alternating steppe - Nothofagus woodland
High fire activity
>precipitation variable
Grassland >fires = drier
Steppe forest ecotone
>moisture
Shrub Grassland
Grassland >moisture
Heath Grassland
Increased moisture to present-day levels
Nothofagus ↑
Sustained Nothofagus expansion, wetter from c. 7.5 ka
Nothofagus ↑
Nothofagus ↑
Forest expansion Open Forest Arid / warm 11.5–7.5 ka
Early Holocene SWW Minimum 11.5–7.5 ka
Proglacial Lago Puerto Consuelo <40 m asl
Nothofagus ↑
Nothofagus & Poaceae centennial scale variability to c. 17 ka
European Impact?
6C
>benthics
infilling
sand layer
5.5–1.3 ka
Planktonic diatoms
Closed Nothofagus Forest
stable → >turbulence
↑↑↑
6A–B
infilling
7.5–5.8 ka
>Planktonic diatoms
Open Nothofagus Forest
5C
10–7.5 ka
>Benthic diatoms
Open Forest
Variable lake level <40 m asl
5B
LP08 hiatus
Isolation 'Anoxic crisis' <40 m asl
5A
13.4–11.6 ka
Lake Lowering >100–<50 m 13.4–12.5 ka
4
2
DRAINAGE
LP16 hiatus
>13.4 ka – <20 ka
missing
ACR

Figure 3. Summary palaeoenvironmental interpretations for key studies from in Chilean Patagonia mentioned in the text (1–14). Summary findings from Lago Pato from this study are included in 15 for comparison. References: 1=(Lamy et al., 2010); 2=(Wille and Schäbitz, 2008); 3=(Echeverria et al., 2014); 4=(Mancini, 2009); 5=(Moreno et al., 2012); 6=(McCulloch and Davies, 2001); 7=(Sagredo et al., 2011); 8=(García et al., 2014); 9=(Solari et al., 2012); 10=(Villa-Martínez and Moreno, 2017); 11=(Moreno et al., 2009a; Moreno et al., 2009b); 12=(Markgraf and Huber, 2010); 13/14=(Moreno et al., 2018; Moreno et al., 2021); 15=This study.

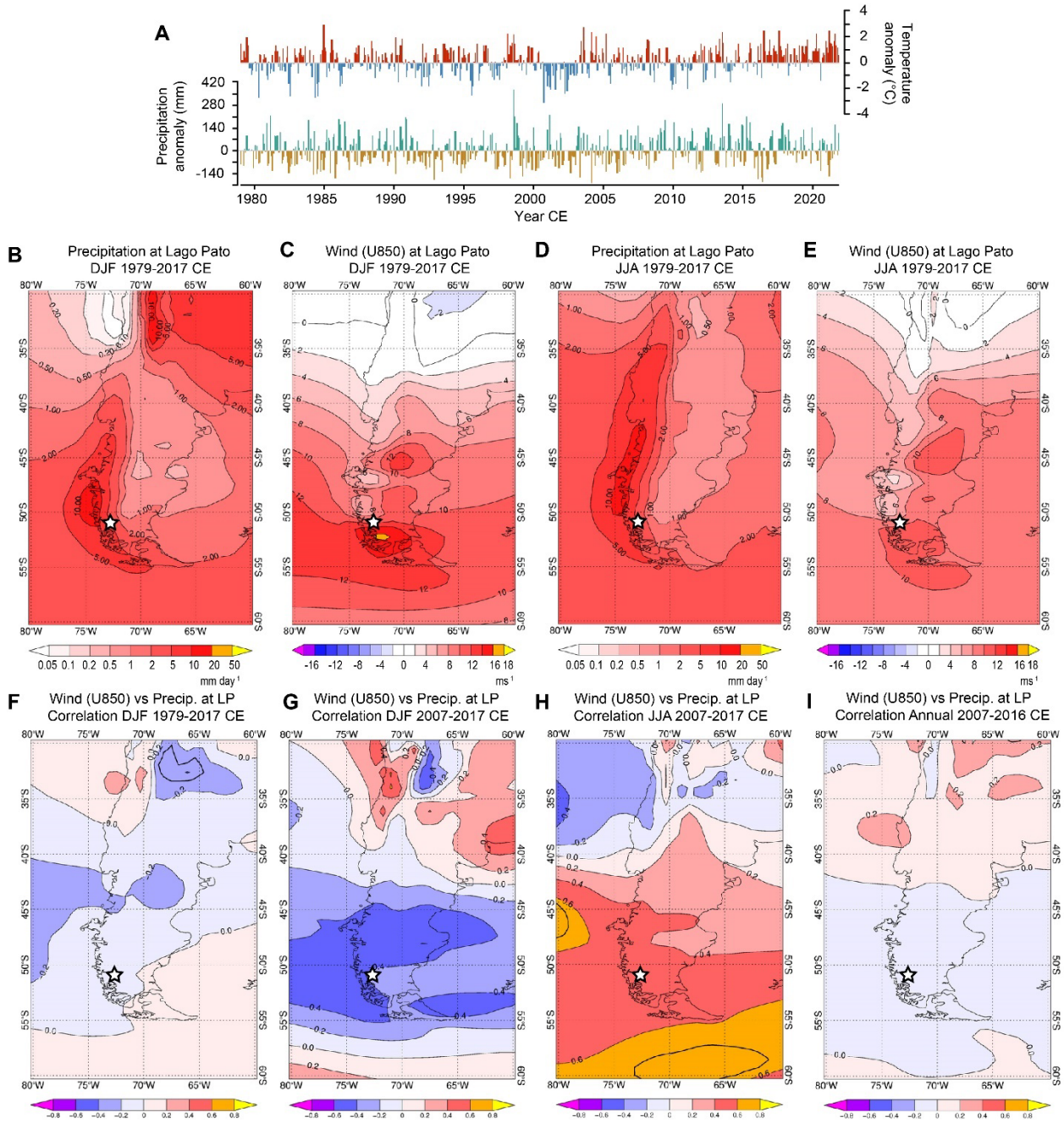

Figure 4. (A) Temperature and precipitation anomaly data from Parque Nacional Torres del Paine meteorological station between 1979–2021. Data generated from and copyright of https://www.meteoblue.com are used here with permission. **(B–E)** ERA-INTERIM reanalysis (Dee et al., 2011) for mean Austral summer (December-January-February; DJF) and winter (June-July-August; JJA) mean surface precipitation (mm per day; 1/12/1979–1/3/2017) and zonal wind speed (U on P at 850-hPa over the Andes in ms^{-1}; 1/12/1979–1/3/2016) over southern South

America (30–60 °S) between 1979-2017 CE. The white star is the location of Lago Pato. **(F)** ERA-INTERIM reanalysis data showing neutral to marginally negative correlation coefficients between mean zonal wind velocity over southern South America and mean surface precipitation at Lago Pato for the austral summer (DJF) from 1/12 to 1/3 between 1979–2017 CE compared to **(G)** increasingly negative time mean correlation coefficients over Lago Pato for the austral summer (DJF) from 1/12 to 1/3 between 2007–2017 CE and **(H)** a positive time mean correlation coefficients at Lago Pato for the austral winter (JJA) from 1/6 to 1/9 between 2007–2017 CE. **(I)** Time mean correlation coefficient map of annual mean wind velocity over southern South America (30–60 °S) and annual mean precipitation at Lago Pato (white circle) between 1/12/1979–1/12/2016 CE. ERA-INTERIM maps and data were generated using the BAS internal portal http://basweb.nerc-bas.ac.uk/icd/toil/clivarm_data/index.html with the final layout made in Adobe Illustrator.

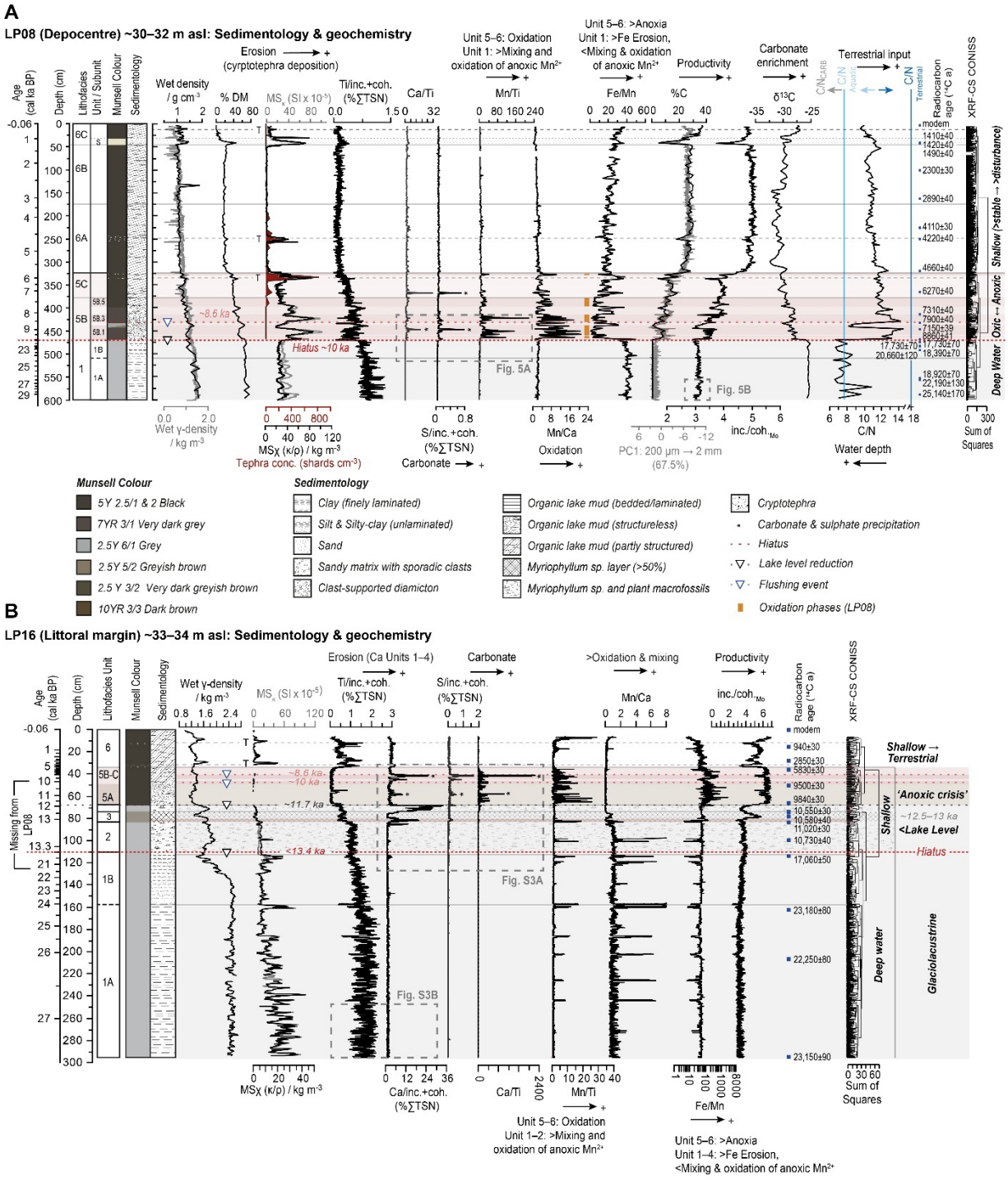

Figure 5. Summary sedimentology and geochemistry data for Lago Pato sediment records. **(A)** LP08 (depocentre site). **(B)** LP16 (littoral-catchment site). This figure integrates sedimentological observations, key core scanning parameters, ratios, and subsample data, and shows the main changes in key elements (Ti, Mn, Ca, Fe) and their ratios in both records. Data points between 68–62 cm in the LP08 record were not plotted or included in analysis due to low counts from an extrusion related surface gap. Data were plotted in C2 (Juggins, 2007) and in R, with the final layout achieved in Adobe Illustrator.

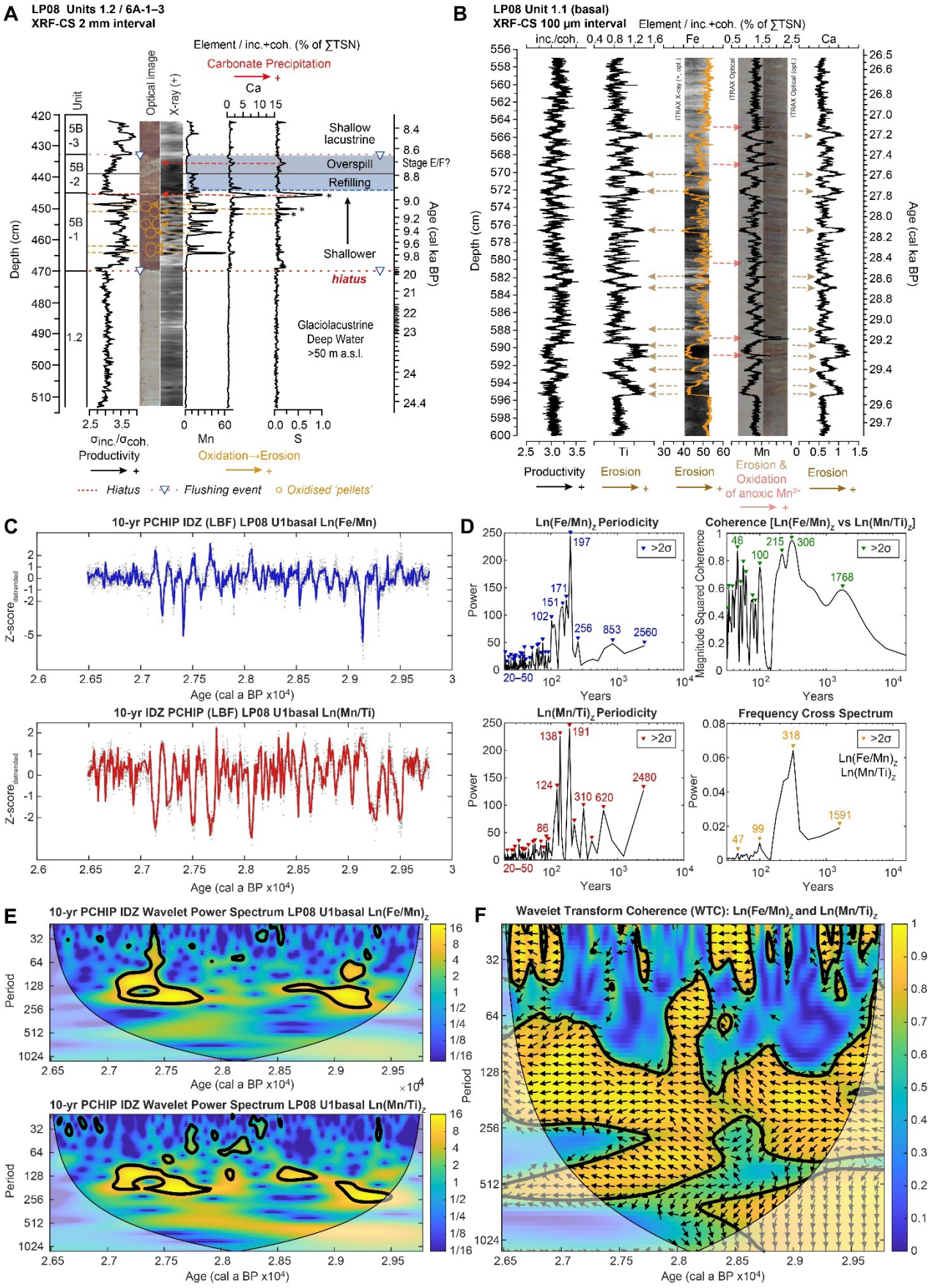

Figure 6. Key geochemical features of the LP08 XRF-CS record**. (A)** Close up of the Unit 1 / Unit 6 boundary showing the sharp boundary (hiatus) at ~470 cm depth (c. 10 cal ka BP) and Mn-rich nodules, and Ca- and S-rich layers associated with carbonate precipitation in a shallow water (arid) sedimentary environment. A short-lived phase of glacier readvance and reformation of

Palaeo-Lago Tehuelche–Puerto Consuelo to >40–<50 m a.s.l. might have occurred between 8.9–8.6 ka (Unit 5B-2). **(B)** Ultra-high-resolution (100 µm; 44 cm core length) XRF-CS data from the LP08 basal core section plotted against depth and weighted mean modelled age (SH20-M1H model). Variations in organic (inc./coh.), erosional (Ti/inc.+coh. and Ca/inc.+coh. as %TSN), redox (Mn/inc.+coh. as %TSN) geochemical ratios are shown. **(C)** Time series analysis of the 10-year PCHIP (Piecewise Cubic Hermite Interpolating Polynomial) interpolated $Ln(Fe/Mn)_{Z\text{-scores}}$ (blue line) and $Ln(Mn/Ti)_{Z\text{-scores}}$ (red line) and from the LP08 basal core section (B). The mean sample interval for the dataset (grey dots) is 0.75 ± 0.31 years. **(D)** Power spectrum periodicity, cross-coherence, and cross-spectrum bi-plots for $Ln(Fe/Mn)_{Z\text{-scores}}$ and $Ln(Mn/Ti)_{Z\text{-scores}}$ data from (C) with prominent (>2-sigma) decadal- to millennial-scale periodicities highlighted. MSC is Magnitude Squared Coherence. **(E)** Wavelet power spectrum and **(F)** wavelet transform coherence (WTC) plots (Grinsted et al., 2004) for $Ln(Fe/Mn)_{Z\text{-scores}}$ $Ln(Mn/Ti)_{Z\text{-scores}}$ from (C) showing decadal- to centennial-scale periodicity (Period, in years in E and F) and time-dependent changes in correlation (0–1 in F). WTC uses Monte Carlo methods to assess the statistical significance of cross-coherence against red noise in both time series. Significant (>95% confidence) decadal- to centennial-scale periodicities and correlations are outlined in black, with a strong and significant correlation for $Ln(Fe/Mn)_{Z\text{-scores}}$ $Ln(Mn/Ti)_{Z\text{-scores}}$. periodicities of 128–512 years between 30–26 ka. Directional arrows in (F) show that Ln(Fe/Mn) and Ln(Mn/Ti) are always anti-correlated. Data were plotted and analysed in C2 (Juggins, 2007) and Matlab, with the final layout achieved in Adobe Illustrator.

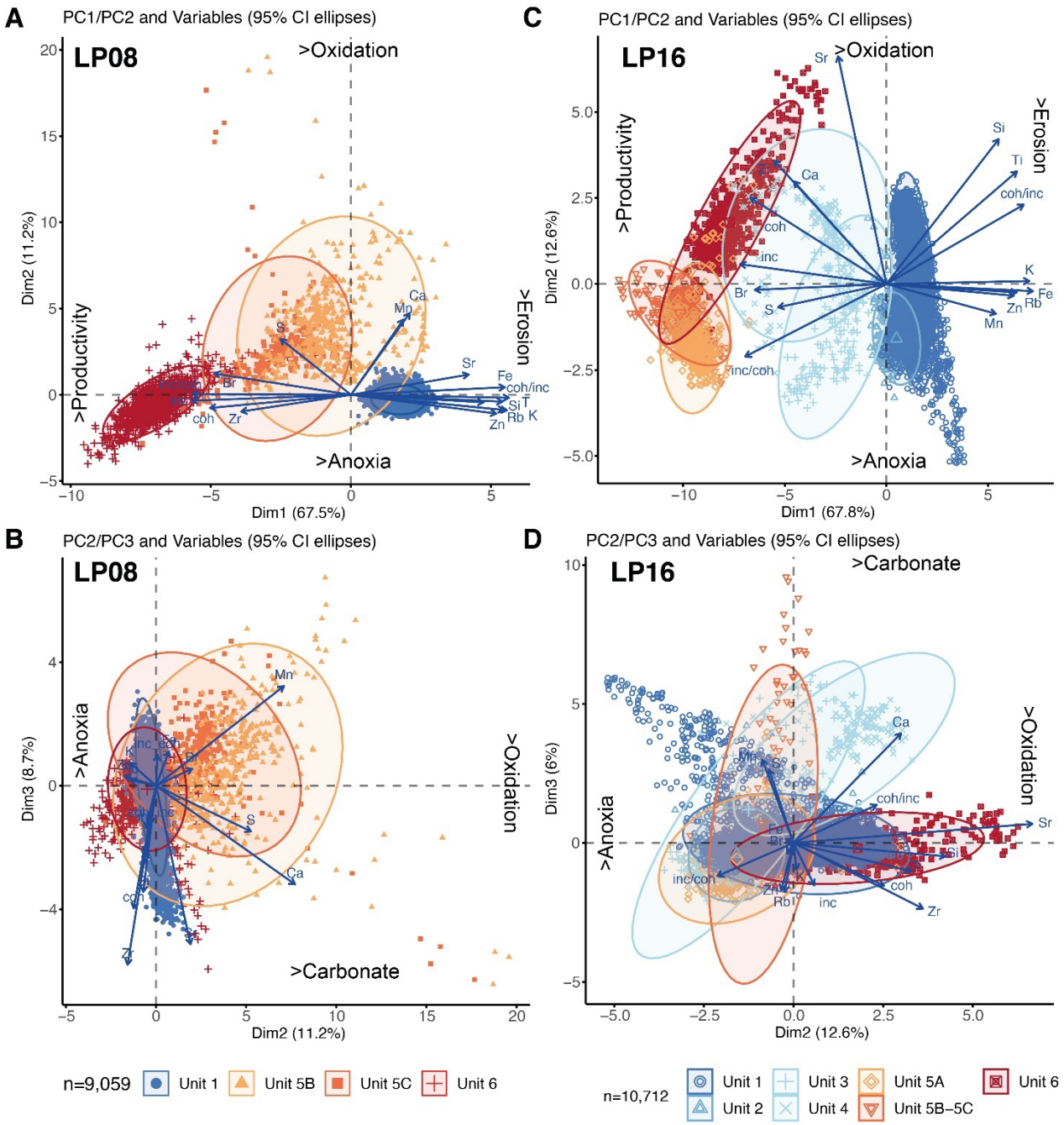

Figure 7. Principal component analysis (PCA) biplots and summary interpretation for: **(A)** LP08: PC1/ PC2. **(B)** LP08: PC1/PC3. **(C)** LP16: PC1/PC2. **(D)** LP16: PC1/PC3. Further analysis and PCA biplots are shown in Figures S2 and S3. 'As measured' 200 µm→2 mm element/total scatter XRF-CS datasets (expressed as percentage of total scatter normalised sum) were used. Data were $\log_n$ transformed, centred, and standardised, and then grouped by lithofacies units as defined by CONISS cluster analysis shown in Figure 5. Data were plotted and analysed in R, with the final layout achieved in Adobe Illustrator.

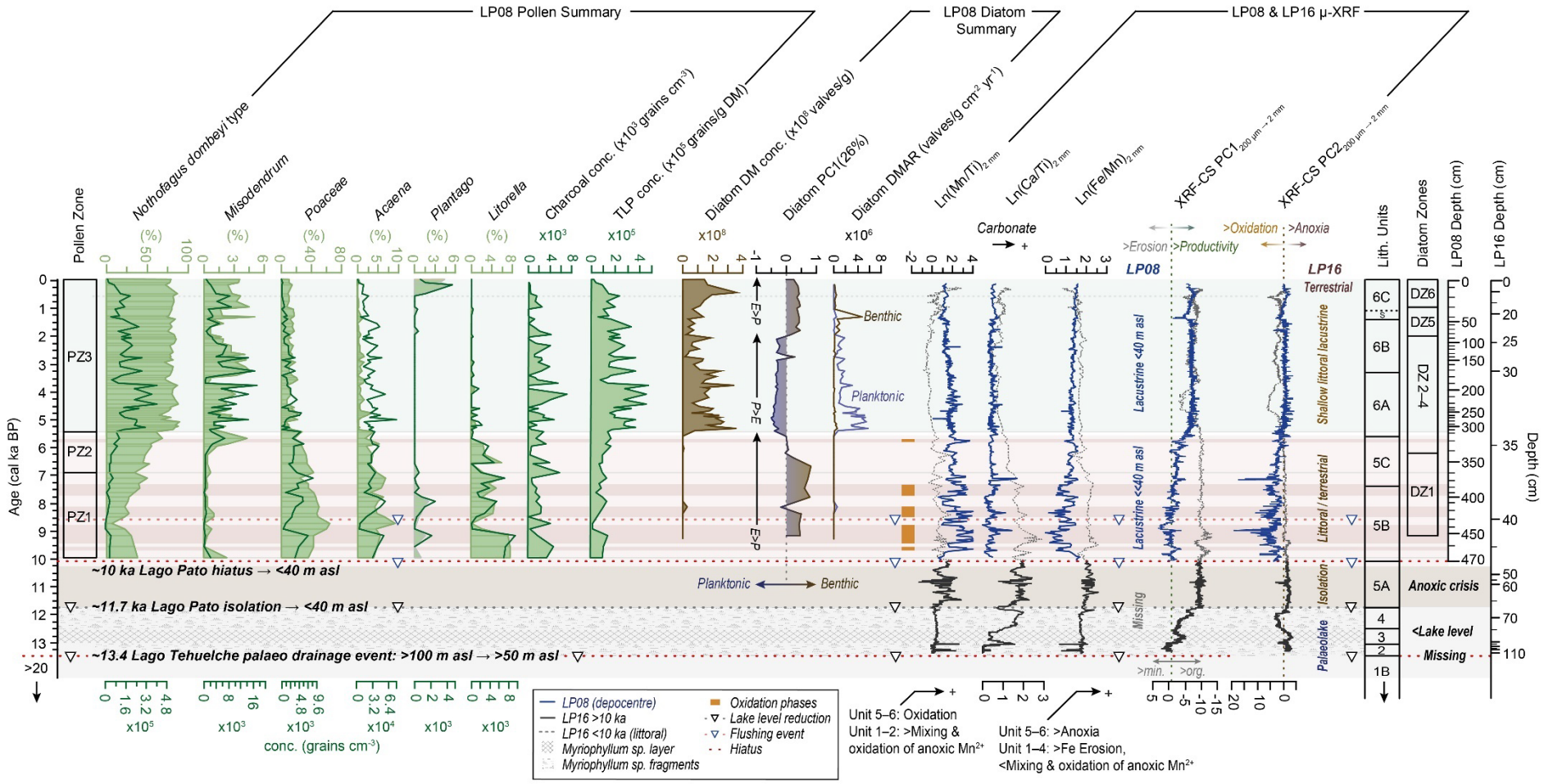

Figure 8. Summary key pollen and diatom compositional diagram for Holocene-age sediments in the LP08 record compared to key geochemical $\log_n$ ratios and Principal Component (PC1) profiles from the LP08 and LP16 records shown in Figures 5–7. DM = dry mass concentration, DMAR = dry mass accumulation rate. Data were plotted and analysed in C2 (Juggins, 2007), with the final layout achieved in Adobe Illustrator.

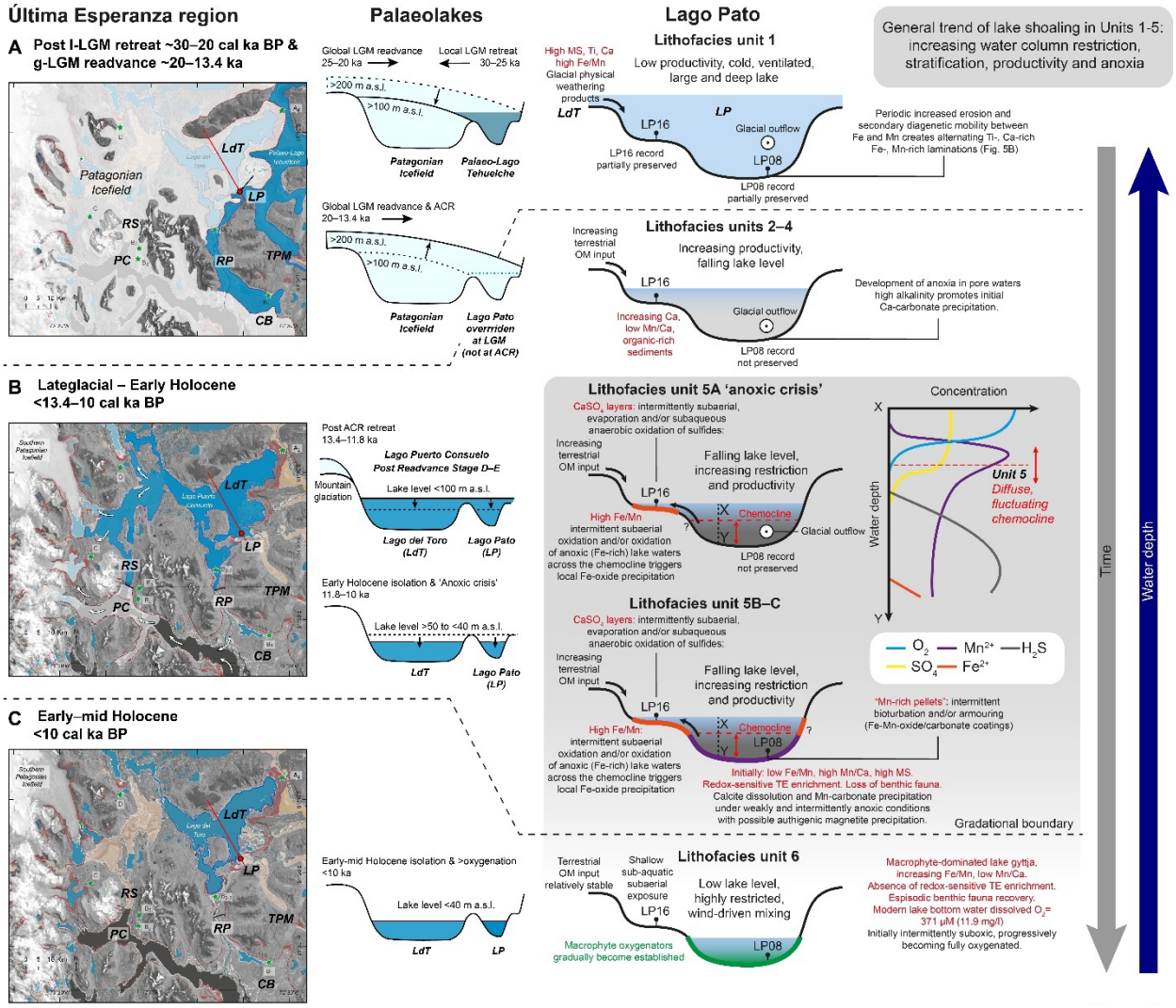

Figure 9. Schematic cartoon and lake ontogeny model illustrating changes in glacial activity, and its impact on the Lago del Toro lake level and development of Lago Pato and in the last ~30 ka. **(A)** Cross section across Lago del Toro (LdT) and Lago Pato (LP) during retreat from local LGM (l-LGM) glacial limits and during readvance to global LGM (g-LGM) limit. The outline of Palaeo-Lago Tehuelche (blue) formed after the l-LGM and the extent of the Southern Patagonia Icefield are adapted from García et al. (2014). PC is Puerto Consuelo, TPM is Tres Paso Moraine, CB is Cerro Benetiz, RS is Rio Serrano. **(B)** Palaeo-Lago Puerto Consuelo at c. 13.4–11.7 ka after the first major lake lowering event and during the early Holocene isolation of Lago del Toro and Lago Pato, between c. 11.7–10 ka. Isolation occurred when the palaeolake level fell below ~40 m a.s.l. after glaciers retreated from the Puerto Consuelo area, removing the ice-dam at ~50 m a.s.l. that retained the enlarged palaeolake over Lago del Toro and Lago Pato. Glacier limits shown in (B) are minima at c. 11.3 ka following retreat from advanced ACR positions along the Río Serrano (RS) and from the Cerro Benetiz (CB) area (adapted from García et al. (2014) and references therein). **(C)** Development of Lago Pato as an isolated basin <10 ka. Chemocline changes in the lithofacies model are based on the Brownie Lake profiles (Wittkop et al., 2020) with observations in black text and interpretations in red text. This figure was made in ARC-GIS and Adobe Illustrator.

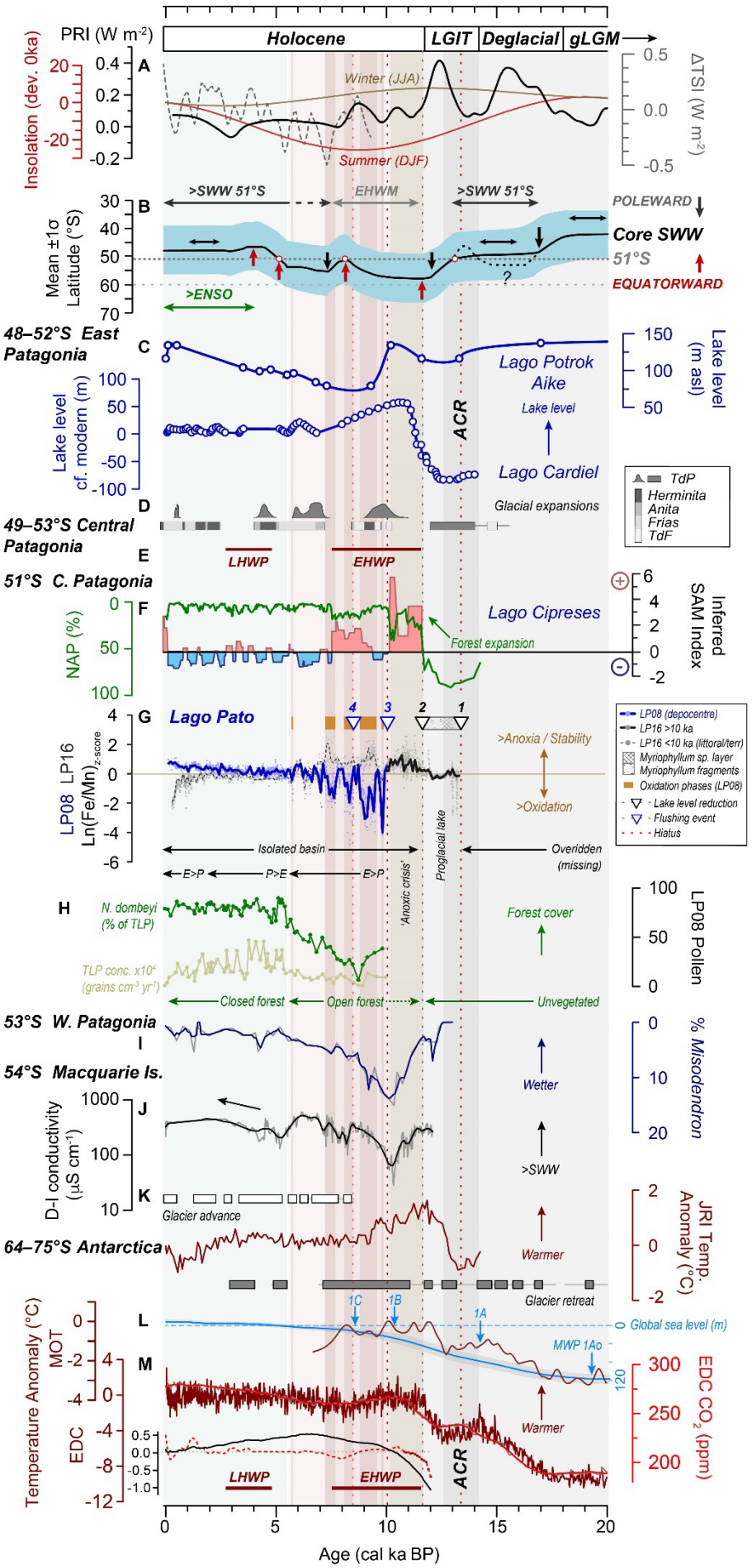
Holocene
LGIT
Deglacial
gLGM
PRI (W m-2)
Insolation (dev. 0ka)
A
Winter (JJA)
Summer (DJF)
ΔTSI (W m-2)
>SWW 51°S
EHWM
>SWW 51°S
POLEWARD
Core SWW
51°S
EQUATORWARD
Mean ±1σ Latitude (°S)
B
>ENSO
48–52°S East Patagonia
C
Lago Potrok Aike
Lake level
Lago Cardiel
Lake level (m asl)
Lake level cf. modern (m)
ACR
D
Glacial expansions
TdP
Herminita
Anita
Frías
TdF
49–53°S Central Patagonia
E
LHWP
EHWP
51°S C. Patagonia
F
Lago Cipreses
Forest expansion
NAP (%)
Inferred SAM Index
G
Lago Pato
4
3
2
1
>Anoxia / Stability
>Oxidation
LP08 LP16 Ln(Fe/Mn)z-score
Isolated basin
Overidden (missing)
E>P
P>E
E>P
Proglacial lake
'Anoxic crisis'
LP08 (depocentre)
LP16 >10 ka
LP16 <10 ka (littoral/terr)
Myriophyllum sp. layer
Myriophyllum fragments
Oxidation phases (LP08)
Lake level reduction
Flushing event
Hiatus
H
N. dombeyi (% of TLP)
TLP conc. x10⁴ (grains cm⁻³ yr⁻¹)
Forest cover
LP08 Pollen
Closed forest
Open forest
Unvegetated
53°S W. Patagonia
I
Wetter
% Misodendron
54°S Macquarie Is.
J
>SWW
D-I conductivity (µS cm-1)
K
Glacier advance
64–75°S Antarctica
Warmer
JRI Temp. Anomaly (°C)
Glacier retreat
1C
1B
1A
L
Global sea level (m)
MWP 1Ao
M
Warmer
Temperature Anomaly (°C)
MOT
EDC
LHWP
EHWP
ACR
EDC CO2 (ppm)
0
5
10
15
20
Age (cal ka BP)

Figure 10. Regional-global driving mechanisms of glacier dynamics and palaeoclimatic change compared with lake level change in Patagonia and the Fe/Mn (redox) record from Lago Pato over the last 20 cal ka BP. **(A)** Total Solar Irradiance deviation (ΔTSI; dashed grey line) from present day value (a solar forcing parameter based on variations in ^{10}Be isotope data from ice cores) (Steinhilber et al., 2009); austral winter insolation (June-July-August, JJA; brown line) and summer insolation (December-January-February, DJF; red line) at 51°S (Laskar et al., 2004); the planetary radiative imbalance at the top of the atmosphere (PRI; solid black line). This is principal driver of global climate change defined as the difference between the total insolation absorbed at the top of the atmosphere and the amount of energy radiated back into space (Baggenstos et al., 2019). **(B)** Hypothetical representation of the mean annual latitudinal position of the core SWW intensity belt and an approximate 1σ latitudinal range of enhanced precipitation associated with it (Ariztegui et al., 2010; Quade and Kaplan, 2017). Figure adapted from Quade and Kaplan (2017) to include a northward shift in the SWW, driving glacier readvance in the TdP region and between 50–55°S during the ACR. The grey dotted line is 51°S; dark grey horizontal arrows represent phases of increased SWW; light grey horizontal arrows represent the Early Holocene Westerlies Minimum (EHWM) ~11.5–7.5 ka (Moreno et al., 2021), which drove the reduction in atmospheric CO_2 between 10–8 ka shown in (M). Black arrows represent poleward (or less diffuse) or stable SWW, dark red arrows represent equatorward (or more diffuse) SWW. Selected regional records between ~49-53°S that follow are shown in order from east to west across Patagonia and from north to south: **(C)** Lake level changes at Potrok Aike, a closed basin ~150 km southeast of Lago Pato (Zolitschka et al., 2013), and Lago Cardiel, ~280 km north of Lago Pato in central (Argentinean) Patagonia. Increased lake levels at the latter during the Late glacial have been linked to stronger SWW and increased precipitation between 48–52°S. For Potrok Aike, increased precipitation and higher lake levels during the EHWM were associated with the incursion of the Easterlies (Ariztegui et al., 2010; Zolitschka et al., 2013). **(D)** Compilation of cosmogenic surface exposure dating constraints on glacier expansion for Southern Patagonia and Tierra del Fuego (adapted from Darvill et al. (2015), Kaplan et al. (2020). **(E)** Summary timing of the Early Holocene Warm Period (EHWP) and the Late Holocene Warm Period (LHWP) (Marcott et al., 2013; Kaufman et al., 2020). **(F)** Inferred Holocene SAM-index from positive (red) to negative (blue) SAM-like states overlain by the Northern Arboreal Pollen (NAP) percentage plot from Lago Cipreses, ~11 km WNW of Lago Pato (Moreno et al., 2018; Kaplan et al., 2020). **(G)** LP08 and LP16 Ln(Fe/Mn) ratios as Z-scores representing anoxia/stability ↔ oxidation/instability in Lago Pato. The solid blue (LP08) and solid/dashed black (LP16) lines are a 100-year interval Piecewise Cubic Hermite Interpolating Polynomial (PCHIP) smoothing of measured interval data (light blue, LP08, and grey, LP16, circles). Downward black triangles denote lake level reductions at (1) c. 13.4, (2) 11.7 ka in LP16. Downward blue triangles represent flushing events at c. 10 ka (3, erosional hiatus) and c. 8.6 ka (4, refilling/emptying event) in the LP08 depocentre record. **(H)** Percentage count data for *Nothofagus dombeyi type* and Total Land Pollen (TLP) concentrations as proxies for changes in vegetational cover in the Lago Pato catchment over the last c. 10 cal ka BP and a summary of the inferred precipitation: evaporation (P:E) balance, based on the LP08 PC1 axis diatom data (Figure 8); **(I)** Relative percentages changes in *Misodendrum* (mistletoes commonly found on deciduous *Nothofagus* species) in sediment records from the western Andes (Lamy et al., 2010; Fletcher and Moreno (2012) interpretation). **(J)** Changes in diatom-inferred (D-I) conductivity from Macquarie Island (Saunders et al., 2018) as an indicator of increasing SWW at ~54°S. The black line is a 100-year LOESS smoothing of as measured D-I data (grey line). **(K)** A compilation of the timing of glacier advance and retreat on the northern Antarctic Peninsula (Kaplan et al., 2020) and temperature anomaly data from the James Ross Island ice core record (Mulvaney et al., 2012). **(L)** Global Mean Ocean Temperature (MOT) 20–6.5 cal ka BP (Bereiter et al., 2018) and a stacked global mean sea level curve 20–0 ka (Spratt and Lisiecki, 2016). **(M)** Atmospheric CO_2 concentrations (100-year LOESS smoothing (red line) of raw data (grey line) and temperature anomaly data from the EPICA Dome C ice core record in Antarctica (dark red line) (Monnin et al., 2001; Jouzel et

al., 2007), Holocene palaeotemperature compilation of median temperature anomalies (relative to 1800–1900 CE) for 60–90 °S (dashed red line), and globally (black line) (Kaufman et al., 2020) and a summary of the main Holocene warm periods at 30–90°S (Marcott et al., 2013) (dark red bars). The grey dotted line is the median 12-kyr temperature value for 60–90 °S (0.02); 5th (-2.21) and 95th (1.51) error percentiles are out of the plotting range. The background shading in this figure summarises the timing of the key features in the Lago Pato record as follows: green shading represents a late Holocene phase of enhanced ENSO (El Niño Southern Oscillation); light red shading represents more arid conditions; dark red shading with orange bars represents enhanced oxidation phases; light brown shading represents the 'Anoxic crisis'; light grey shading represents glaciogenic deposits; dark grey shading indicating the time period covered by the Antarctic Cold Reversal (ACR: 14.6–12.8 ka). Data in this figure were analysed and plotted in Sigmaplot and R, with the final layout achieved in Adobe Illustrator.

Table 1. Geomorphological data collected from Lago Pato. Data marked with an asterisk were calculated by subtracting the mean Google Earth offset (6.70 ± 5.95 m) from GPS measured data. Field measurements were undertaken using a Trimble 5700 GPS in December 2015, with a tripod height correction of 0.523 m using WGS84 as the reference ellipsoid, corrected using the EGM96 geoid model. Calculated elevations are shown to three decimal places, but precision is one decimal place at best.

ID	Location description	Latitude (°S)	± 2σ (m)	Longitude (°W)	± 2σ (m)	WGS84 Ellipsoidal height (m)	± 2σ (m)	Geoid height (m)	Uncorrected elevation (m a.s.l.)	Corrected elevation (m a.s.l.)	Google Earth alt. (m a.s.l.)	Google Earth offset (m)
LP1	NW Sill to Lago del Toro 1	51°17' 53.4218"	0.215	72°40' 55.1173"	0.288	51.397	0.398	13.02	38.377	37.854	41	3.15
LP2	NW sill to Lago del Toro 2	51°17' 53.4196"	0.044	72°40' 55.1224"	0.097	51.508	0.145	13.02	38.488	37.965	41	3.04
LP3	LP16 coring site	51°18' 11.3293"	0.059	72°40' 53.6633"	0.107	46.682	0.112	13.01	33.672	33.149	40	6.85
LP4	S sill towards wetland	51°18' 16.7246"	0.067	72°40' 45.9815"	0.113	46.914	0.126	13.00	33.914	33.391	40	6.61
LP5	NE edge of Lago Pato	51°17' 59.4762"	0.044	72°40' 39.4845"	0.136	49.497	0.210	13.01	36.487	32.686	43	10.31
LP6	LP08 coring site	51°18' 01.2000"	-	72°40' 42.9600"	-	-	-	-	-	32.297*	39	-

Table 2. Summary descriptions and interpretations of the lithofacies units in the Lago Pato LP08 and LP16 records.

Record	**Unit Subunit**	**Depth (cm)**	**Modelled Age Range** (cal a BP ± 95% CI)	**Summary lithological description**	**Summary Interpretation**	**Lake history and palaeoclimate** *SWW position and movement*
LP08 LP16	1	600–470 295–112 [112–110 hiatus]	29,800 ± 1,020 –21,230 ± 520 27,530 ± 270 –20,490 ± 350	Light grey, finely laminated glaciolacustrine silty clay with pale greyish -orange layers enriched in Ti and Ca. The lowermost laminated sub-unit (1A) grades into a paler green-grey massive sub-unit (1B). In LP08, a sharp erosional upper boundary separates Unit 1 and Unit 5B at 470 cm. Units 2–5A are missing from LP08. In LP16, step changes to lower MS values separate sub-units 1A and 1B at 187 cm (25.5 cal ka BP) and Unit 1 and 2 at ~110 cm (20.4 cal ka BP).	Unit 1 represents the 'background' glaciogenic detrital composition, with well-developed fine scale internal structure, most notably within Unit 1A, and dominated by glaciogenic physical weathering products associated with allochthonous catchment erosion. Fine grey (glaciogenic) laminations are enriched in Fe and Mn reflecting reduced conditions and/or the decomposition of organic matter at the sediment water interface.	**Lago del Toro and Lago Pato were part of a larger proglacial Palaeo-Lago Tehuelche after the l-LGM and before the g-LGM.** **Lago Pato was overridden at the g-LGM.** *SWW: N of 51 °S, limited latitudinal movement in run up to g-LGM*
LP16	2	110–83	13,390 ± 640 –13,060 ± 390	Unit 2 has similar sedimentological characteristics to the upper parts of Unit 1 but is distinguished by the lack of well-defined orange-brown banding and the presence of embedded fine subaquatic *Myriophyllum sp.* fragments.	Glaciogenic physical weathering products associated with allochthonous catchment erosion. Embedded sub-aquatic macrofossils imply a shallower environment than Unit 1	**First substantial lake level reduction at c. 13.4 ka: shallow, >productive lake (lake level: >100 m asl → <50 m asl)** SWW: At 51 °S, moving S from ACR SWW peak north of 51 °S at c. 13.5 ka
LP16	3	83–74	13,070 ± 390 –12,500 ± 220	Unit 3 is composed entirely of subaquatic *Myriophyllum sp*.	Shallower and more productive glaciogenic environment	A further reduction in lake level between c. 13.0–12.5 cal ka BP following glacier retreat after the ACR. *SWW: S of 51 °S, moving S*
LP16	4	74–67	12,500 ± 220 –11,720 ± 280	Unit 4 has a similar composition to Unit 2 but has increasingly elevated Ca and Sr and a reduced density of subaquatic *Myriophyllum sp*.	Shallower and more productive glaciogenic environment with authigenic precipitation (or redeposition) of Ca-, Sr-rich deposits. Still connected to Lago del Toro	**Gradual refilling of Lago Pato while still connected to Lago del Toro** SWW: S 51 °S, moving N
LP16	5A	67–47	11,720 ± 280 –10,120 ± 190	Unit 5 is structureless organic lake mud characterized by fluctuating Fe/Mn and Mn/Ti, with Ca and S peaks. Subunits 5A–C in LP16	Shallow-littoral environment isolated from glaciogenic inputs from Lago del Toro at 11.7 ka.	**Second major lake level reduction between at c. 11.7 cal ka BP, continuing until complete isolation from Lago del**

	5B/C	47–35	10,120 ± 190 –5,720 ± 130	characterised by exceptionally elevated (>+2σ) Fe/Mn and Mn/Ti between c. 11.7–10 cal ka BP (Unit 5A) and c. 8.4–7 cal ka BP. Subunits 5B and C are characterised lower but still elevated Fe/Mn and Mn/Ti ratios, and higher C/N values than Unit 1. Elevated Fe/Mn ratios reflecting minerogenic input are correlated with Mn/Ti ratios.	Unit 5A represents an 'Anoxic Crisis' with the eventual loss of benthic diatoms within the lake. Units 5B & C represent a more restricted shallow and productive basin, with increased input of terrestrial vegetation ad periodic oxic phases consisting of Mn-oxides and co-precipitated hydroxides.	**Toro at c. 11.3 cal ka BP (lake level: <50 m asl → <40 m asl). Erosional and overspill/flushing events (or, less likely, palaeolake reformation and emptying) at c. 10 ka and c. 8.9–8.6 ka?** *SWW: S 51 °S, moving N back over 51 °S by 8 ka*
LP08	5B	470–378	10,160 ± 480 –7,370 ± 290			
	5C	378–324	7,370 ± 290 –5,600 ± 250			
LP08	6A	324–175	5,600 ± 250 – 3,310 ± 330	Highly organic, structureless and increasingly fibrous macrophytic lake mud with low Mn/Ti ratios divided into subunits at 175 cm by a reduction in Mn (6B), and at 45 cm by a ~15 cm thick Sr-rich inwash sand layer (6c).	Significant Mn-enrichment, with sporadic Mn and Ca peaks implying that Lago Pato was occasionally shallow and highly anoxic well into the mid Holocene. Increasing Fe/Mn ratios reflect a general increase in anoxia linked greater stability and lake infilling.	**Shift to more persistently wet conditions with increased turbulence in the last 2 ka. LP16 became a subaerial environment in the last 200 years.** *SWW: marginally north of 51 °S and generally stable; increased ENSO influence*
	6B	175–45	3,310 ± 330 – 1,380 ± 130			
	6C	45–0	1,380 ± 130– -60 ± 3			
LP16	6A–C	35–0	5,720 ± 130 – -10 ± 1			

Table 3. Radiocarbon dating data for the LP08 and LP16 records. Aw = acid wash; a/a/a = acid-alkali-acid pre-treatment; M=Macrofossil age; P=paired bulk-macrofossil ages; R = age reversal and length of reversal in years in brackets. Reasons for rejection: X-a = Organic sediments emplaced on extraction; X-b = Drag down of younger roots during coring

No.	Lab ID	Core ID & section depth (cm)	Strat. Depth (cm)	Carbon source: pre-treatment	$\delta^{13}C_{IRMS}$ (‰)	^{14}C (ab. pMC) (% mod. ± 1σ)	C-14 age (^{14}C a ± 1σ)	SH20 calibrated ages (cal a BP) [2σ, 95.4% probability] max.–min.	Mean ± 1σ	Median	Notes
1	SUERC-20903	LP08-SC 1.5-2.0	1.5–2	Macrophytic lake mud: aw	-27.8	104.09 ± 0.45	-	-6 – -70	-15 ± 19	-7	
2	BETA-281397	LP08-1A:26.5-27	39.5–40	Macrophytic lake mud: aw	-26.9	83.9 ± 0.42	1410 ± 40	1360–1170	1270 ± 50	1280	
3	BETA-283772	LP08-SC:40 M	40–41	Plant material: a/a/a	-28.5	83.8 ± 0.42	1420 ± 40	1360–1170	1280 ± 50	1290	P
4	BETA-281396	LP08-SC:40 B	40–41	Macrophytic lake mud: aw	-29.2	83.07 ± 0.41	1490 ± 40	1410–1280	1340 ± 30	1340	P
5	BETA-476098	LP08-1A:81-82	100.2–101.3	Macrophytic lake mud: aw	-30.0	75.1 ± 0.28	2300 ± 30	2350–2140	2240 ± 60	2220	
6	BETA-281398	LP08-1B: 48-48.5	162–162.5	Macrophytic lake mud: aw	-31.1	69.78 ± 0.35	2890 ± 40	3150–2850	2980 ± 70	2970	
7	BETA-476104	LP08-1C: 53-54	225.2–226.2	Macrophytic lake mud: aw	-31.5	59.95 ± 0.22	4110 ± 30	4810–4420	4590 ± 100	4570	
8	BETA-281399	LP08-1C: 78-78.5	250–250.5	Plant material: a/a/a	-29.5	59.14 ± 0.29	4220 ± 40	4850–4570	4710 ± 80	4720	M
9	BETA-281400	LP08-1D: 69-69.5	319.6–320.1	Macrophytic lake mud: aw	-29.2	55.98 ± 0.28	4660 ± 40	5480–5060	5370 ± 90	5390	
10	BETA-281402	LP08-1E: 30-31	365.4–366.4	Plant material: a/a/a	-30.8	45.82 ± 0.23	6270 ± 40	7260–6990	7130 ± 80	7120	M
11	BETA-288873	LP08-1E 79-80	414.4–415.4	Organic-rich sediment: aw	-27.8	40.25 ± 0.20	7310 ± 40	8180–7980	8090 ± 50	8100	
12	SUERC-20906	LP08-1F: 10-11	432–433	Organic-rich sediment: aw	-28.3	37.38 ± 0.19	7900 ± 40	8980–8540	8690 ± 100	8670	R (-720)
13	SUERC-20907	LP08-1F: 25-26	447–448	Organic-rich sediment: aw	-27.7	41.05 ± 0.20	7150 ± 39	8020–7840	7930 ± 50	7940	
14	SUERC-20909	LP08-1F: 46-47	468–469	Organic-rich sediment: aw	-28.7	33.20 ± 0.17	8860 ± 41	10160–9680	9900 ± 130	9880	
15	BETA-281403	LP08-1F:52.5-53	474.5–475.5	Glaciogenic clay-rich sediment: aw	-25.2	11.00 ± 0.10	17,730 ± 70	21,790–21090	21,450 ± 180	21,430	
16	BETA-281405	LP08-1G:17.5-18	483.5–484	Glaciogenic clay-rich sediment: aw	-25.2	11.03 ± 0.10	17,710 ± 70	21,760–21050	21,400 ± 180	21,390	
17	BETA-281404	LP08-1F:61.5-62	483.5–484.5	Glaciogenic clay-rich sediment: aw	-24.9	10.13 ± 0.09	18,390 ± 70	22,440–22130	22,290 ± 70	22,300	
18	BETA-271299	LP08-1G 26-27	492–493	Glaciogenic clay-rich sediment: aw	-25.6	7.64 ± 0.11	20,660 ± 120	25,200–24370	24,830 ± 190	24,850	
19	BETA-281406	LP08-1H:46-46.5	554.2–554.7	Glaciogenic clay-rich sediment: aw	-24.8	9.49 ± 0.08	18,920 ± 70	22,990–22550	22,790 ± 120	22,800	R (-3,600)
20	BETA-271298	LP08-1H 48-49	556.2–557.2	Glaciogenic clay-rich sediment: aw	-25.5	6.31 ± 0.10	22,190 ± 130	26,910–25990	26,420 ± 250	26,380	
21	BETA-271297	LP08-1I 33-34	589.4–590.4	Glaciogenic clay-rich sediment: aw	-25.3	4.37 ± 0.09	25,140 ± 170	29,910–29050	29,440 ± 230	29,420	
22	BETA-480157	LP16-1C(SUR)_0-2	0–2	Plant material: a/a/a	-27.8	103.2 ± 0.40	-	-6 – -7	-6 ± 1	-6	M

23	BETA-480156	LP16-1C(SUR)_15-16	15–16	Organic-rich sediment: aw	-27.8	88.96 ± 0.33	940 ± 30	910–730	820 ± 50	800	
24	BETA-476093	LP16-1A: 0-1	28–29	Organic-rich sediment: aw	-28.2	70.13 ± 0.26	2850 ± 30	3060–2780	2920 ± 60	2920	
25	BETA-476099	LP16-1A: 8-9	36–37	Organic-rich sediment: aw	-29.7	48.4 ± 0.18	5830 ± 30	6730–6480	6590 ± 50	6590	
26	BETA-476094	LP16-1A: 22-23	50–51	Organic-rich sediment: aw	-28.7	30.65 ± 0.11	9500 ± 30	11,070–10,570	10,720 ± 110	10,700	
27	BETA-476095	LP16-1A: 38-39	66–67	Glaciogenic clay-rich sediment: aw	-31.4	29.38 ± 0.11	9840 ± 30	11,260–11,170	11,220 ± 20	11,220	
28	BETA-476100	LP16-2A: 20-21 M	74–74.5	*Myriophyllum sp.* aq. moss; a/a/a	-33.0	26.89 ± 0.10	10,550 ± 30	12,620–12,470	12,550 ± 60	12,550	P
29	BETA-476101	LP16-2A: 20-21 B	74–74.5	Glaciogenic grey clay-rich sediment: aw	-27.1	26.79 ± 0.13	10,580 ± 40	12,690–12,470	12,560 ± 70	12,550	P
30	BETA-476096	LP16-2A: 24-24.5_M	78–78.5	*Myriophyllum sp.* aq. moss layer; a/a/a	-36.3	25.36 ± 0.09	11,020 ± 30	13,070–12,780	12,900 ± 60	12,900	M
32	BETA-480158	LP16-2A_46-M	100–100.5	*Myriophyllum sp.* aq. moss; a/a/a	-30.5	26.3 ± 0.13	10,730 ± 40	12,750–12,620	12,700 ± 30	12,710	M
33	BETA-476102	LP16-2B: 22-23	114–115	Glaciogenic clay-rich sediment: aw	-25.0	11.96 ± 0.07	17,060 ± 50	20,780–20,430	20,580 ± 90	20,560	
34	BETA-480160	LP16-3A_33	162–163	Glaciogenic clay-rich sediment: aw	-25.2	5.58 ± 0.06	23,180 ± 80	27,650–27,250	27,420 ± 110	27,400	
35	BETA-476103	LP16-3B: 38-39	206.8–207.8	Glaciogenic clay-rich sediment: aw	-25.1	6.27 ± 0.06	22,250 ± 80	26,920–26,120	26,540 ± 200	26,480	
36	BETA-476097	LP16-4B: 47-48	294.52–295.5	Glaciogenic clay-rich sediment: aw	-25.5	5.6 ± 0.06	23,150 ± 90	27,640–27,230	27,400 ± 110	27,370	
-	SUERC-20910	LP08-LP08-1I: 51-52	607.4–608.4	Organic sediment: acid washes	-29.3	39.52 ± 0.20	7460 ± 40	8370–8050	8250 ± 60	8260	X-a
-	SUERC-20911	LP08-1I: 55-56	611.4–612.4	Organic sediment: acid washes	-29.1	40.34 ± 0.18	7290 ± 40	8180–7970	8080 ± 60	8080	X-a
31	BETA-480159	LP16-2A: 30-30.5_M	84–84.5	Plant root material (terrestrial); a/a/a	-27.5	37.68 ± 0.14	7840 ± 30	8690–8450	8570 ± 50	8570	X-b

References

Abram, N.J., Mulvaney, R., Vimeux, F., Phipps, S.J., Turner, J., and England, M.H. (2014). Evolution of the Southern Annular Mode during the past millennium. *Nature Climate Change* 4**,** 564-569.

Aller, R.C., and Rude, P.D. (1988). Complete oxidation of solid phase sulfides by manganese and bacteria in anoxic marine sediments. *Geochimica et Cosmochimica Acta* 52**,** 751-765.

Altenberger, U., Oberhansli, R., Putlitz, B., and Wemmer, K. (2003). Tectonic controls and Cenozoic magmatism at the Torres del Paine, southern Andes (Chile, 51 degrees 10'S). *Revista Geologica De Chile* 30**,** 65-81.

Aniya, M. (2013). Holocene glaciations of Hielo Patagonico (Patagonia Icefield), South America: A brief review. *Geochemical Journal* 47**,** 97-105.

Ariztegui, D., Gilli, A., Anselmetti, F.S., Goñi, R.A., Belardi, J.B., and Espinosa, S. (2010). Lake-level changes in central Patagonia (Argentina): crossing environmental thresholds for Lateglacial and Holocene human occupation. *Journal of Quaternary Science* 25**,** 1092-1099.

Baggenstos, D., Häberli, M., Schmitt, J., Shackleton, S.A., Birner, B., Severinghaus, J.P., Kellerhals, T., and Fischer, H. (2019). Earth's radiative imbalance from the Last Glacial Maximum to the present. *Proceedings of the National Academy of Sciences* 116**,** 14881-14886.

Barret, S. (2021). ggobi/ggally: v2.1.2. *doi: 10.5281/zenodo.5009047*.

Bennion, H., Sayer, C.D., Tibby, J., and H.J., C. (2010). "Diatoms as indicators of environmental change in shallow lakes," in *The Diatoms: Applications for the Environmental and Earth Sciences,* eds. J.P. Smol & E.F. Stoermer. 2nd ed: Cambridge University Press), 152-173.

Bereiter, B., Shackleton, S., Baggenstos, D., Kawamura, K., and Severinghaus, J. (2018). Mean global ocean temperatures during the last glacial transition. *Nature* 553**,** 39-44.

Bertrand, S., Hughen, K., Sepúlveda, J., and Pantoja, S. (2014). Late Holocene covariability of the southern westerlies and sea surface temperature in northern Chilean Patagonia. *Quaternary Science Reviews* 105**,** 195-208.

Bertrand, S., Lange, C.B., Pantoja, S., Hughen, K., Van Tornhout, E., and Wellner, J.S. (2017). Postglacial fluctuations of Cordillera Darwin glaciers (southernmost Patagonia) reconstructed from Almirantazgo fjord sediments. *Quaternary Science Reviews* 177**,** 265-275.

Bigler, C., Grahn, E., Larocque, I., Jeziorski, A., and Hall, R. (2003). Holocene environmental change at Lake Njulla (999 m asl), northern Sweden: a comparison with four small nearby lakes along an altitudinal gradient. *Journal of Paleolimnology* 29**,** 13-29.

Bishop, T. (2021). itraxR: Itrax Data Analysis Tools. *https://CRAN.R-project.org/package=itraxR*.

Blaauw, M., and Christen, J.A. (2011). Flexible paleoclimate age-depth models using an autoregressive gamma process. *Bayesian Analysis* 6**,** 457-474.

Blunier, T., Schwander, J., Stauffer, B., Stocker, T., Dällenbach, A., Indermühle, A., Tschumi, J., Chappellaz, J., Raynaud, D., and Barnola, J.-M. (1997). Timing of the Antarctic cold reversal and the atmospheric CO2 increase with respect to the Younger Dryas Event. *Geophysical Research Letters* 24**,** 2683-2686.

Bronk Ramsey, C. (2016). Development of the Radiocarbon Calibration Program. *Radiocarbon* 43**,** 355-363.

Calvert, S.E., and Pedersen, T.F. (1996). Sedimentary geochemistry of manganese; implications for the environment of formation of manganiferous black shales *Economic Geology* 91**,** 36-47.

Caniupán, M., Lamy, F., Lange, C.B., Kaiser, J., Kilian, R., Arz, H.W., León, T., Mollenhauer, G., Sandoval, S., De Pol-Holz, R., Pantoja, S., Wellner, J., and Tiedemann, R. (2017). Holocene sea-surface temperature variability in the Chilean fjord region. *Quaternary Research* 82**,** 342-353.

Damman, A.W.H. (1978). Distribution and Movement of Elements in Ombrotrophic Peat Bogs. *Oikos* 30**,** 480-495.

Darvill, C.M., Bentley, M.J., Stokes, C.R., Hein, A.S., and Rodés, Á. (2015). Extensive MIS 3 glaciation in southernmost Patagonia revealed by cosmogenic nuclide dating of outwash sediments. *Earth and Planetary Science Letters* 429**,** 157-169.

Davies, B.J., Darvill, C.M., Lovell, H., Bendle, J.M., Dowdeswell, J.A., Fabel, D., García, J.-L., Geiger, A., Glasser, N.F., Gheorghiu, D.M., Harrison, S., Hein, A.S., Kaplan, M.R., Martin, J.R.V., Mendelova, M., Palmer, A., Pelto, M., Rodés, Á., Sagredo, E.A., Smedley, R.K., Smellie, J.L., and Thorndycraft, V.R. (2020). The evolution of the Patagonian Ice Sheet from 35 ka to the present day (PATICE). *Earth-Science Reviews* 204**,** 103152.

Davies, S.J., Lamb, H.F., and Roberts, S.J. (2015). "Micro-XRF Core Scanning in Palaeolimnology: Recent Developments," in *Micro-XRF Studies of Sediment Cores,* eds. I.W. Croudace & R.G. Rothwell. (Dordrecht: Springer Netherlands), 189-226.

Dee, D.P., Uppala, S.M., Simmons, A.J., Berrisford, P., Poli, P., Kobayashi, S., Andrae, U., Balmaseda, M.A., Balsamo, G., Bauer, P., Bechtold, P., Beljaars, A.C.M., Van De Berg, L., Bidlot, J., Bormann, N., Delsol, C., Dragani, R., Fuentes, M., Geer, A.J., Haimberger, L., Healy, S.B., Hersbach, H., Hólm, E.V., Isaksen, L., Kållberg, P., Köhler, M., Matricardi, M., Mcnally, A.P., Monge-Sanz, B.M., Morcrette, J.J., Park, B.K., Peubey, C., De Rosnay, P., Tavolato, C., Thépaut, J.N., and Vitart, F. (2011). The ERA-Interim reanalysis: configuration and performance of the data assimilation system. *Quarterly Journal of the Royal Meteorological Society* 137**,** 553-597.

Dickens, W.A., Kuhn, G., Leng, M.J., Graham, A.G.C., Dowdeswell, J.A., Meredith, M.P., Hillenbrand, C.D., Hodgson, D.A., Roberts, S.J., Sloane, H., and Smith, J.A. (2019). Enhanced glacial discharge from the eastern Antarctic Peninsula since the 1700s associated with a positive Southern Annular Mode. *Scientific Reports* 9**,** 14606.

Duff, K.E., and Smol, J.P. (1995). The relationship of chrysophycean stomatocysts to environmental variables in fresh-water lakes in British Columbia. *Canadian Journal of Botany-Revue Canadienne De Botanique* 73**,** 1097-1111.

Dunlea, A.G., Murray, R.W., Tada, R., Alvarez-Zarikian, C.A., Anderson, C.H., Gilli, A., Giosan, L., Gorgas, T., Hennekam, R., Irino, T., Murayama, M., Peterson, L.C., Reichart, G.-J., Seki, A., Zheng, H., and Ziegler, M. (2020). Intercomparison of XRF Core Scanning Results From Seven Labs and Approaches to Practical Calibration. *Geochemistry, Geophysics, Geosystems* 21**,** e2020GC009248.

Echeverria, M.E., Sottile, G.D., Mancini, M.V., and Fontana, S.L. (2014). Nothofagus forest dynamics and palaeoenvironmental variations during the mid and late Holocene, in southwest Patagonia. *The Holocene* 24**,** 957-969.

Emile-Geay, J., Cane, M., Seager, R., Kaplan, A., and Almasi, P. (2007). "El Niño as a mediator of the solar influence on climate. Paleoceanography, 22, PA3210".).

Evans, G., Augustinus, P., Gadd, P., Zawadzki, A., Ditchfield, A., and Hopkins, J. (2022). Millennial-scale periodicities associated with changes in wind ansd precipitation over the last Glacial cycle (ca. 117 ± 8.5 ka BP) recorded in sediments from Lake Kai Iwi, Northland, New Zealand. *Global and Planetary Change* 208**,** 103688.

Fiers, G., Bertrand, S., Van Daele, M., Granon, E., Reid, B., Vandoorne, W., and De Batist, M. (2019). Hydroclimate variability of northern Chilean Patagonia during the last 20 kyr inferred from the bulk organic geochemistry of Lago Castor sediments (45°S). *Quaternary Science Reviews* 204**,** 105-118.

Fletcher, M.-S., and Moreno, P.I. (2012). Have the Southern Westerlies changed in a zonally symmetric manner over the last 14,000 years? A hemisphere-wide take on a controversial problem. *Quaternary International* 253**,** 32-46.

Fletcher, M.-S., Pedro, J., Hall, T., Mariani, M., Alexander, J.A., Beck, K., Blaauw, M., Hodgson, D.A., Heijnis, H., Gadd, P.S., and Lise-Pronovost, A. (2021). Northward shift of the southern westerlies during the Antarctic Cold Reversal. *Quaternary Science Reviews* 271**,** 107189.

Fogwill, C.J., and Kubik, P.W. (2016). A glacial stage spanning the antarctic cold reversal in torres del paine (51°s), chile, based on preliminary cosmogenic exposure ages. *Geografiska Annaler: Series A, Physical Geography* 87**,** 403-408.

Force, E.R., and Cannon, W.F. (1988). Depositional model for shallow-marine manganese deposits around black shale basins. *Economic Geology* 83**,** 93-117.

Galili, T. (2021). dendextend: Extending 'dendrogram' Functionality in R. *https://cran.r-project.org/package=dendextend*.

García, J.-L., Hall, B.L., Kaplan, M.R., Vega, R.M., and Strelin, J.A. (2014). Glacial geomorphology of the Torres del Paine region (southern Patagonia): Implications for glaciation, deglaciation and paleolake history. *Geomorphology* 204**,** 599-616.

García, J.-L., Hein, A.S., Binnie, S.A., Gómez, G.A., González, M.A., and Dunai, T.J. (2018). The MIS 3 maximum of the Torres del Paine and Última Esperanza ice lobes in Patagonia and the pacing of southern mountain glaciation. *Quaternary Science Reviews* 185**,** 9-26.

García, J.L., Kaplan, M.R., Hall, B.L., Schaefer, J.M., Vega, R.M., Schwartz, R., and Finkel, R. (2012). Glacier expansion in southern Patagonia throughout the Antarctic cold reversal. *Geology* 40**,** 859-862.

Garreaud, R., Lopez, P., Minvielle, M., and Rojas, M. (2013). Large-Scale Control on the Patagonian Climate. *Journal of Climate* 26**,** 215-230.

Garreaud, R.D., Vuille, M., Compagnucci, R., and Marengo, J. (2009). Present-day South American climate. *Palaeogeography, Palaeoclimatology, Palaeoecology* 281**,** 180-195.

Glasser, N.F., Jansson, K.N., Goodfellow, B.W., De Angelis, H., Rodnight, H., and Rood, D.H. (2017). Cosmogenic nuclide exposure ages for moraines in the Lago San Martin Valley, Argentina. *Quaternary Research* 75**,** 636-646.

Glasser, N.F., Jansson, K.N., Harrison, S., and Kleman, J. (2008). The glacial geomorphology and Pleistocene history of South America between 38°S and 56°S. *Quaternary Science Reviews* 27**,** 365-390.

Grinsted, A., Moore, J.C., and Jevrejeva, S. (2004). Application of the cross wavelet transform and wavelet coherence to geophysical time series. *Nonlinear Processes in Geophysics* 11**,** 561-566.

Guerrero, J.M., and Echenique, R.O. (2002). Cyclostephanos patagonicus sp. nov., a new freshwater diatom from Western Patagonia (Argentina). *Diatom Research* 17**,** 141-151.

Gunn, D.E., and Best, A.I. (1998). A new automated nondestructive system for high resolution multi-sensor core logging of open sediment cores. *Geo-Marine Letters* 18**,** 70-77.

Heiri, O., Lotter, A.F., and Lemcke, G. (2001). Loss on ignition as a method for estimating organic and carbonate content in sediments: reproducibility and comparability of results. *Journal of Paleolimnology* 25**,** 101-110.

Henríquez, C.A., Moreno, P.I., Dunbar, R.B., and Mucciarone, D.A. (2021). The last glacial termination in northwestern Patagonia viewed from the Lago Fonk (~40°S) record. *Quaternary Science Reviews* 271**,** 107197.

Hodgson, D.A., Roberts, S.J., Bentley, M.J., Carmichael, E.L., Smith, J.A., Verleyen, E., Vyverman, W., Geissler, P., Leng, M.J., and Sanderson, D.C.W. (2009). Exploring former subglacial Hodgson Lake, Antarctica. Paper II: palaeolimnology. *Quaternary Science Reviews* 28**,** 2310-2325.

Hodgson, D.A., and Sime, L.C. (2010). Palaeoclimate Southern westerlies and CO2. *Nature Geoscience* 3**,** 666-667.

Hogg, A.G., Heaton, T.J., Hua, Q., Palmer, J.G., Turney, C.S.M., Southon, J., Bayliss, A., Blackwell, P.G., Boswijk, G., Bronk Ramsey, C., Pearson, C., Petchey, F., Reimer, P., Reimer, R., and Wacker, L. (2020). SHCal20 Southern Hemisphere Calibration, 0–55,000 Years cal BP. *Radiocarbon* 62**,** 759-778.

Hogg, A.G., Hua, Q., Blackwell, P.G., Niu, M., Buck, C.E., Guilderson, T.P., Heaton, T.J., Palmer, J.G., Reimer, P.J., Reimer, R.W., Turney, C.S.M., and Zimmerman, S.R.H. (2016). SHCal13 Southern Hemisphere Calibration, 0–50,000 Years cal BP. *Radiocarbon* 55**,** 1889-1903.

Huber, U.M., Markgraf, V., and Schäbitz, F. (2004). Geographical and temporal trends in Late Quaternary fire histories of Fuego-Patagonia, South America. *Quaternary Science Reviews* 23**,** 1079-1097.

Hughes, P.D., and Gibbard, P.L. (2015). A stratigraphical basis for the Last Glacial Maximum (LGM). *Quaternary International* 383**,** 174-185.

Ineson, S., Maycock, A.C., Gray, L.J., Scaife, A.A., Dunstone, N.J., Harder, J.W., Knight, J.R., Lockwood, M., Manners, J.C., and Wood, R.A. (2015). Regional climate impacts of a possible future grand solar minimum. *Nature Communications* 6**,** 7535.

Jouzel, J., Masson-Delmotte, V., Cattani, O., Dreyfus, G., Falourd, S., Hoffmann, G., Minster, B., Nouet, J., Barnola, J.M., Chappellaz, J., Fischer, H., Gallet, J.C., Johnsen, S., Leuenberger, M., Loulergue, L., Luethi, D., Oerter, H., Parrenin, F., Raisbeck, G., Raynaud, D., Schilt, A., Schwander, J., Selmo, E., Souchez, R., Spahni, R., Stauffer, B., Steffensen, J.P., Stenni, B., Stocker, T.F., Tison, J.L., Werner, M., and Wolff, E.W. (2007). Orbital and millennial Antarctic climate variability over the past 800,000 years. *Science* 317**,** 793-796.

Juggins, S. (2007). "C2 Version 1.5 User Guide. Software for ecological and palaeoecological data analysis and visualisation". (Newcastle University).

Juggins, S. (2012). Rioja: Analysis of Quaternary Science Data, R package version (0.8-5).

Kaplan, M.R., Coronato, A., Hulton, N.R.J., Rabassa, J.O., Kubik, P.W., and Freeman, S.P.H.T. (2007). Cosmogenic nuclide measurements in southernmost South America and implications for landscape change. *Geomorphology* 87**,** 284-301.

Kaplan, M.R., Fogwill, C.J., Sugden, D.E., Hulton, N.R.J., Kubik, P.W., and Freeman, S.P.H.T. (2008). Southern Patagonian glacial chronology for the Last Glacial period and implications for Southern Ocean climate. *Quaternary Science Reviews* 27**,** 284-294.

Kaplan, M.R., Strelin, J.A., Schaefer, J.M., Peltier, C., Martini, M.A., Flores, E., Winckler, G., and Schwartz, R. (2020). Holocene glacier behavior around the northern Antarctic Peninsula and possible causes. *Earth and Planetary Science Letters* 534**,** 116077.

Karst-Riddoch, T.L., Malmquist, H.J., and Smol, J.P. (2009). Relationships between freshwater sedimentary diatoms and environmental variables in Subarctic Icelandic lakes. *Fundamental and Applied Limnology* 175**,** 1-28.

Kaufman, D., Mckay, N., Routson, C., Erb, M., Davis, B., Heiri, O., Jaccard, S., Tierney, J., Datwyler, C., Axford, Y., Brussel, T., Cartapanis, O., Chase, B., Dawson, A., De Vernal, A., Engels, S., Jonkers, L., Marsicek, J., Moffa-Sanchez, P., Morrill, C., Orsi, A., Rehfeld, K., Saunders, K., Sommer, P.S., Thomas, E., Tonello, M., Toth, M., Vachula, R., Andreev, A., Bertrand, S., Biskaborn, B., Bringue, M., Brooks, S., Caniupan, M., Chevalier, M., Cwynar, L., Emile-Geay, J., Fegyveresi, J., Feurdean, A., Finsinger, W., Fortin, M.C., Foster, L., Fox, M., Gajewski, K., Grosjean, M., Hausmann, S., Heinrichs, M., Holmes, N., Ilyashuk, B., Ilyashuk, E., Juggins, S., Khider, D., Koinig, K., Langdon, P., Larocque-Tobler, I., Li, J., Lotter, A., Luoto, T., Mackay, A., Magyari, E., Malevich, S., Mark, B., Massaferro, J., Montade, V., Nazarova, L., Novenko, E., Paril, P., Pearson, E., Peros, M., Pienitz, R., Plociennik, M., Porinchu, D., Potito, A., Rees, A., Reinemann, S., Roberts, S., Rolland, N., Salonen, S., Self, A., Seppa, H., Shala, S., St-Jacques, J.M., Stenni, B., Syrykh, L., Tarrats, P., Taylor, K., Van Den Bos, V., Velle, G., Wahl, E., Walker, I., Wilmshurst, J., Zhang, E., and Zhilich, S. (2020). A global database of Holocene paleotemperature records. *Sci Data* 7**,** 115.

Kilham, S.S., and Kilham, P. (1975). Melosira granulata (Ehr.) RALFS: morphology and ecology of a cosmopolitan freshwater diatom. *Verg. Internat. Verein. Limnol.* 19**,** 2716-2721.

Kilian, R., and Lamy, F. (2012). A review of Glacial and Holocene paleoclimate records from southernmost Patagonia (49–55°S). *Quaternary Science Reviews* 53**,** 1-23.

Kirschvink, J.L., and Chang, S.-B.R. (1984). Ultrafine-grained magnetite in deep-sea sediments: Possible bacterial magnetofossils. *Geology* 12**,** 559-562.

Kylander, M.E., Ampel, L., Wohlfarth, B., and Veres, D. (2011). High-resolution X-ray fluorescence core scanning analysis of Les Echets (France) sedimentary sequence: new insights from chemical proxies. *Journal of Quaternary Science* 26**,** 109-117.

Lamy, F., Kilian, R., Arz, H.W., Francois, J.-P., Kaiser, J., Prange, M., and Steinke, T. (2010). Holocene changes in the position and intensity of the southern westerly wind belt. *Nature Geoscience* 3**,** 695-699.

Landschützer, P., Gruber, N., and Bakker, D.C.E. (2016). Decadal variations and trends of the global ocean carbon sink. *Global Biogeochemical Cycles* 30**,** 1396-1417.

Laskar, J., Robutel, P., Joutel, F., Gastineau, M., Correia, A.C.M., and Levrard, B. (2004). A long-term numerical solution for the insolation quantities of the Earth. *A&A* 428**,** 261-285.

Le Quere, C., Rodenbeck, C., Buitenhuis, E.T., Conway, T.J., Langenfelds, R., Gomez, A., Labuschagne, C., Ramonet, M., Nakazawa, T., Metzl, N., Gillett, N., and Heimann, M.

(2007). Saturation of the southern ocean CO2 sink due to recent climate change. *Science* 316**,** 1735-1738.

Löwemark, L., Chen, H.F., Yang, T.N., Kylander, M., Yu, E.F., Hsu, Y.W., Lee, T.Q., Song, S.R., and Jarvis, S. (2011). Normalizing XRF-scanner data: A cautionary note on the interpretation of high-resolution records from organic-rich lakes. *Journal of Asian Earth Sciences* 40**,** 1250-1256.

Mancini, M.a.V. (2002). Vegetation and climate during the Holocene in Southwest Patagonia, Argentina. *Review of Palaeobotany and Palynology* 122**,** 101-115.

Mancini, M.V. (2009). Holocene vegetation and climate changes from a peat pollen record of the forest – steppe ecotone, Southwest of Patagonia (Argentina). *Quaternary Science Reviews* 28**,** 1490-1497.

Mann, M.E., Zhang, Z., Rutherford, S., Bradley, R.S., Hughes, M.K., Shindell, D., Ammann, C., Faluvegi, G., and Ni, F. (2009). Global Signatures and Dynamical Origins of the Little Ice Age and Medieval Climate Anomaly. *Science* 326**,** 1256-1260.

Marcott, S.A., Shakun, J.D., Clark, P.U., and Mix, A.C. (2013). A reconstruction of regional and global temperature for the past 11,300 years. *Science* 339**,** 1198-1201.

Marden, C.J., and Clapperton, C.M. (1995). Fluctuations of the South Patagonian Ice-field during the last glaciation and the Holocene. *Journal of Quaternary Science* 10**,** 197-209.

Markgraf, V., and Huber, U.M. (2010). Late and postglacial vegetation and fire history in Southern Patagonia and Tierra del Fuego. *Palaeogeography, Palaeoclimatology, Palaeoecology* 297**,** 351-366.

Marshall, G.J. (2003). Trends in the Southern Annular Mode from Observations and Reanalyses. *Journal of Climate* 16**,** 4134-4143.

Marshall, G.J. (2007). Half-century seasonal relationships between the Southern Annular mode and Antarctic temperatures. *International Journal of Climatology* 27**,** 373-383.

Marshall, J., and Speer, K. (2012). Closure of the meridional overturning circulation through Southern Ocean upwelling. *Nature Geoscience* 5**,** 171-180.

Mayr, C., Lücke, A., Wagner, S., Wissel, H., Ohlendorf, C., Haberzettl, T., Oehlerich, M., Schäbitz, F., Wille, M., Zhu, J., and Zolitschka, B. (2013). Intensified Southern Hemisphere Westerlies regulated atmospheric CO2 during the last deglaciation. *Geology* 41**,** 831-834.

Mayr, C., Wille, M., Haberzettl, T., Fey, M., Janssen, S., Lucke, A., Ohlendorf, C., Oliva, G., Schabitz, F., and Schleser, G. (2007). Holocene variability of the Southern Hemisphere westerlies in Argentinean Patagonia (52°S). *Quaternary Science Reviews* 26**,** 579-584.

Mcculloch, R.D., Bentley, M.J., Tipping, R.M., and Clapperton, C.M. (2005). Evidence for late-glacial ice dammed lakes in the central Strait of Magellan and Bahia Inutil, southernmost South America. *Geografiska Annaler Series a-Physical Geography* 87A**,** 335-362.

Mcculloch, R.D., Blaikie, J., Jacob, B., Mansilla, C.A., Morello, F., De Pol-Holz, R., San Román, M., Tisdall, E., and Torres, J. (2020). Late glacial and Holocene climate variability, southernmost Patagonia. *Quaternary Science Reviews* 229**,** 106131.

Mcculloch, R.D., and Davies, S.J. (2001). Late-glacial and Holocene palaeoenvironmental change in the central Strait of Magellan, southern Patagonia. *Palaeogeography Palaeoclimatology Palaeoecology* 173**,** 143-173.

Mcculloch, R.D., Mansilla, C.A., Martin, F., Borrero, L., Staff, R.A., and Tisdall, E.W. (2021). The nature and timing of landscape change at Cerro Benítez, Última Esperanza, southern Patagonia (52°S): New insights into the history of megafaunal extinctions and human occupation. *Quaternary International* 601**,** 116-129.

Melles, M., Brigham-Grette, J., Minyuk, P.S., Nowaczyk, N.R., Wennrich, V., Deconto, R.M., Anderson, P.M., Andreev, A.A., Coletti, A., Cook, T.L., Haltia-Hovi, E., Kukkonen, M., Lozhkin, A.V., Rosen, P., Tarasov, P., Vogel, H., and Wagner, B. (2012). 2.8 million years of Arctic climate change from Lake El'gygytgyn, NE Russia. *Science* 337**,** 315-320.

Monnin, E., Indermuhle, A., Dallenbach, A., Fluckiger, J., Stauffer, B., Stocker, T.F., Raynaud, D., and Barnola, J.M. (2001). Atmospheric CO2 concentrations over the last glacial termination. *Science* 291**,** 112-114.

Moore, P.D., Webb, J.A., and Collinson, M.E. (1991). *Pollen Analysis.* Blackwell Scientific Publications.

Moreno, A., Giralt, S., Valero-Garcés, B., Sáez, A., Bao, R., Prego, R., Pueyo, J.J., González-Sampériz, P., and Taberner, C. (2007). A 14kyr record of the tropical Andes: The Lago Chungará sequence (18°S, northern Chilean Altiplano). *Quaternary International* 161**,** 4-21.

Moreno, P.I. (2020). Timing and structure of vegetation, fire, and climate changes on the Pacific slope of northwestern Patagonia since the last glacial termination. *Quaternary Science Reviews* 238**,** 106328.

Moreno, P.I., Francois, J.P., Moy, C.M., and Villa-Martínez, R. (2010). Covariability of the Southern Westerlies and atmospheric CO2 during the Holocene. *Geology* 38**,** 727-730.

Moreno, P.I., François, J.P., Villa-Martínez, R.P., and Moy, C.M. (2009a). Millennial-scale variability in Southern Hemisphere westerly wind activity over the last 5000 years in SW Patagonia. *Quaternary Science Reviews* 28**,** 25-38.

Moreno, P.I., Henríquez, W.I., Pesce, O.H., Henríquez, C.A., Fletcher, M.S., Garreaud, R.D., and Villa-Martínez, R.P. (2021). An early Holocene westerly minimum in the southern mid-latitudes. *Quaternary Science Reviews* 251**,** 106730.

Moreno, P.I., Kaplan, M.R., François, J.P., Villa-Martínez, R., Moy, C.M., Stern, C.R., and Kubik, P.W. (2009b). Renewed glacial activity during the Antarctic cold reversal and persistence of cold conditions until 11.5 ka in southwestern Patagonia. *Geology* 37**,** 375-378.

Moreno, P.I., and Videla, J. (2016). Centennial and millennial-scale hydroclimate changes in northwestern Patagonia since 16,000 yr BP. *Quaternary Science Reviews* 149**,** 326-337.

Moreno, P.I., Vilanova, I., Villa-Martinez, R., Dunbar, R.B., Mucciarone, D.A., Kaplan, M.R., Garreaud, R.D., Rojas, M., Moy, C.M., De Pol-Holz, R., and Lambert, F. (2018). Onset and Evolution of Southern Annular Mode-Like Changes at Centennial Timescale. *Sci Rep* 8**,** 3458.

Moreno, P.I., Vilanova, I., Villa-Martínez, R., Garreaud, R.D., Rojas, M., and De Pol-Holz, R. (2014). Southern Annular Mode-like changes in southwestern Patagonia at centennial timescales over the last three millennia. *Nature Communications* 5**,** 4375.

Moreno, P.I., Villa-Martínez, R., Cárdenas, M.L., and Sagredo, E.A. (2012). Deglacial changes of the southern margin of the southern westerly winds revealed by terrestrial records from SW Patagonia (52°S). *Quaternary Science Reviews* 41**,** 1-21.

Mulvaney, R., Abram, N.J., Hindmarsh, R.C., Arrowsmith, C., Fleet, L., Triest, J., Sime, L.C., Alemany, O., and Foord, S. (2012). Recent Antarctic Peninsula warming relative to Holocene climate and ice-shelf history. *Nature* 489**,** 141-144.

Neukom, R., Gergis, J., Karoly, D.J., Wanner, H., Curran, M., Elbert, J., Gonzalez-Rouco, F., Linsley, B.K., Moy, A.D., Mundo, I., Raible, C.C., Steig, E.J., Van Ommen, T., Vance, T., Villalba, R., Zinke, J., and Frank, D. (2014). Inter-hemispheric temperature variability over the past millennium. *Nature Clim. Change* 4**,** 362-367.

Oksanen, J. (2014). "Vegan: Community Ecology Package. R package version 2.3-0.". (http://cran.r-project.org/web/packages/vegan/index.html).

Paillard, D., Labeyrie, L., and Yiou, P. (1996). Macintosh program performs time-series analysis. *Eos Transactions. AGU* 77**,** 379.

Palacios, D., Stokes, C.R., Phillips, F.M., Clague, J.J., Alcalá-Reygosa, J., Andrés, N., Angel, I., Blard, P.-H., Briner, J.P., Hall, B.L., Dahms, D., Hein, A.S., Jomelli, V., Mark, B.G., Martini, M.A., Moreno, P., Riedel, J., Sagredo, E., Stansell, N.D., Vázquez-Selem, L., Vuille, M., and Ward, D.J. (2020). The deglaciation of the Americas during the Last Glacial Termination. *Earth-Science Reviews* 203**,** 103113.

Peck, V.L., Allen, C.S., Kender, S., Mcclymont, E.L., and Hodgson, D.A. (2015). Oceanographic variability on the West Antarctic Peninsula during the Holocene and the influence of upper circumpolar deep water. *Quaternary Science Reviews* 119**,** 54-65.

Perren, B.B., Hodgson, D.A., Roberts, S.J., Sime, L., Van Nieuwenhuyze, W., Verleyen, E., and Vyverman, W. (2020). Southward migration of the Southern Hemisphere westerly winds corresponds with warming climate over centennial timescales. *Communications Earth & Environment* 1**,** 58.

Pesce, O., and Moreno, P. (2014). Vegetation, fire and climate change in central-east Isla Grande de Chiloé (43 S) since the Last Glacial Maximum, northwestern Patagonia. *Quaternary Science Reviews* 90**,** 143-157.

Pirlet, H., Wehrmann, L.M., Brunner, B., Frank, N., Dewanckele, J., Van Rooij, D., Foubert, A., Swennen, R., Naudts, L., Boone, M., Cnudde, V., and Henriet, J.-P. (2010). Diagenetic formation of gypsum and dolomite in a cold-water coral mound in the Porcupine Seabight, off Ireland. *Sedimentology* 57**,** 786-805.

Quade, J., and Kaplan, M.R. (2017). Lake-level stratigraphy and geochronology revisited at Lago (Lake) Cardiel, Argentina, and changes in the Southern Hemispheric Westerlies over the last 25 ka. *Quaternary Science Reviews* 177**,** 173-188.

Renberg, I. (1990). A procedure for preparing large sets of diatom slide from sediment cores. *Journal of Paleolimnology* 4**,** 87-90.

Reynhout, S.A., Sagredo, E.A., Kaplan, M.R., Aravena, J.C., Martini, M.A., Moreno, P.I., Rojas, M., Schwartz, R., and Schaefer, J.M. (2019). Holocene glacier fluctuations in Patagonia are modulated by summer insolation intensity and paced by Southern Annular Mode-like variability. *Quaternary Science Reviews* 220**,** 178-187.

Rioual, P., Andrieu-Ponel, V., De Beaulieu, J.-L., Reille, M., Svobodova, H., and Battarbee, R.W. (2007). Diatom responses to limnological and climatic changes at Ribains Maar (French Massif Central) during the Eemian and Early Würm. *Quaternary Science Reviews* 26**,** 1557-1609.

Roberts, S.J., Monien, P., Foster, L.C., Loftfield, J., Hocking, E.P., Schnetger, B., Pearson, E.J., Juggins, S., Fretwell, P., Ireland, L., Ochyra, R., Haworth, A.R., Allen, C.S., Moreton, S.G., Davies, S.J., Brumsack, H.J., Bentley, M.J., and Hodgson, D.A. (2017). Past penguin colony responses to explosive volcanism on the Antarctic Peninsula. *Nat Commun* 8**,** 14914.

Rühland, K., Paterson, A.M., and Smol, J.P. (2008). Hemispheric-scale patterns of climate-related shifts in planktonic diatoms from North American and European lakes. *Global Change Biology* 14**,** 2740-2754.

Rühland, K.M., Smol, J.P., and Pienitz, R. (2003). Ecology and spatial distributions of surface-sediment diatoms from 77 lakes in the subarctic Canadian treeline region. *Canadian Journal of Botany* 81**,** 57-73.

Rumrich, U., Lange-Bertalot, H., and Rumrich, M. (2000). *Diatoms of the Andes.* Königstein, Germany,: Koeltz Scientific Books.

Sagredo, E.A., Moreno, P.I., Villa-Martínez, R., Kaplan, M.R., Kubik, P.W., and Stern, C.R. (2011). Fluctuations of the Última Esperanza ice lobe (52°S), Chilean Patagonia, during the last glacial maximum and termination 1. *Geomorphology* 125**,** 92-108.

Saunders, K.M., Roberts, S.J., Perren, B., Butz, C., Sime, L., Davies, S., Van Nieuwenhuyze, W., Grosjean, M., and Hodgson, D.A. (2018). Holocene dynamics of the Southern Hemisphere westerly winds and possible links to CO2 outgassing. *Nature Geoscience* 11**,** 650-655.

Schittek, K., Forbriger, M., Mächtle, B., Schäbitz, F., Wennrich, V., Reindel, M., and Eitel, B. (2015). Holocene environmental changes in the highlands of the southern Peruvian Andes (14° S) and their impact on pre-Columbian cultures. *Climate of the Past* 11**,** 27-44.

Schneider, C., Glaser, M., Kilian, R., Santana, A., Butorovic, N., and Casassa, G. (2013). Weather Observations Across the Southern Andes at 53°S. *Physical Geography* 24**,** 97-119.

Shin, J., Ahn, J., Chowdhry Beeman, J., Lee, H.G., and Brook, E.J. (2021). Millennial variations of atmospheric CO2 during the early Holocene (11.7–7.4 ka). *Clim. Past Discuss.* 2021**,** 1-22.

Simms, A.R., Bentley, M.J., Simkins, L.M., Zurbuchen, J., Reynolds, L.C., Dewitt, R., and Thomas, E.R. (2021). Evidence for a “Little Ice Age” glacial advance within the Antarctic Peninsula – Examples from glacially-overrun raised beaches. *Quaternary Science Reviews* 271**,** 107195.

Smol, J.P. (1983). Paleophycology of a high arctic lake near Cape Herschel, Ellesmere Island. *Canadian Journal of Botany* 61**,** 2195-2204.

Solari, M.A., Le Roux, J.P., Herve, F., Airo, A., and Calderon, M. (2012). Evolution of the Great Tehuelche Paleolake in the Torres del Paine National Park of Chilean Patagonia during the Last Glacial Maximum and Holocene. *Andean Geology* 39**,** 1-21.

Spratt, R.M., and Lisiecki, L.E. (2016). A Late Pleistocene sea level stack. *Climate of the Past* 12**,** 1079-1092.

Steinhilber, F., Beer, J., and Fröhlich, C. (2009). Total solar irradiance during the Holocene. *Geophysical Research Letters* 36.

Sterken, M., Roberts, S., Hodgson, D., Vyverman, W., Balbo, A.L., Sabbe, K., Moreton, S.G., and Verleyen, E. (2012). Holocene glacial and climate history of Prince Gustav Channel, northeastern Antarctic Peninsula. *Quaternary Science Reviews* 31**,** 93-111.

Stevenson, R.J., Hill, B.H., Herlihy, A.T., Yuan, L.L., and Norton, S.B. (2008). Algae–P relationships, thresholds, and frequency distributions guide nutrient criterion development. *Journal of the North American Benthological Society* 27**,** 783-799.

Stockmarr, J. (1971). Tablets with Spores Used in Absolute Pollen Analysis. *Pollen et Spores* 13**,** 615-621.

Street-Perrott, F.A., Barker, P.A., Swain, D.L., Ficken, K.J., Wooller, M.J., Olago, D.O., and Huang, Y. (2007). Late Quaternary changes in ecosystems and carbon cycling on Mt. Kenya, East Africa: a landscape-ecological perspective based on multi-proxy lake-sediment influxes. *Quaternary Science Reviews* 26**,** 1838-1860.

Tjallingii, R., Röhl, U., Kölling, M., and Bickert, T. (2007). Influence of the water content on X-ray fluorescence core-scanning measurements in soft marine sediments. *Geochemistry, Geophysics, Geosystems* 8.

Toggweiler, J.R., and Russell, J. (2008). Ocean circulation in a warming climate. *Nature* 451**,** 286-288.

Toggweiler, J.R., Russell, J.L., and Carson, S.R. (2006). Midlatitude westerlies, atmospheric CO2, and climate change during the ice ages. *Paleoceanography* 21**,** n/a-n/a.

Tolotti, M., Corradini, F., Boscaini, A., and Calliari, D. (2007). Weather-driven ecology of planktonic diatoms in Lake Tovel (Trentino, Italy). *Hydrobiologia* 578**,** 147-156.

Torres, M.E., Hong, W.-L., Solomon, E.A., Milliken, K., Kim, J.-H., Sample, J.C., Teichert, B.M.A., and Wallmann, K. (2020). Silicate weathering in anoxic marine sediment as a requirement for authigenic carbonate burial. *Earth-Science Reviews* 200**,** 102960.

Trauth, M.H. (2015). "Time-Series Analysis," in *MATLAB® Recipes for Earth Sciences,* ed. M. H. Trauth. (Berlin, Heidelberg: Springer Berlin Heidelberg), 151-213.

Tuhkanen, S. (1992). The climate of Tierra del Fuego from a vegetation geographical point of view and its ecoclimatic counterparts elsewhere. . *Acta Botanica Fennica* 145**,** 1-64.

Turney, C.S.M., Jones, R.T., Fogwill, C., Hatton, J., Williams, A.N., Hogg, A., Thomas, Z.A., Palmer, J., Mooney, S., and Reimer, R.W. (2016). A 250-year periodicity in Southern Hemisphere westerly winds over the last 2600 years. *Climate of the Past* 12**,** 189-200.

Van Daele, M., Bertrand, S., Meyer, I., Moernaut, J., Vandoorne, W., Siani, G., Tanghe, N., Ghazoui, Z., Pino, M., Urrutia, R., and De Batist, M. (2016). Late Quaternary evolution of Lago Castor (Chile, 45.6°S): Timing of the deglaciation in northern Patagonia and evolution of the southern westerlies during the last 17 kyr. *Quaternary Science Reviews* 133**,** 130-146.

Van Dam, H., Mertens, E., and Sinkeldam, J. (1994). A coded checklist and ecological indicator values of freshwater diatoms from The Netherlands. *Netherland Journal of Aquatic Ecology* 28**,** 117-133.

Viaggi, P. (2021). Quantitative impact of astronomical and sun-related cycles on the Pleistocene climate system from Antarctica records. *Quaternary Science Advances* 4**,** 100037.

Villa-Martínez, R., and Moreno, P.I. (2017). Pollen evidence for variations in the southern margin of the westerly winds in SW patagonia over the last 12,600 years. *Quaternary Research* 68**,** 400-409.

Weltje, G.J., and Tjallingii, R. (2008). Calibration of XRF core scanners for quantitative geochemical logging of sediment cores: Theory and application. *Earth and Planetary Science Letters* 274**,** 423-438.

Wennrich, V., Minyuk, P.S., Borkhodoev, V., Francke, A., Ritter, B., Nowaczyk, N.R., Sauerbrey, M.A., Brigham-Grette, J., and Melles, M. (2014). Pliocene to Pleistocene climate and environmental history of Lake El'gygytgyn, Far East Russian Arctic, based on high-resolution inorganic geochemistry data. *Climate of the Past* 10**,** 1381-1399.

Whitlock, C., Moreno, P.I., and Bartlein, P. (2017). Climatic controls of Holocene fire patterns in southern South America. *Quaternary Research* 68**,** 28-36.

Wille, M., and Schäbitz, F. (2008). Late-glacial and Holocene climate dynamics at the steppe/forest ecotone in southernmost Patagonia, Argentina: the pollen record from a fen near Brazo Sur, Lago Argentino. *Vegetation History and Archaeobotany* 18**,** 225-234.

Wilson, C.R., Michelutti, N., Cooke, C.A., Briner, J.P., Wolfe, A.P., and Smol, J.P. (2012). Arctic lake ontogeny across multiple interglaciations. *Quaternary Science Reviews* 31**,** 112-126.

Winder, M., Reuter, J.E., and Schladow, S.G. (2009). Lake warming favours small-sized planktonic diatom species. *Proc Biol Sci* 276**,** 427-435.

Wittkop, C., Swanner, E.D., Grengs, A., Lambrecht, N., Fakhraee, M., Myrbo, A., Bray, A.W., Poulton, S.W., and Katsev, S. (2020). Evaluating a primary carbonate pathway for manganese enrichments in reducing environments. *Earth and Planetary Science Letters* 538**,** 116201.

Yuan, X., and Yonekura, E. (2011). Decadal variability in the Southern Hemisphere. *Journal of Geophysical Research: Atmospheres* 116.

Zolitschka, B., Anselmetti, F., Ariztegui, D., Corbella, H., Francus, P., Lücke, A., Maidana, N.I., Ohlendorf, C., Schäbitz, F., and Wastegård, S. (2013). Environment and climate of the last 51,000 years – new insights from the Potrok Aike maar lake Sediment Archive Drilling prOject (PASADO). *Quaternary Science Reviews* 71**,** 1-12.

Zolitschka, B., Fey, M., Janssen, S., Maidana, N.I., Mayr, C., Wulf, S., Haberzettl, T., Corbella, H., Lücke, A., Ohlendorf, C., and Schäbitz, F. (2018). Southern Hemispheric Westerlies control sedimentary processes of Laguna Azul (south-eastern Patagonia, Argentina). *The Holocene* 29**,** 403-420.

Late Glacial and Holocene Palaeolake History of the Última Esperanza Region of Southern Patagonia

Supplementary Materials and Data

Stephen J. Roberts[1], Robert D. McCulloch[2], Joseph F. Emmings[3], Sarah J. Davies[4], Wim Van Nieuwenhuyze[5], Mieke Sterken[5], Katrien Heirman[6], Jeroen Van Wichelen[5,7], Carolina Diaz[8], Evelien Van de Vyver[5,9], Alex Whittle[1], Wim Vyverman[5], Dominic A. Hodgson[1], Elie Verleyen[5]

[1]British Antarctic Survey, Natural Environment Research Council, Cambridge, United Kingdom; [2]Centro de Investigación en Ecosistemas de la Patagonia (CIEP), Coyhaique, Chile; [3]British Geological Survey, Nottingham, United Kingdom; [4]Department of Geography and Earth Sciences, Aberystwyth University, Aberystwyth, United Kingdom; [5]Protistology and Aquatic Ecology, Ghent University, Gent, Belgium; [6]TNO—Geological Survey of the Netherlands, Utrecht, Netherlands; [7]Research Institute for Nature and Forest, Herman Teirlinckgebouw, Brussels, Belgium; [8]Institute of Ecology and Biodiversity (IEB), Universidad de Chile, Santiago, Chile; [9]Flanders Environment Agency, Aalst, Belgium.

1. Supplementary Methods

Chronological Methods: Twenty-four samples were taken from the Lago Pato LP08 record and fifteen samples from the LP16 record for Accelerator Mass Spectrometry (AMS) radiocarbon dating. For the LP08 record, these included five highly organic macrophyte-dominated lake-mud samples, which were wet-sieved (250 μm) to remove fine minerogenic sand, silt, and clay particles; six organic-rich bulk lake-mud samples; three hand-picked plant macrofossils; seven fine glaciogenic bulk sediment samples. The LP16 samples consisted of four hand-picked plant macrofossils, five organic peat/lake mud bulk samples and five glaciogenic bulk sediment samples (Table 3).

Radiocarbon dating samples analysed by SUERC were 'acid-washed': digested in 2 M HCl (80ºC for 8 hours), washed free from mineral acid with distilled water until all traces of acid and carbonate had been removed, and dried in a vacuum oven. The total carbon in a known weight of all pre-treated samples was recovered as CO_2 by heating with CuO in a sealed quartz tube. The CO_2 was converted to graphite by Fe/Zn reduction. Samples dated by Beta Analytic were 'acid-washed': leached with a 0.5M to 1.0M HCl bath to remove carbonates, heated to 70ºC for 4 hours. Leaching was repeated until no carbonate remained, followed by rinsing to neutral 20 times with deionised water. Plant material samples were 'acid/alkali/acid' pretreated using the above procedure then placed in 0.5% to 2% solution of NaOH for 4 hrs at 70ºC and rinsed to neutral 20 times with deionised water. The process was repeated until no additional reaction (typically indicated by a colour change in the NaOH liquid) was observed. Samples were then leached again in a 0.5M to 1.0M HCl bath to remove any CO_2 absorbed from the atmosphere by the NaOH soakings and to ensure initial carbonate removal was complete. All samples were dried at 70ºC in a gravity oven for 8-12 hours.

Calibration of measured radiocarbon ages was undertaken in OXCAL v.4.2 (Ramsey, 2009) using the SHCal20.14C Southern Hemisphere atmosphere dataset (Hogg et al., 2020). Post-bomb samples were calibrated using the SHCal13 SH Zone 1-2 Bomb curve in CALIBomb (Hua et al., 2013). Radiocarbon age data are reported as conventional radiocarbon years BP (^{14}C yr. BP) ± 1σ and as 2σ (95.4%) calibrated age ranges, median and mean cal yr BP (relative to 1950 CE) (Table 3), rounded to the nearest ten years as measured age errors are less than ± 50 ^{14}C years. Age-depth models were generated using Bayesian age-depth modelling software BACON v.2.5 (Blaauw and Christen, 2011)

using R v. 3.5. Weighted mean interpolated ages, derived from the 'best-fit' age depth model, and 95% confidence interval calibrated age ranges were rounded to the nearest 100 years in the text to reflect dating errors and modelling uncertainties. Holocene sediment accumulation rates in LP08 were relatively uniform apart from a notable decrease in the less-compacted uppermost 40 cm. The minimum-maximum range and mean ± 2σ sedimentation rate from 470 cm upwards is 0.011–0.085 cm yr^{-1} and 0.055 ± 0.04 cm yr^{-1} meaning that a 1 cm sampling interval represents, on average, 18 years and a 2 mm interval represents 4 years. Accumulation rates are highest during the mid-late Holocene (0.05–0.08 cm yr-1 and lowest during the early Holocene (340–470 cm; 10,000-6,100 cal a BP: 0.025-0.05 cm yr^{-1}) and during the last c. 1,500 years (upper 40 cm: 0.025–0.03 cm yr^{-1}).

Core Scanning Methods: Cores were split and analysed using a GEOTEK multi-sensor core logger following standard procedures to obtain gamma-ray density, resistivity and magnetic susceptibility (MS) data (Gunn and Best, 1998) (Bartington Instruments; LP08: MS2C loop sensor, 2 mm intervals, 10 seconds; LP16: MS2E point sensor, 0.5 mm intervals; 10 seconds). XRF core scanning (XRF-CS) analysis was undertaken to characterise bulk wet geochemical variations. Digital X-radiographs were obtained from split cores using a rotating anode mobile digital Celtic SMR CR computerised X radiography unit, based at Cambridge University Vet School (48kV; 4 mAs; no grid; exposure per plate digitally processed and converted to JPEG files) and, prior to XRF-CS analysis, from an ITRAX^{TM} digital X-radiograph (45 kV, 50 mA.ms, 200 ms, 60 µm interval) at the University Aberystwyth. Contiguous downcore wet-sediment Energy Dispersive Spectrometry (EDS) XRF-CS geochemistry was obtained using an ITRAX^{TM} XRF scanner fitted with a Molybdenum (Mo) anode X-ray tube (settings: 30 kV, 50 mA, count time 10 seconds, at 2 mm (Unit 6 LP08), 200 µm (Unit 1 LP08) 100 µm intervals (basal Unit 1; core LP08-1I), and LP16 (0.5 mm (Units 2-6) and 200 µm Unit 1) intervals). A synthetic glass standard and XRF fused glass discs from Antarctic lake sediment core subsamples were used to ensure the XRF-CS scanner was functioning correctly.

XRF-CS spectra were analysed using Q-spec v8.6.0, to generate count per second ED (Energy Dispersive) datasets with MSE values minimised to optimise measured-modelled spectra fit and generate robust counts-per-second (cps) data. To account for downcore variations in water content and density, and to examine covariance, closed-sum effects, and non-stationarity of some geochemical responses through time, data were normalised by total scatter cps (incoherent (Compton) scatter + coherent (Rayleigh) scatter). Results are expressed as $\log_{10}$ and/or natural log element/total scatter ratios, and as a percentage of the total scatter normalised ratio ($\sum$ TSN; see below) (Kylander et al., 2011; Davies et al., 2015; Roberts et al., 2017; Saunders et al., 2018). As Al counts were too low (Löwemark et al., 2011) and Rb counts in organic-rich deposits were often zero (Wilhelms-Dick et al., 2012), Ti-normalised (natural) log-ratios were used to estimate of the background bedrock composition. Constrained CONISS clustering of XRF-CS geochemical data was used to delineate lithofacies zones. Principal Components Analysis (PCA) was used to establish correlation relationships between different elements and determine which element ratios could be used to constrain lake orogeny, sediment provenance, and bottom water redox conditions. Data from finely laminated glaciolacustrine sediments in Units 1and 2 were smoothed to 200 µm and equal spaced time-intervals (10-years and 100-years) used for time series analysis were centered, standardised (Z-scores) and detrended (polynomial linear best fit) and interpolated using a 10-year Piecewise Cubic Hermite Interpolating Polynomial (PCHIP) interpolation applied to avoid spline artefacts and preserve the shape of the original XRF-CS data series. Second order polynomial Locally Weighted Scatterplot Smoothing (LOESS) 100-year smoothing (0.1 sampling interval with outliers removed) was also used to compare datasets to published data.

Detection limits are <c. 1% for all elements described. For direct comparison with 1 cm interval subsample data, five-point and 50-point cps data sum and ratio/percentage running means were used to convert 2 mm and 200 µm as-measured interval datasets to 1 cm in intervals. The 1 cm dataset is equivalent to 50 and 500 second scans per cm, respectively, and allowed the more reliable acquisition of useful light elements with low count rates, e.g., Si, P and S. Improved counting statistics for these lighter elements can also be obtained using Cr-tube analysis (Saunders et al., 2018) (not undertaken

on the Lago Pato cores). Elemental and scatter counts were calculated form measurable element peak area count per second data (cps). After filtering out low-count areas and spurious data due to uneven sediment surface or gaps in the core with lower-than-average count statistics (<2-sigma standard deviation kcps), CONISS (constrained) cluster analysis was applied to 1 cm mean datasets to identify geochemically distinct zones.

XRF-CS Total Scatter Normalisation: XRF core scanning has many advantages, but it is an Energy Dispersive Spectrometry (ED) method and, therefore, produces semi-quantitative, non-concentration data. Without normalisation, trends in wet sediment XRF-CS scan data can be different to those obtained by standard (whole-rock composition) XRF analysis in which water and carbon are removed beforehand. Potential differences between Wavelength Dispersive Spectrometry (WD)-XRF and EDS XRF-CS techniques can be undertaken by examining data from representative lithologies using WD-XRF and ICP-MS subsample analysis methods. Several examples good coherence between ED XRF-XRF and WD-XRF methods can be found in (Rothwell and Croudace, 2015). Since we are primarily interested in the downcore trends in wet sediment and the differences between organic-rich and minerogenic sediments, scan data have not been calibrated using subsample data in this study (Davies et al. 2015). XRF-CS data were compared with downcore patterns of standard palaeolimnological parameters (e.g., LOI, TOC, MS). Further comparison of the patterns obtained from ED and WD techniques is outside the scope of the present study and was largely ineffectual in highly organic Holocene-age deposits in the LP08 and LP16 records.

Without normalisation, spurious elemental patterns and matrix effects can occur in wet sediment scanning, especially when dealing with a high and/or highly variable highly organic sediment content (Croudace et al., 2006; Wilhelms-Dick et al., 2012; Davies et al., 2015). To account for these effects, closed-sum effects and downcore variations in organic and water content, and to allow comparisons between cores run at different times and different tube life, cps data were normalised by total scatter counts (incoherent+coherent) (Kylander et al., 2011; Löwemark et al., 2011; Davies et al., 2015) and element/Ti log ratios to account for closed-sum effects associated with compositional data.

To determine the relative proportions of individual elements and scatter parameters measured and examine covariance patterns, we examined scatter ratios (element/in.) and expressed element/inc.+coh. values (following Kylander et al., (2011)) as a percentage of the total scatter normalised element and scatter cps ratio sum ($\sum$TSN). Total scatter ($\sigma_{inc+coh}$) (cps) is defined as Compton+Rayleigh scattering and referred to as incoherent (σ_{inc}) (Compton or inelastic) +coherent (σ_{coh}) (Rayleigh or elastic) scattering. In effect, this method accounts for the influence of scatter, by converting it to a constant equal to one.

Elemental and scatter data in this study are presented as percentages of the Total Scatter Normalised ratio sum (%$\sum$TSN or, simply, %TSN), which produces the same percentage values for elements and scatter expressed as a percentage of the cps sum (%cps). Scatter normalisation %TSN and %cps methods provide a simple and effective way to account for the influence of variable scatter from wet (and organic-rich) sediment and can produce different downcore profiles to cps plots and. These percentages are tube-specific and represent the proportion of elements measured by ITRAX^{TM} ED XRF-CS analysis and are not equivalent to whole rock compositions obtained by traditional XRF analytical techniques.

Correlations between key elements and parameters of interest were determined using Pearson Correlation Coefficients (PCC) (Table S1) and by Principal Components Analysis (PCA). Covariant element and scatter parameters are colour-coded in Figures S2 and S3 according to their PCA axis 1 derived relationship to minerogenic (blue) or organic-driven (green) trends. Covariance and PCC statistics were used to determine which of the recognised 'stable' elements can be considered resilient to weathering processes (e.g., Al, Ti, Rb; Davies et al. (2015)) had sufficient counts for normalization. Al and Rb cps were considered too low for reliable normalization, particularly in organic-rich sections of the record.

In calibration tests, trends in reliably measurable downcore elements (e.g., Ti) have been well correlated to traditional XRF subsampling methods (e.g., Roberts et al., 2017). We also compared %TSN element and scatter with those obtained using the Boyle et al. (2015) dry mass 'concentration' normalization method where elemental and scatter cps data are normalized by the $\sigma_{coh}/\sigma_{inc}$ ratio to produce dry mass equivalent datasets. These important initial data processing steps were particularly important for elements such as Mn, Fe, Ca in this study that have multiple possible sources (Kylander et al., 2011; Melles et al., 2012).

Cryptotephra analysis: Glass shard geochemistry was analysed using the Cameca SX-100 electron probe microanalyser (EPMA) at the Tephra Analytical Unit, University of Edinburgh by Chris Hayward with a beam diameter of 8 µm following procedures in Hayward (2012) and run conditions: 15 keV/2 nA (Al, Ka, Si Ka, K Ka, Ca Ka, Na Ka, Mg Ka, K Ka, Ca Ka, Fe Ka); 15 keV/80 nA (P Ka, Ti Ka, Mn Ka, P Ka, Ti Ka). Andradite standards were run at the start and end of each session. Analytical conditions and results for shards with >95% totals are shown in Table S2. New shard geochemical data was compared to a database of distal tephra major element glass shard analyses from Southern South America n = 1,031 (McCulloch and Davies, 2001; McCulloch et al., 2005; Sagredo et al., 2011; Stern et al., 2015; Mansilla et al., 2016; McCulloch et al., 2017; Mansilla et al., 2018; McCulloch et al., 2019; Smith et al., 2019; Blaikie, 2020; McCulloch et al., 2020; McCulloch et al., 2021) using Principal Components Analysis (PCA) and k-means hierarchical cluster analysis (Wards method, Euclidean distance between samples).

Diatom analysis: Several different sources were used for diatom taxonomy (Rumrich et al., 2000; Guerrero and Echenique, 2002). For some diatom identifications, scanning-electron microscopy was used in addition to light microscopy. Some species were grouped or could only be identified to genus level because of difficulties in distinguishing morphotypes/species under light microscopy, for example *Fragilariod* species.

Statistical analysis: Hierarchical cluster analysis (k-means; Ward's) and data plotting was undertaken in RStudio v. 0.98.939 using R v. 3.5 and packages Vegan v. 2.3-0 (Oksanen, 2014) and Rioja v. 0.8-5 (Juggins, 2012), XLStat v. 2010.3.09, C2 v. 1.7.6 (Juggins, 2007), C2 v. 1.7.7, and Sigmaplot v.14. Principal Components Analysis (PCA) was undertaken in C2 and R using packages ggplot2, factoextra, dendextend, cowplot, Ggally and ITRAX.r (Bishop, 2021)) with standardised (mean-1σ) and centered natural log-transformed percentage diatom, pollen and %TSN XRF-CS data. CONISS stratigraphically constrained cluster analysis with Hellinger's distances was undertaken in R packages Rioja and Tilia (Grimm, 1987) on standardised (mean-1σ) percentage data with broken stick analysis to determine the stratigraphic position of significant geochemical, diatom and pollen units/zones. Time series (interpolation, standardization (Z-scores), detrending, autocorrelation, peak identification, changepoint and wavelet analysis) were all undertaken in MATLAB using standard Signal Processing Tools and modules.

All data has been deposited in the NERC EDS UK Polar Data Centre (PDC) as follows:

Roberts, S., Sterken, M., Heirman, K., Van Wichelen, J., Diaz, C., Vyverman, W., & Verleyen, E. (2022). Bathymetric and lake chemistry data for Lago Pato,Torres del Paine National Park, Chile (Version 1.0) [Data set]. NERC EDS UK Polar Data Centre. https://doi.org/10.5285/D55D7619-3E07-41B0-929E-C9DA0A4B61AF Short DOI: https://doi.org/hjnx

Roberts, S., McCulloch, R., Davies, S., Emmings, J., Sterken, M., Van de Vyver, E., Van Nieuwenhuyze, W., Heirman, K., Van Wichelen, J., & Diaz, C. (2022). Biological, chronological, geochemical, and physical sedimentological data for the LP08 lake sediment record extracted from Lago Pato, Torres del Paine, Chile in 2007-2008 (Version 1.0) [Data set]. NERC EDS UK Polar Data Centre. https://doi.org/10.5285/C75EA98B-080E-455E-A54F-A9E8CF07AA73 Short DOI: https://doi.org/hjnz

Roberts, S., McCulloch, R., Emmings, J., Davies, S., Vyverman, W., Verleyen, E., & Hayward, C. (2022). Biological, chronological, geochemical, and physical sedimentological data for the LP16 lake sediment record extracted from Lago Pato, Torres del Paine, Southern Chile in 2015 (Version 1.0) [Data set]. NERC EDS UK Polar Data Centre. https://doi.org/10.5285/F85EE4EB-8918-4AA4-8E51-6C46F4C812CB Short DOI: https://doi.org/hjn2

Roberts, S., McCulloch, R., Emmings, J., & Davies, S. (2022). Geochemical X ray fluorescence log ratio time series data for two sediment cores, LP08 and LP16, extracted from Lago Pato, Torres del Paine, Southern Chile (Version 1.0) [Data set]. NERC EDS UK Polar Data Centre. https://doi.org/10.5285/6BD95602-F2E3-4968-8622-C4AEB71C214C Short DOI: https://doi.org/hjn3

Code and data can be found at: https://github.com/stever60/Lago_Pato.

2. Supplementary Results

Chronological Results: Four radiocarbon ages from organic deposits in LP08 and LP16 were outliers due to the emplaced during coring and excluded prior to age-depth modelling (Table 3). In LP08, flocculent organic deposits recovered from >600 cm depth with radiocarbon ages of <9,000 cal yr BP were emplaced by upwards suction on extraction of the core from Unit 1 deposits and not considered part of the sequence stratigraphy. Translocated root material in Unit 2 of LP16with a significant age reversal was rejected as an outlier and excluded from the LP16 age-depth model.

As-measured results from both records imply that a deep palaeolake existed at Lago Pato between the gLGM and local glacier maximum extent, and that sediments between c. 21,000–10,000 cal a BP are missing from the LP08 record. In contrast, no obvious evidence of a hiatus due erosion by glacier overriding or rapid lake emptying exists between Units 1 and 2 in the LP16 stratigraphic record.

For Units 1 and 2 in LP16 to be continuous, bulk radiocarbon ages would require a lake reservoir correction of c. 6,600 ± 500 ^{14}C years. Problems with 'old' carbon glacially derived sediments in the TdP region are well-documented (McCulloch and Davies, 2001; Solari et al., 2012; Davies et al., 2020) and bulk dates are widely considered to represent maximum, rather than depositional ages of palaeolake formation (Grimm et al., 2009; García et al., 2014). Several processes are known to create offsets of as much as 10,000 years in glaciolacustrine sediments: 1) carbonate or 'hard water effect'; 'old' carbon by glacial erosion; radiocarbon-depleted glacial meltwater; 2) reduced gaseous exchange at the sediment water interface in deep and poorly ventilated lakes; 3) perennial ice cover; disturbance of the sediments by ice or ice-rafting (Hodgson et al., 2009).

A large reservoir-correction for Unit 1 sediments is supported by an offset of c. 3,640 years between two closely spaced bulk sediment samples at 554–555 cm and 556–557 cm in LP08 (Calibrated ages of 22,740 ± 120 cal yr BP and 26,380 ± 190 cal yr BP; Table 3). Conversely, mean %TSN values for Ca in LP08 and LP16 Unit 1 deposits are <2% and maximum values in Unit 6A are significantly lower (Ca<15%TSN) than marl deposits in other lake records from Patagonia (Ca>70%TSN; McCulloch, unpublished data), suggesting 'hard water' corrections for bulk radiocarbon ages may not be necessary. All other carbonate proxies (LOI_{950}, resistivity, Ca/Ti, Sr/Ti) remained low in Unit 1 in LP08 and LP16 and in Unit 2 in LP16 compared to Units 3–6A/B in both records. Carbon isotope data of Unit 1 sediments from both records were only marginally enriched (mean ± 1σ: n = 16, $\%C_{org}$ = 0.69 ± 0.54, C/N = 8.00 ± 1.10, $\delta^{13}C$ = -26.28 ± 1.56 ‰ and $\delta^{13}C$ dated: n = 11; -25.2 ± 0.3 ‰) compared to the glacial sediments of Unit 2 ($\delta^{13}C$ from radiocarbon dated samples n = 2; -29.3+3.0 ‰) and Holocene-age organic deposits and macrofossils (mean ± 1σ: n = 101, $\%C_{org}$ = 21.66 ± 8.60, C/N = 11.34 ± 0.90, δ13C = -30.15 ± 1.13 ‰ and δ13C dated: n = 19; -28.9 ± 1.3 ‰). N/C ratios corrections are not generally applicable to 'carbonate-rich' lakes in Chilean Patagonia environments

influenced by hard water effects (Bertrand et al., 2012) yet Holocene-age offsets during exceptionally arid phases between 10-7.5 ka are minimal, with a mean N/C-based age correction for Unit 6 deposits of 25 ± 2.5 years.

Cryptotephra analysis: The LP16 record contains two visible Holocene tephra deposits, between ~35–32 cm (5,720 ± 130–3,970 ± 230 cal yr BP), and between 13–12 cm (540 ± 220–420 ± 300 cal yr BP). The age of the LP16: 35–32 cm tephra is consistent with a prominent cryptotephra peaks at ~252 cm (4740 ± 130 cal yr BP) in the LP08 record (Figure 5, S2). A further cryptotephra deposit, also characterized by MS, Ti, Sr, Si peaks within the organic matrix layer, occurs at ~29–25 cm (3020 ± 180 cal yr BP). EPMA data produced thus far from glass shards at 12.5, 32 and 57 cm depth in the LP16 record produced mixed results with no clear match to known eruptions (Figure S9, S10). In common with some other records from the Torres del Paine and peat records from further south in Patagonia, EPMA analysis of cryptotephra undertaken thus far shows a large geochemical spread, broadly affiliated to the Austral Volcanic Zone (rhyolitic), but with no individual deposit correlating convincingly with any of the major Holocene eruptions of Reclus, Aguilera, Burney, or Hudson in the Southern Volcanic Zone (Andesitic). No Holocene-age ash layers were visible in the LP08 record and, thus far, we have found no (crypto)tephra of a similar age to the Hudson H1 tephra at c. 8,700 cal yr BP (Smith et al., 2019). Cryptotephra in the LP08 record between 338–334 cm (6,140 ± 540–5980 ± 480 cal yr BP cal yr BP) is characterized by peaks in MS, Ti, Sr, Si within the organic matrix (Figure 5A, S2). This could possibly relate to the ChaA1 eruption of the Chaitén volcano (>6000, but <7450 cal yr BP) (Fontijn et al., 2014), which deposited ash southwards across Patagonia but this requires further investigation.

Core Scanning Results: For Mo-tube 2 mm datasets with 10 second count time, Al and Rb cps were considered too low for reliable normalization, particularly in organic-rich sections of the record; hence, we present data as total scatter-normalised and element/Titanium (Ti) normalized percentage ratios and $\log_{10}$ or natural log-ratios (Figure 5, 6, 8, 10, S2, S3). The LP08 2 mm dataset (mastercore, filtered data) has a mean ± 1σ kcps = 18,776 ± 3218 and mean MSE = 1.33 ± 0.12 (n = 2885), the LP08 200 μm-2 mm dataset has a mean ± 1σ kcps = 16,187 ± 2606 and mean MSE = 1.28 ± 0.10 (n = 9059); the LP16 2 mm dataset has a mean ± 1σ kcps = 21,080 ± 2441 and mean MSE = 1.47 ± 0.11 (n = 1444) and the LP16 200 μm-2 mm dataset has a mean ± 1σ kcps = 20,778 ± 2187 and mean MSE = 1.50 ± 0.13 (n = 10,712). The TSN ratio sum for LP08 is correlated with coh./inc. and both relate to changes in dry mass (Boyle et al., 2015) (r values >0.80; p<0.0001) (Figure S4; Table S1). Other correlations between key variables from subsample and XRF-CS data are summarised in Table S1. Downcore PC axes 1 and 2 explain 67.5% and 11.7% of the variance in the LP08 2 mm dataset and 67.8% and 12.5% of the variance in the LP16 200 μm-2 mm dataset (Figure S2, S3).

The LP08 and LP16 records were divided into six lithofacies units shown in Figure 5, Table 2 and summarised as follows:

Unit 1: Unit 1 is characterised by high to moderate MS, high Ti, Rb, with high and stable Fe/Mn and Sr/Ca associated with glaciogenic physical weathering products and allochthonous catchment erosion (Figure 5). Low organic matter (including Br) content, together with a lack of authigenic enrichment of redox-sensitive trace elements (e.g., V/Ti), suggests deposition under low productivity and generally well-ventilated bottom water conditions. Unit 1 represents the 'background' glaciogenic detrital composition, with well-developed fine scale internal structure, most notably within Unit 1A (Figure 6B–F). Fe/Mn and Mn/Ti ratios are inversely related in LP08 in general (r = -0.65; p = 0.0047) and within Unit 1, with well-developed decadal to centennial scale variability present between the Ti- and Ca-rich orange-grey and light grey laminations (Figure 6B–F).

Units 2–4: The detrital component of Unit 2 is composed of light grey (glaciogenic) silty clay, similarly enriched in Ti, K, Fe and Mn to Unit 1, but massive and embedded with subaquatic *Myriophyllum* sp. fragments. Unit 3 is composed entirely of shallow water sub-aquatic *Myriophyllum* sp., an early colonizer (Figure 5B). The moderate to low MS and Ti and elevated Br content of Unit

3 implies declining input of glaciogenic physical weathering products and increase in the organic matter content, biogenic activity, and productivity in the lake. Unit 4 is similar to Unit 2 but distinguished by substantial enrichment in Ca and Sr (but not S) and a lower density of *Myriophyllum* sp. fragments (Figure 5B).

Units 5–6: Unit 5 is structureless organic lake mud characterized by very low MS, low Ti content, high Br (and other organic proxies) and higher (more terrestrial) C/N values than Unit 1, which reflect increased productivity in a shallower basin. Unit 5A in LP16 has extremely high Fe/Mn ratios which reflect an 'Anoxic Crisis' during a period of lower water levels (and possibly peat formation), as conditions became and calmer and more stable at the LP16 site. Units 5B–C between c. 10–5.6 cal ka BP are characterised by increased erosional inputs (shown by elevated MS and Mn/Ti), with Fe/Mn remaining low and occasional exceptionally elevated Ca and S in LP08 (Figure 5A), whereas, in LP16, MS remained low, with significantly increased Mn/Ti and Fe/Mn (Figure 5B). Unit 6 is a highly organic, structureless and increasingly fibrous macrophytic lake mud depleted in low detrital elements, with low Mn/Ti and increasing Fe/Mn ratios (more anoxic/stable) in LP08 and decreasing Fe/Mn ratios in LP16 (more oxic/less stable).

We classified element and element/total scatter ratios into five groups:

1) *Catchment erosion proxies:* Here, we used: >Ti/inc.+coh. >coh./inc. ratio and >MS as proxies for increasing detrital clastic (minerogenic) input; >(Fe+Ti)/K or Ti/K as a grain size indicator, compared to the clay fraction with >Rb/Ti reflecting increased clay input (Davies et al., 2015); >Sr/Ti for increased detrital input during the glaciogenic sediments and soil erosion in the non-glacial deposits, coupled >Si/Ti, >K, >Ti, >MS to identify tephra deposits; concomitant >Sr/Ti + >Si/Ti to identify outwash sands; coupled >Mn/inc.+coh, >Fe/Ti, >Mn/Ti, >MS in glaciolacustrine deposits to identify magnetite-rich sediments and erosional layers and >Mn/Ca and >MS to locate cryptotephra deposits.

2) *Redox proxies:* Elevated Fe/Mn and Mn/Ti ratios have been interpreted as representing increased stability and anoxia, which, combined with <Ca/Ti and <Sr/Ti, reflect increased water depth in Lago Pato. This is because Mn^{2+} is more stable in pore water and precipitates later than Fe^{2+}, while Mn is more soluble than Fe in anoxic conditions, leading to lower Fe/Mn ratios in sediment profiles during periods of lake anoxia (Wennrich et al., 2014; Davies et al., 2015). Although Fe has many potential sources, including detrital inputs, elevated Fe counts often reflect increased water column stratification and anoxia in very deep and otherwise unproductive proglacial lakes, and a lack of mixing in more productive and shallower lakes (Kylander et al., 2011). Hence, higher Fe/Mn ratios reflect greater stability and stratification. High Mn and magnetite solubility also occur in more anoxic conditions, particularly at depth and with perennial lake ice-cover, associated with colder glacial conditions (Melles et al., 2012; Olsen et al., 2013; Wennrich et al., 2014; Davies et al., 2015). Conversely, higher Mn/Ti and <Fe/Mn ratios have been widely used as indicators of increased oxidation, particularly where wind-driven mixing of the lake water column in deep water and glaciolacustrine environments or in shallow–dry lakes overturns stratification and reduces Mn solubility causing manganese oxides and hydroxides to co-precipitate with iron oxy-hydroxides (Wennrich et al., 2014; Davies et al., 2015). Elevated S/Ti in Units 6C and D has a strong association with elevated Br/Ti (r2 = 0.91; Figure S4F). In most non-marine environments, and in Lago Pato, Br has a particularly strong association with organic material and lower Fe/Mn ratios (Davies et al., 2015). An exception occurs in shallow–littoral organic (possibly terrestrial deposits) (e.g., LP16 Units 4–5) where exceptionally elevated Fe/Mn ratios, reflecting a very anoxic environment ('Anoxic crisis' in Figure 5, 8, 10), are covariant with elevated inc./coh., Br and S ratios (Figure 5, 6A). The shallow water organic-rich environments of Units 5A and B have higher S/inc.+coh. and S/Ti ratios than Units 1 and 2 (Figure S4), reflecting increased eutrophication-driven anoxia, limited ventilation, and greater stability.

3) *Carbonate deposition proxies:* We identified the following modes of Ca- and carbonate-deposition:
   i. *Minerogenic, catchment-derived Ca:* In this mode, Ca is principally covariant with erosional elements. Relatively low Ca content throughout Unit 1 is associated with the low-Ca and high-Rb content of fine clays eroded from an enlarged catchment.
   ii. *Minerogenic Sr- and Ca-rich:* Elevated Ca and Sr between, for example, ~ 42-43 cm in LP08 are caused by the inwash of fine sandy-silt minerogenic Sr-rich deposit (labelled S, in Figure 5A). All major measurable minerogenic elements (K, Ti, Fe, Rb, Sr, Ca) are significantly elevated above background organic values, distinguishing Sr and Ca peaks from those formed by cryptotephra. The similarity between paired ages from bulk organic mud and plant remains between 41–40 cm indicates minimal carbonate impact on radiocarbon ages.
   iii. *Authigenic carbonate (evaporation and precipitation related).* In this mode, elevated Ca is associated with Sr and S. Precipitation of calcite, carbonates and, eventually, evaporites progresses rapidly in some closed, cold-water, high latitude and/or density-stratified (heliothermal-hypersaline) lacustrine environments (Lauterbach et al., 2011; Jouve et al., 2013; Olsen et al., 2013). Elevated Ca and S in combination have been associated with formation of $CaSO_4$ (gypsum) (Brown, 2011; Hodell et al., 2012; Mueller et al., 2017), common in semi-arid environments of the northern high Andes with a dry steppe climate (Farias et al., 2014). Carbonate-rich evaporation rinds exist around ion-concentrated, closed-shallow brackish lakes in Southern Chile (Campos et al., 1995).
   iv. *Anoxia:* This mode occurs where elevated S conditions become decoupled from Ca during stratification, suggesting anoxic (and poorly ventilated) conditions developed as in-lake productivity rose (Kylander et al., 2011)

4) *Organic proxies:* Incoherent/coherent (inc./coh.$_{Mo}$) ratios obtained from Mo-tube analysis reflect changes in water content and sediment density in the LP08 and LP16 records, and have been used as proxies for organic content (%TOC and/or Loss-on-ignition) (Jouve et al., 2013; Davies et al., 2015; Roberts et al., 2017). Organic material is less dense, and more water saturated, and higher inc./coh.$_{Mo}$ ratios show a strong and significant correlation with >TOC and >Br (inc/coh – TOC: $r^2 = 0.94$, Br-TOC: $r^2 = 0.84$; $p<0.0001$ for both; Figure 5A; Figure S4).

5) *Matrix effects:* These occur when scanning wet, organic-rich deposits (Kylander et al., 2011; Davies et al., 2015). Elevated levels of Zr are commonly found in sand-size grains and variations in Zr have been used as a proxy for changes in grain-size elsewhere. While stable values in Unit 1 in both records reflect the consistently fine-grained minerogenic nature of (glaciolacustrine) sediments deposited, elevated Zr values in the more organic-rich units 5 and 6 most likely represent a matrix effect caused by Zr being adjacent to the Mo-incoherence peak in the energy spectra (Figure S5).

Diatom analysis: Where possible, a distinction was made between different morphotypes in the groups of the small benthic *Fragilariod* species (e.g., *Staurosirella aff. pinnata*; *Staurosira aff. venter*) (Figure S7). These groups may be the same species but still exhibit different ecological responses. Further studies are needed to understand these distinct ecological shifts within the *Fragilaria* species in general, and, more specifically, in the LP08 and LP16 records (Figure S7) (Einarsson et al., 2004; Finkelstein and Gajewski, 2008; Bennion et al., 2010) since the full significance of these shifts is not currently understood (Westover et al., 2006; Bennion et al., 2010). Nevertheless, the size and shape of valves within one diatom species can reflect different environmental conditions (Stevenson et al., 1999; Stevenson et al., 2010).

3. Supplementary Figures

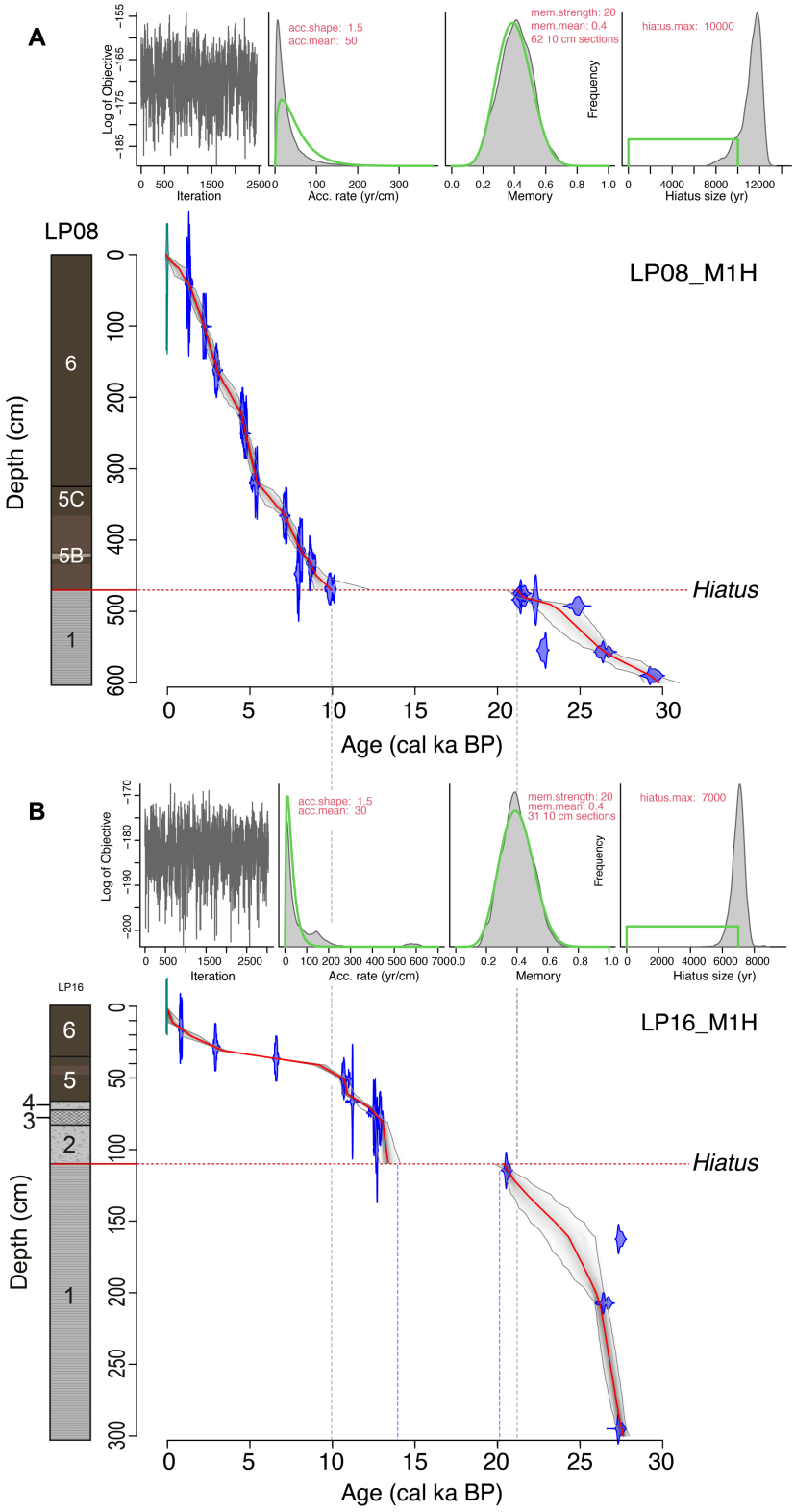

Figure S1. Summary of age depth models for Lago Pato sediment records **(A)** LP08 and **(B)** LP16 constructed using BACON v.2.4 (Bayesian) age-depth modelling software in R v3.1 using the SHCal120.14C Southern Hemisphere atmosphere dataset (Hogg et al., 2020). Prior settings are shown in the inset boxes. Data and code can be found at: https://github.com/stever60/Lago_Pato.

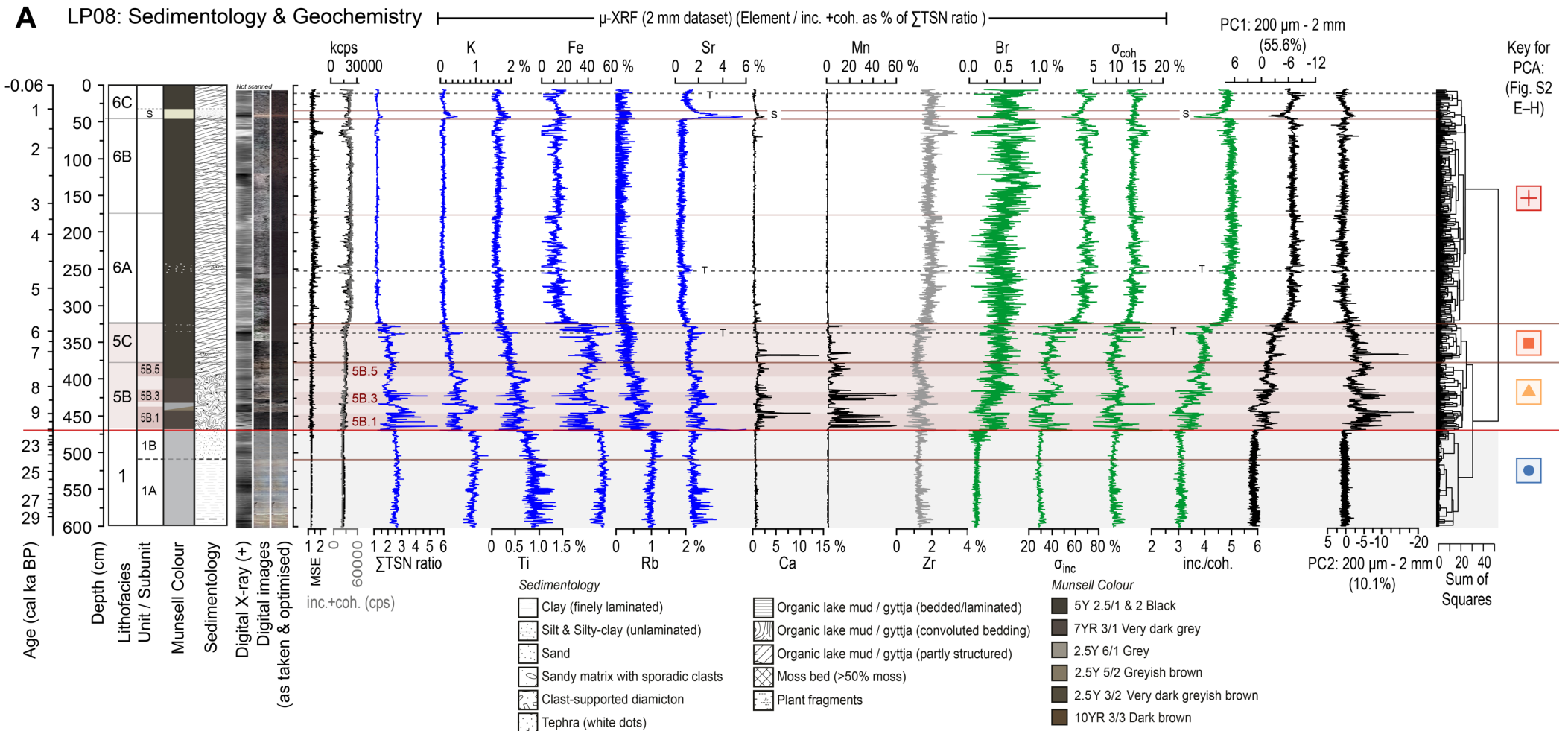

Figure S2. (A) Summary sedimentological logs and downcore XRF-CS composite 2 mm dataset for the Lago Pato sediment record. Plot colours for elements and scattering parameters reflect minerogenic versus organic affinities. Blue plots have a significant and strongly positive relationship to TSN ratios (Pearson correlation coefficient (PCC) r>0.5; p<0.0001; R^2>0.5) and a significant negative relationship with inc./coh. ratios (PCC<-0.5; p<0.0001; R^2>0.5). Green plots are positively correlated with inc./coh. ratios., while black plots show no strong relationship to TSN or inc./coh ratios. Elevated Zr in organic-rich Unit 6 is a matrix effect (Figure S5). The scanning location of cryptotephra deposits was confirmed by pollen counting. S is a fine-grained Sr-rich minerogenic outwash sand layer. Correlation and PCA analysis plots shown in this diagram are summarised in (B)–(H) overpage.

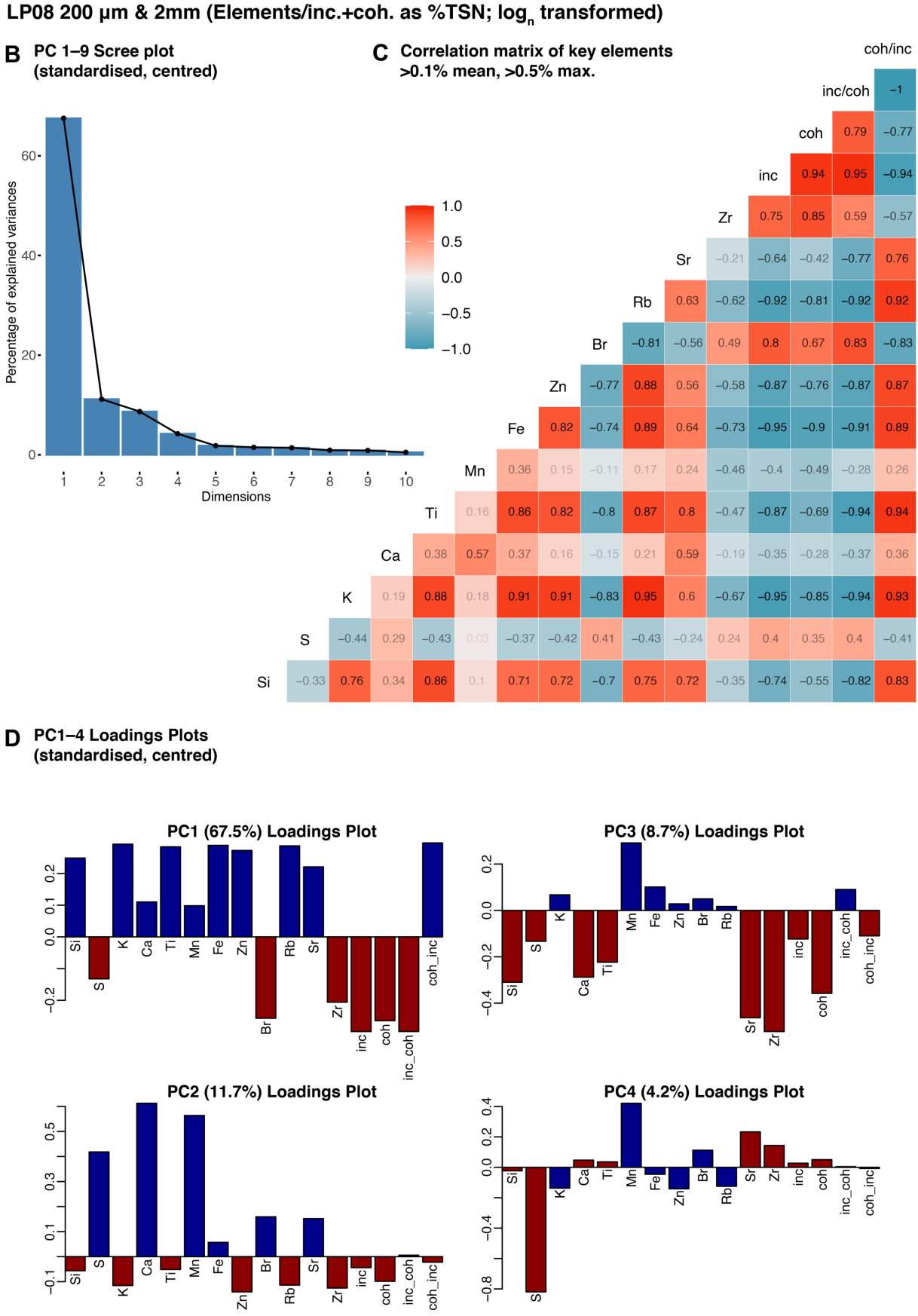

Figure S2. (B) Scree plot summarizing the percentage of variance explained by PC dimensions PC1–9. **(C)** Correlation matrix for key elements and scatter parameters and ratios present in

the LP08 200 µm–2 mm dataset (n = 9,059). Key elements were defined as having a mean >0.1% TSN value and a maximum TSN value of 0.5% or greater. **(D)** Loadings plots for PC1–4 summarising positive and negative element groups. **(E–H) below:** PC1-4 biplot combinations and summary interpretation of each axis for the LP08 200 µm–2 mm dataset, grouped by unit, as defined by CONISS cluster analysis, shown in (A). Data were $\log_n$ transformed, centred, and standardised (Z-scores) for PCA analysis. Data and code can be found at: https://github.com/stever60/Lago_Pato.

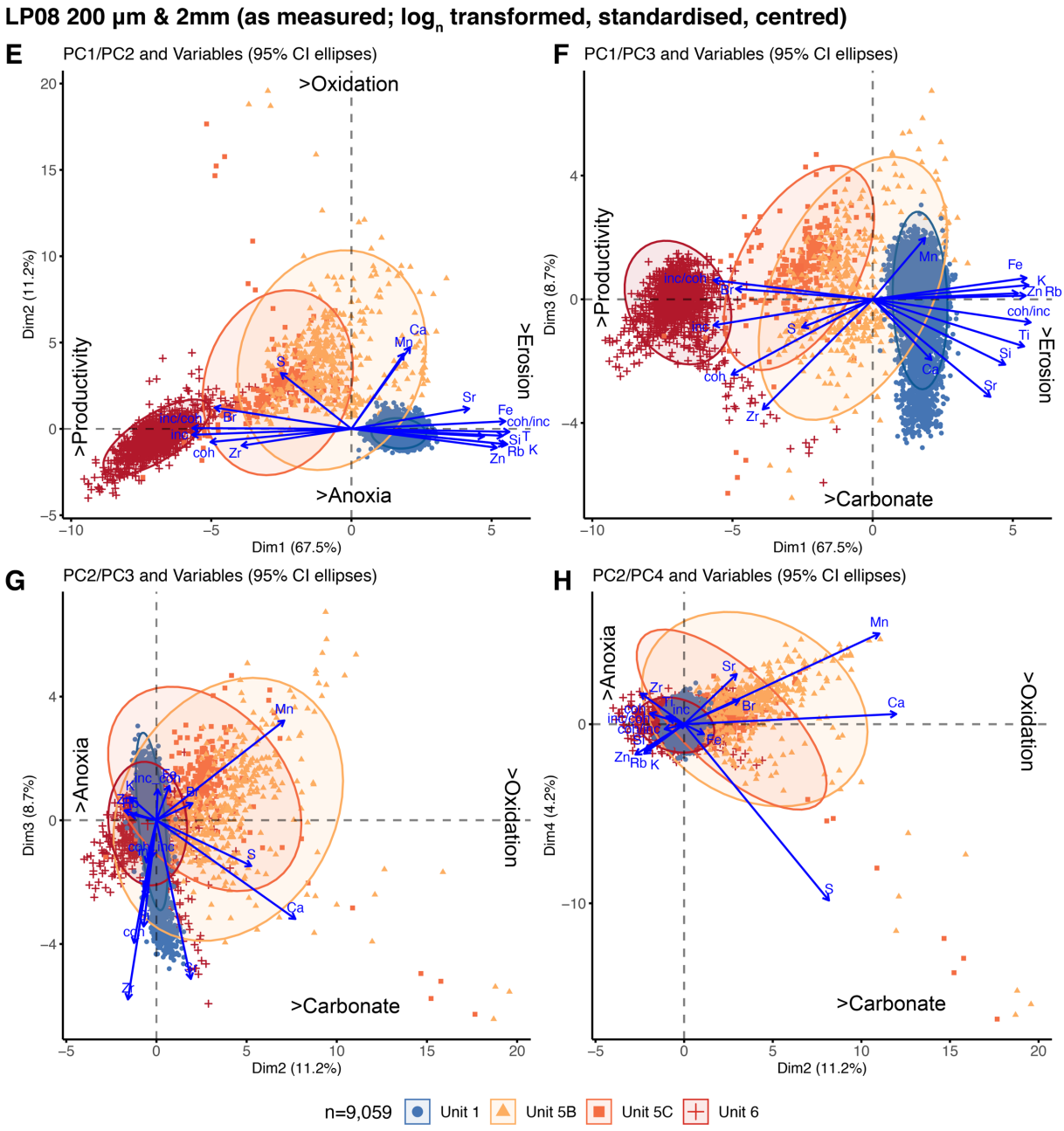

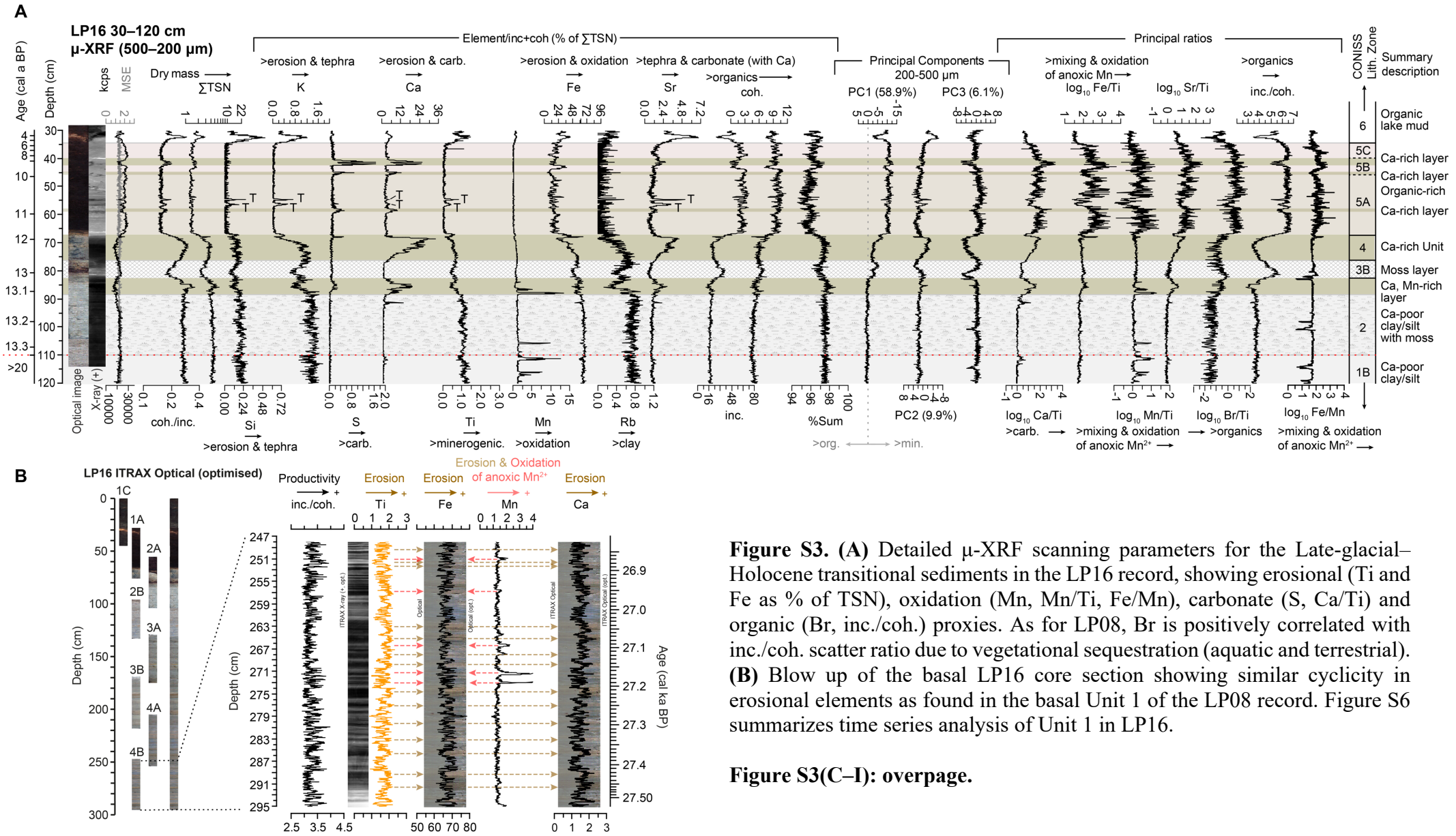

Figure S3. (A) Detailed µ-XRF scanning parameters for the Late-glacial–Holocene transitional sediments in the LP16 record, showing erosional (Ti and Fe as % of TSN), oxidation (Mn, Mn/Ti, Fe/Mn), carbonate (S, Ca/Ti) and organic (Br, inc./coh.) proxies. As for LP08, Br is positively correlated with inc./coh. scatter ratio due to vegetational sequestration (aquatic and terrestrial). **(B)** Blow up of the basal LP16 core section showing similar cyclicity in erosional elements as found in the basal Unit 1 of the LP08 record. Figure S6 summarizes time series analysis of Unit 1 in LP16.

Figure S3(C–I): overpage.

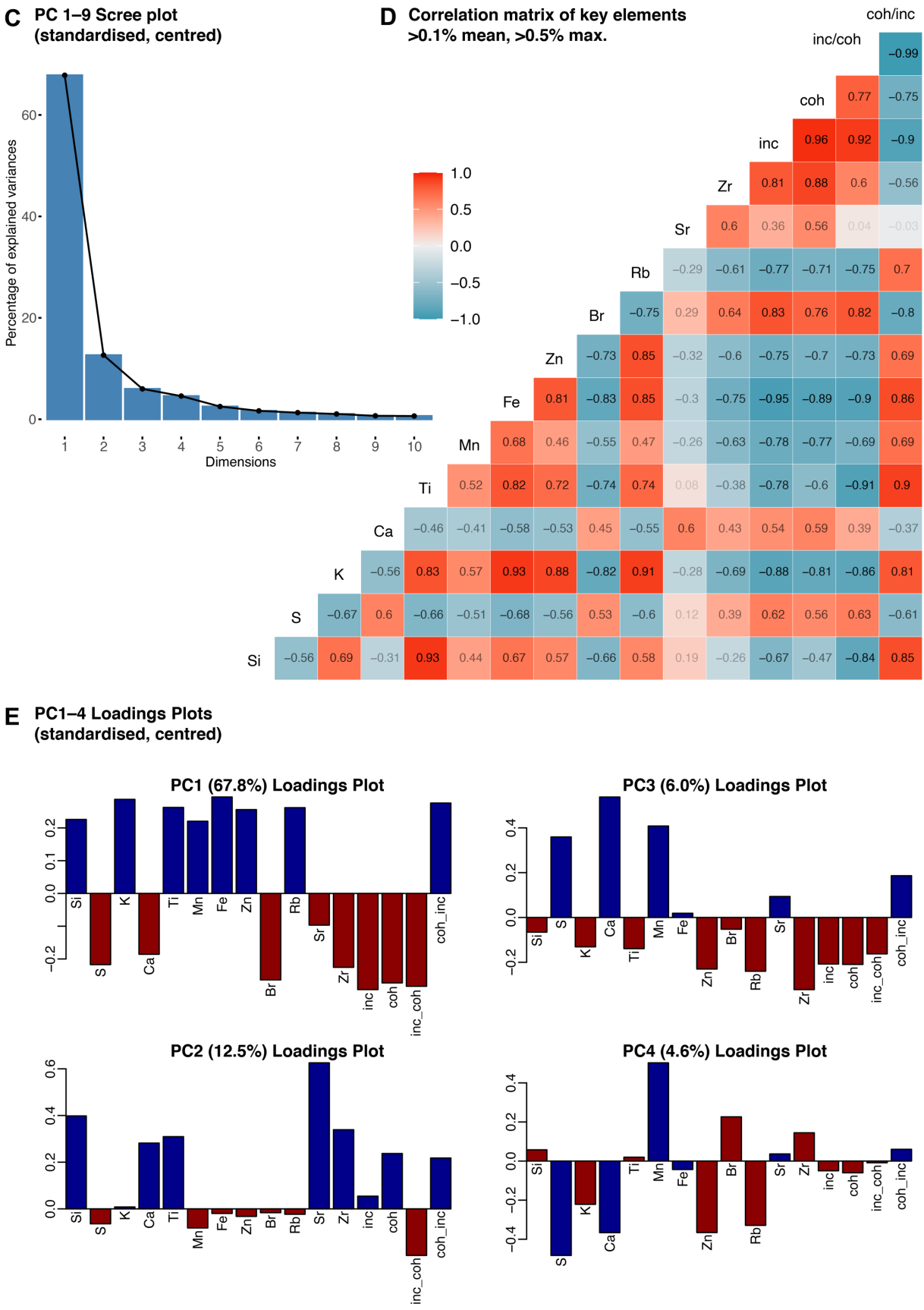

Figure S3. (C) Scree plot summarizing the percentage of variance explained by PC dimensions PC1–9 for the LP16 200–500 µm dataset (n = 10,712). **(D)** Correlation matrix for key elements and scatter parameters and ratios present in the LP16 200–500 µm dataset. Key elements were defined as having a mean >0.1% TSN value and a maximum TSN value of 0.5% or greater. **(E)**

Loadings plots for PC1–4 summarising positive and negative element groups. **(F–I) below** PC1-4 biplot combinations and summary interpretation of each axis for the LP16 200–500 µm dataset grouped by unit, as defined by CONISS cluster analysis, shown in (A). Data were $\log_n$ transformed, centred, and standardised (Z-scores) for PCA analysis. Data and code can be found at: https://github.com/stever60/Lago_Pato.

LP16 200–500 µm (Elements/inc.+coh. as %TSN; $\log_n$ transformed standardised, centred)

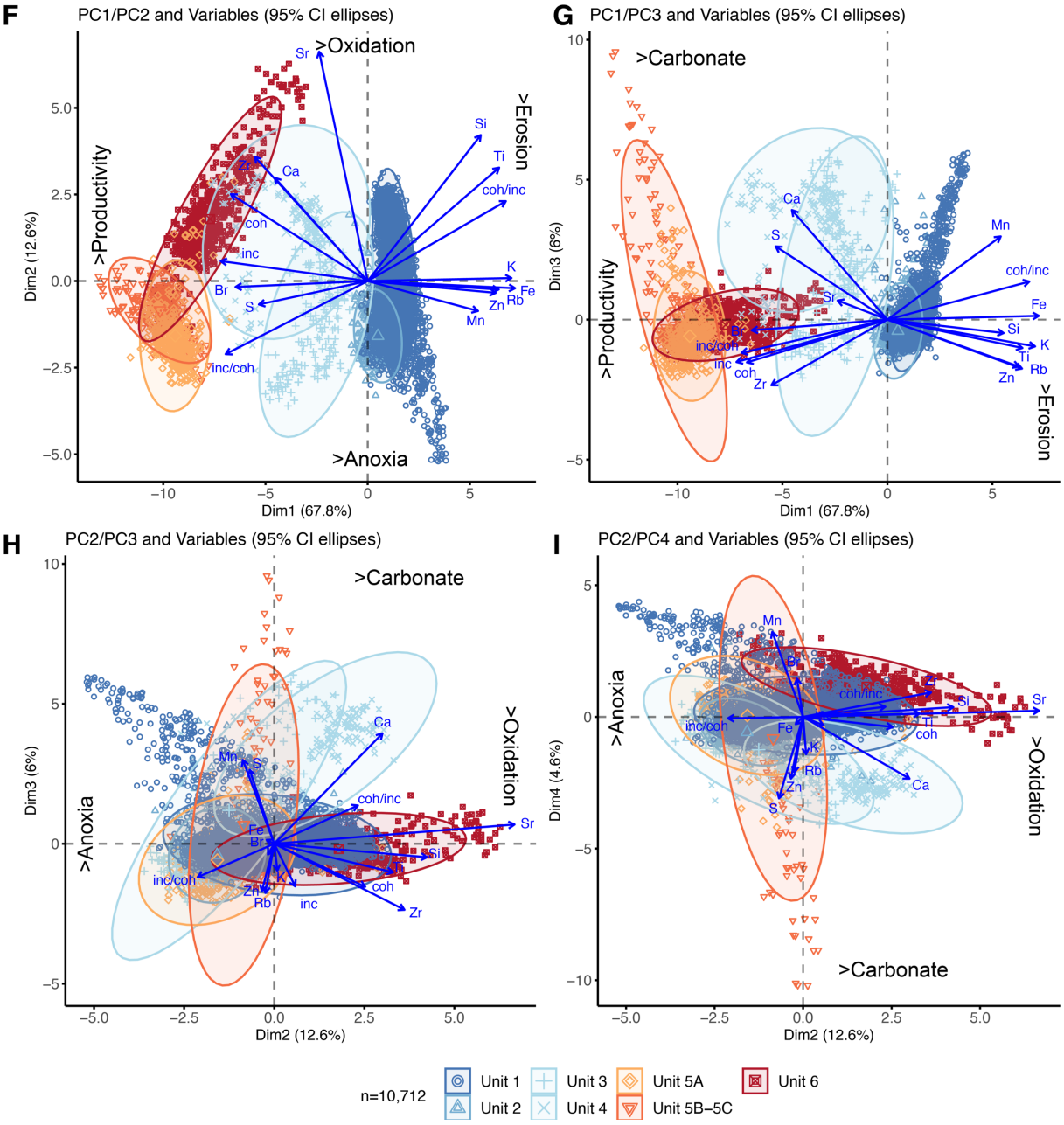

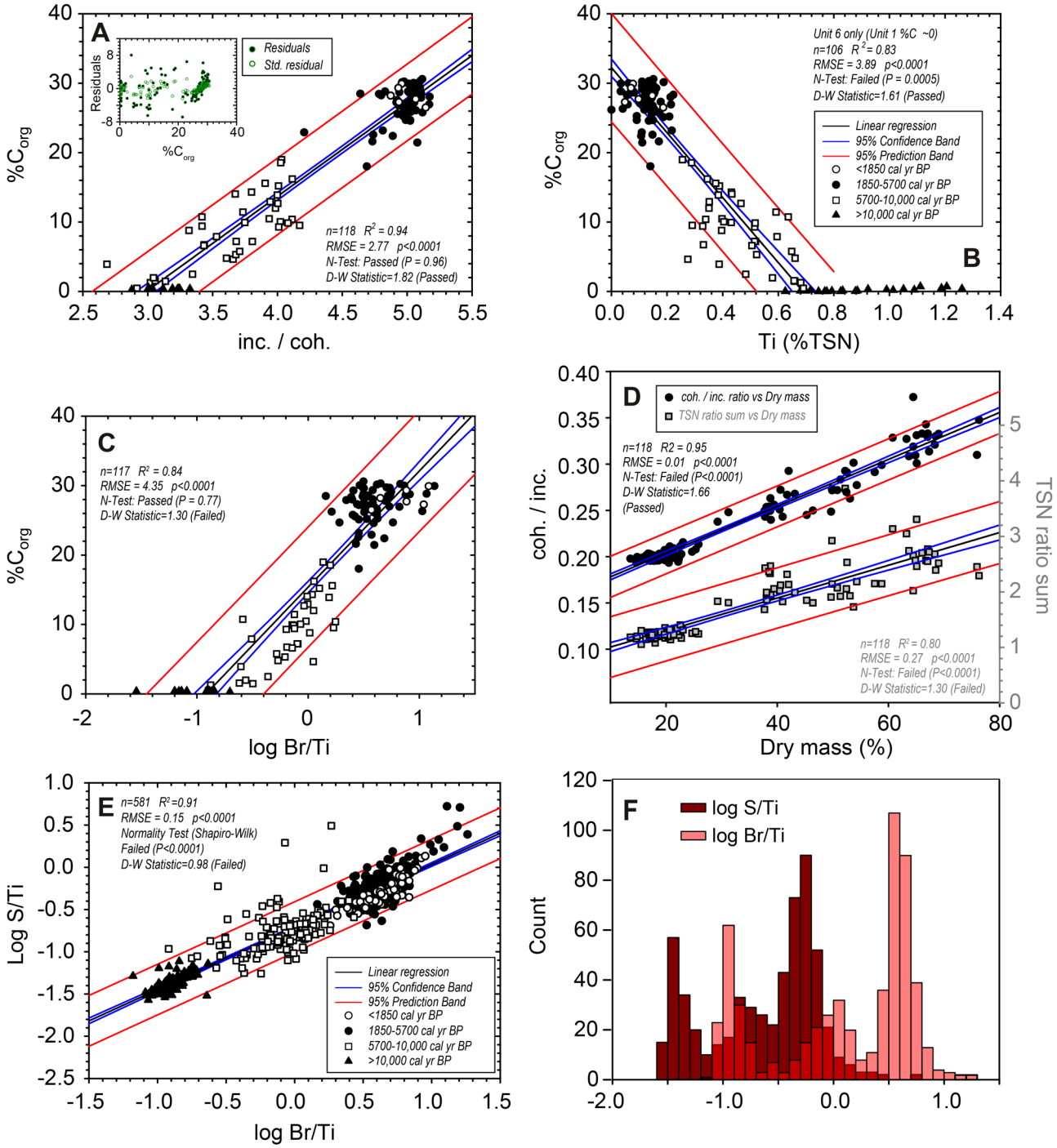

Figure S4. Regression analysis and comparison of key productivity- and erosion-related XRF-CS parameters in the LP08 1 cm dataset. Organic carbon (C_{org}) subsample data are plotted against: **(A)** inc./coh. scatter ratio. **(B)** Ti (expressed as % of TSN ratio). **(C)** Log (Br/Ti). **(D)** Regression analysis of the TSN ratio (ø) and coh. / inc. ratio with subsample dry mass data. **(E), (F)** Regression analysis of log (S/Ti) against log (Br/Ti) showing the significant correlation between Br and S and histograms showing distinct phases of organic sedimentation with different data distributions and count levels for Br and S enrichment. In summary, these graphs show that three clearly defined organic carbon zones existed at: >c. 10 cal ka BP (Unit 1), between c. 10–5.7 cl ka BP (Unit 5), 5.7–1.9 cal ka BP (Unit 6). The inc./coh. scatter ratio is strongly and significantly correlated to $\%C_{org}$ ($n = 118$; $r = 0.96$; $p<0.0001$; $R^2 = 0.94$), passing Shapiro-Wilkinson normality and auto-correlation (N-test) tests. Log (Br/Ti) vs $\%C_{org}$ (not shown) log (Br/Ti) vs log(S/Ti) ($n = 581$; $r = 0.95$; $p<0.0001$; $R^2 = 0.91$) are also strongly and significantly correlated but Br/Ti and S/Ti datasets fail normal distribution tests. Regression analysis involving Br/Ti fails autocorrelation tests. No direct matches between subsample and core scan data were possible for data younger than c. 1.4 cal ka BP. D-W is the Durbin-Watson

Statistic run at 5% significance level to test for autocorrelation in residuals, with zero representing a strong positive serial correlation, four a strong negative serial correlation and two no autocorrelation. For all datasets, n>50, i.e., above the recommended upper sample size limit for N- and D-W tests.

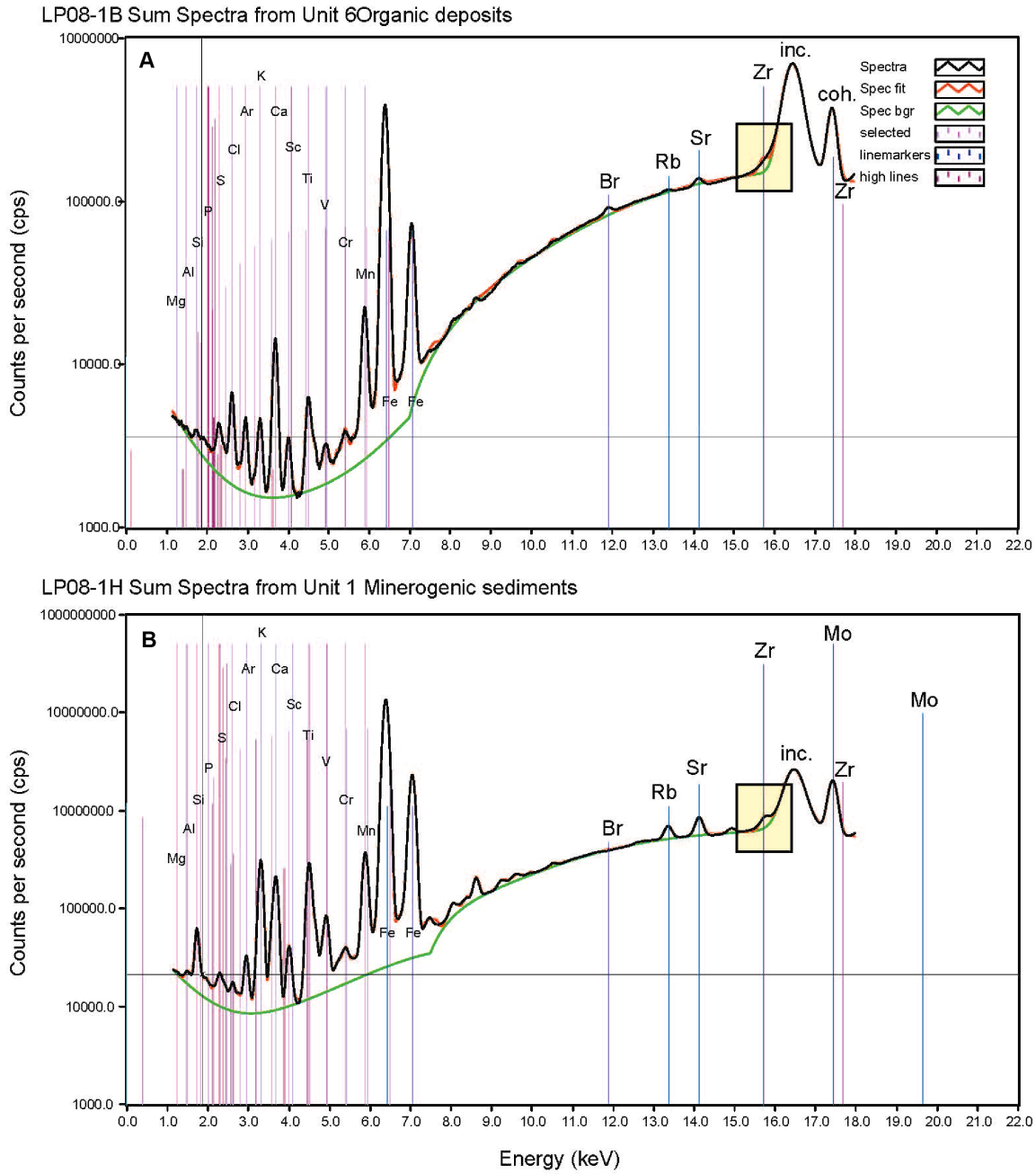

Figure S5. XRF core scanning sumspectra profiles for core **(A)** PAT1B and **(B)** PAT1H showing contrasting spectra obtained organic- and minerogenic-dominated sediment matrices. The spectra mismatch for Zr is due to an organic matrix effect that artificially elevates Zr cps, rendering this element unreliable as a grain size proxy in the upper half of the Lago Pato core.

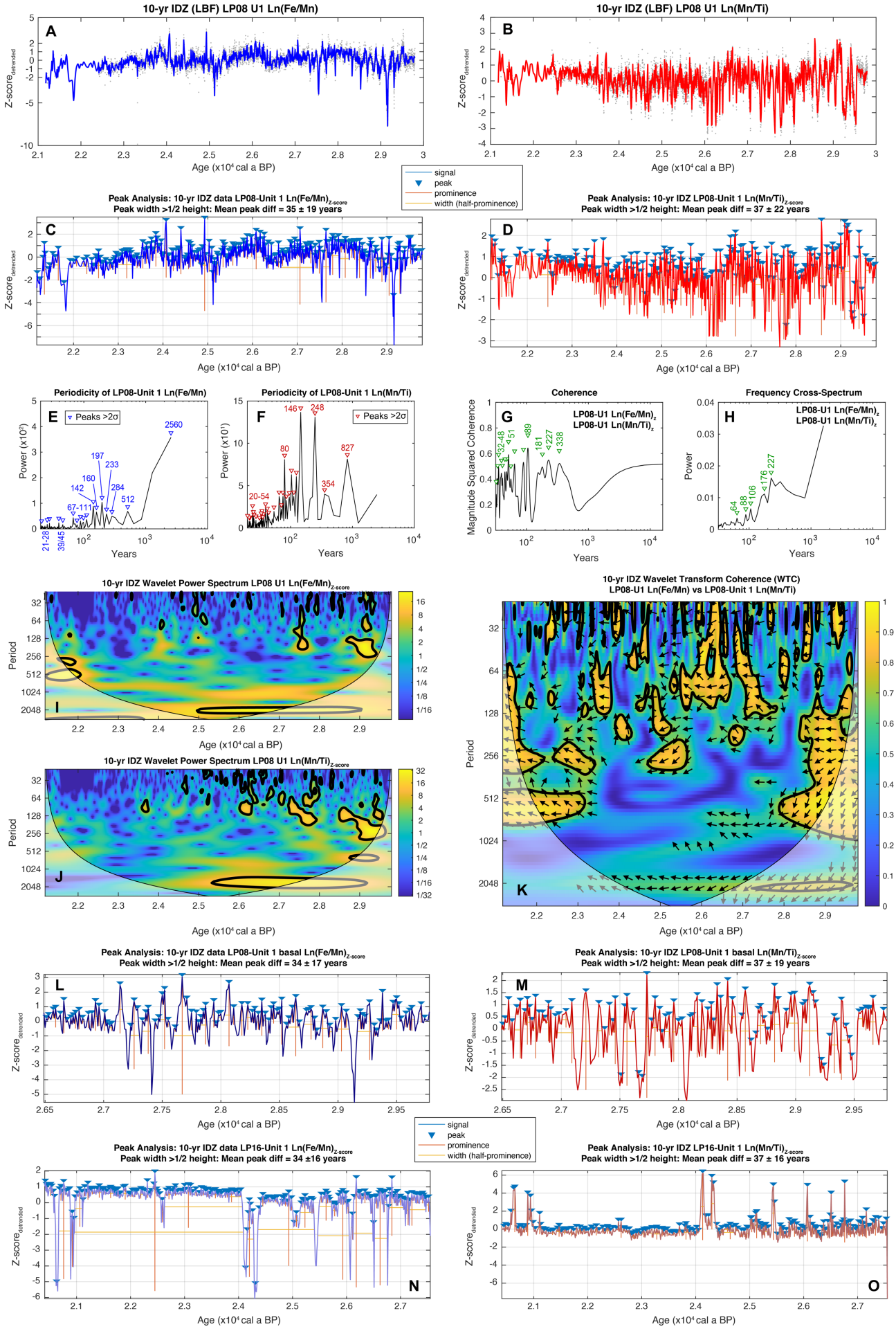

Figure S6. Time series, peak analysis, and wavelet power spectral analysis for the 10-year PCHIP (Piecewise Cubic Hermite Interpolating Polynomial) interpolated datasets from the 200 μm LP08

Unit 1, LP08 Unit 1 basal core section and LP16 Unit datasets**(A)** $Ln(Fe/Mn)_{Z\text{-}scores}$ (blue line) and **(B)** $Ln(Mn/Ti)_{Z\text{-}scores}$ (red line) from Unit 1 in the LP08 record. The mean sample interval for the dataset (grey dots) is 1.26 ± 4.23 years. **(C)** Peak identification and interval analysis for $Ln(Fe/Mn)_{Z\text{-}scores}$ from the LP08 Unit 1 dataset, resulting in a mean peak difference of 35 ± 19 years. Prominent peaks were defined as peak width being greater than half its height. **(D)** Peak identification and interval analysis for the LP08 Unit 1 $Ln(Mn/Ti)_{Z\text{-}scores}$ dataset resulting in a mean peak difference of 37 ± 22 years. **(E, F)** Power spectrum periodicity for interpolated and detrended LP08 Unit 1 $Ln(Fe/Mn)_{Z\text{-}scores}$ (blue) and $Ln(Mn/Ti)_{Z\text{-}scores}$ (red). **(G, H)** Cross-coherence and cross-spectrum bi-plots for interpolated and detrended $Ln(Mn/Ti)_{Z\text{-}scores}$ and $Ln(Fe/Mn)_{Z\text{-}scores}$ datasets with prominent centennial scale periodicities highlighted. **(I, J, K)** Wavelet power spectrum and wavelet transform coherence (WTC) plots (Grinsted et al., 2004) showing centennial-scale periodicity and time-dependent changes in cycle correlation between $Ln(Mn/Ti)_{Z\text{-}scores}$ and $Ln(Fe/Mn)_{Z\text{-}scores}$ datasets. WTC uses Monte Carlo methods to assess the statistical significance of cross-coherence against red noise in both time series. Significant (>95% confidence) decadal–centennial scale periodicities and correlations are outlined in black. **(L)** Peak identification and interval analysis for $Ln(Fe/Mn)_{Z\text{-}scores}$ from the LP08 Unit 1 basal core section dataset shown in Figure 6C–F, resulting in a mean peak difference of 34 ± 17 years. Prominent peaks were defined as peak width being greater than half its height. **(M)** Peak identification and interval analysis for $Ln(Mn/Ti)_{Z\text{-}scores}$ from the LP08 Unit 1 basal core section dataset shown in Figure 6C–F, resulting in a mean peak difference of 37 ± 19 years. **(N)** Peak identification and interval analysis for $Ln(Fe/Mn)_{Z\text{-}scores}$ from the LP016 Unit 1 dataset, resulting in a mean peak difference of 34 ± 16 years. Prominent peaks were defined as peak width being greater than half its height. **(O)** Peak identification and interval analysis for $Ln(Mn/Ti)_{Z\text{-}scores}$ from the LP08 Unit 1 basal core section dataset shown in Figure 6C–F, resulting in a mean peak difference of 37 ± 15 years. Data and code can be found at: https://github.com/stever60/Lago_Pato.

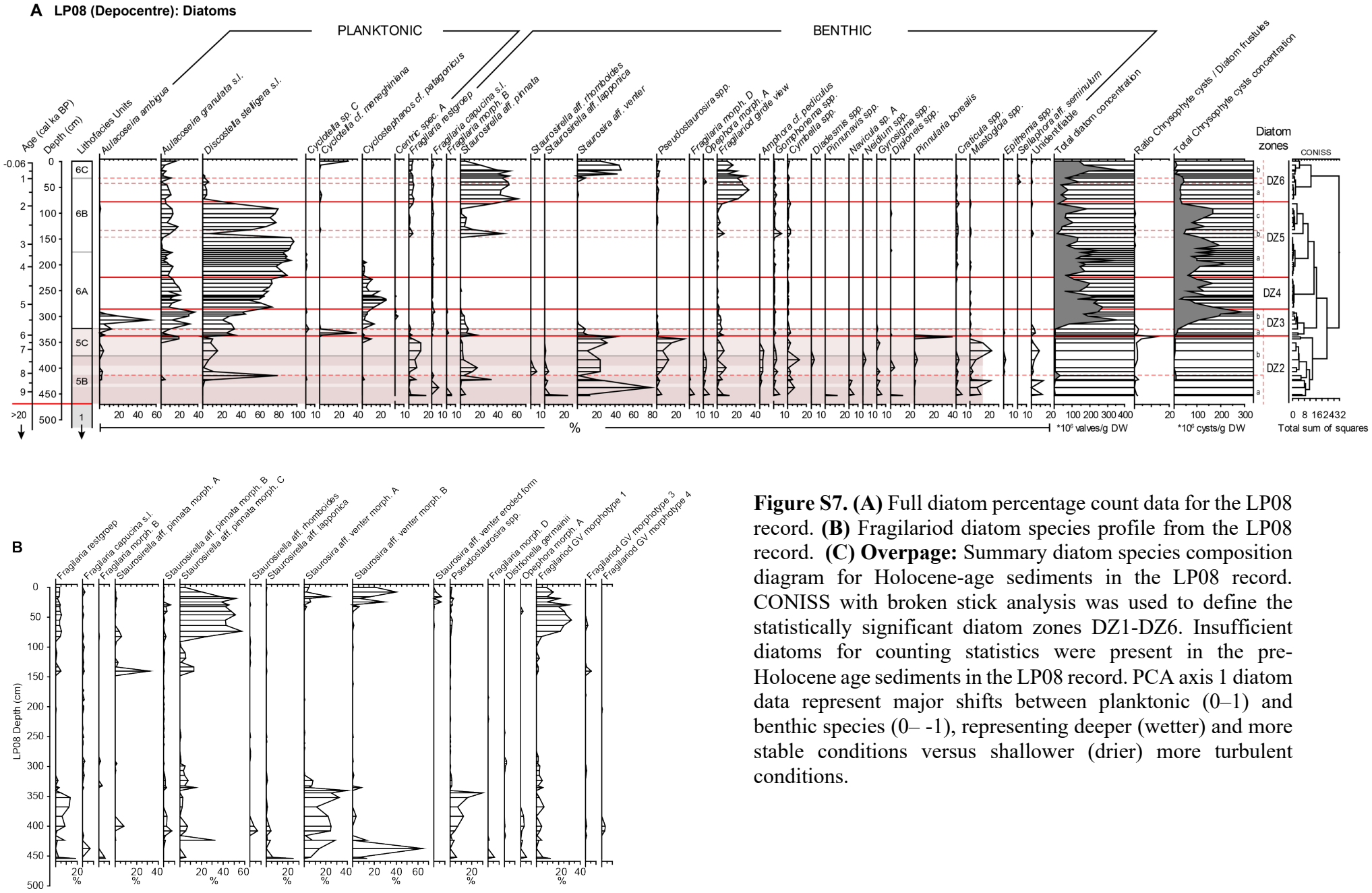

Figure S7. (A) Full diatom percentage count data for the LP08 record. **(B)** Fragilariod diatom species profile from the LP08 record. **(C) Overpage:** Summary diatom species composition diagram for Holocene-age sediments in the LP08 record. CONISS with broken stick analysis was used to define the statistically significant diatom zones DZ1-DZ6. Insufficient diatoms for counting statistics were present in the pre-Holocene age sediments in the LP08 record. PCA axis 1 diatom data represent major shifts between planktonic (0–1) and benthic species (0– -1), representing deeper (wetter) and more stable conditions versus shallower (drier) more turbulent conditions.

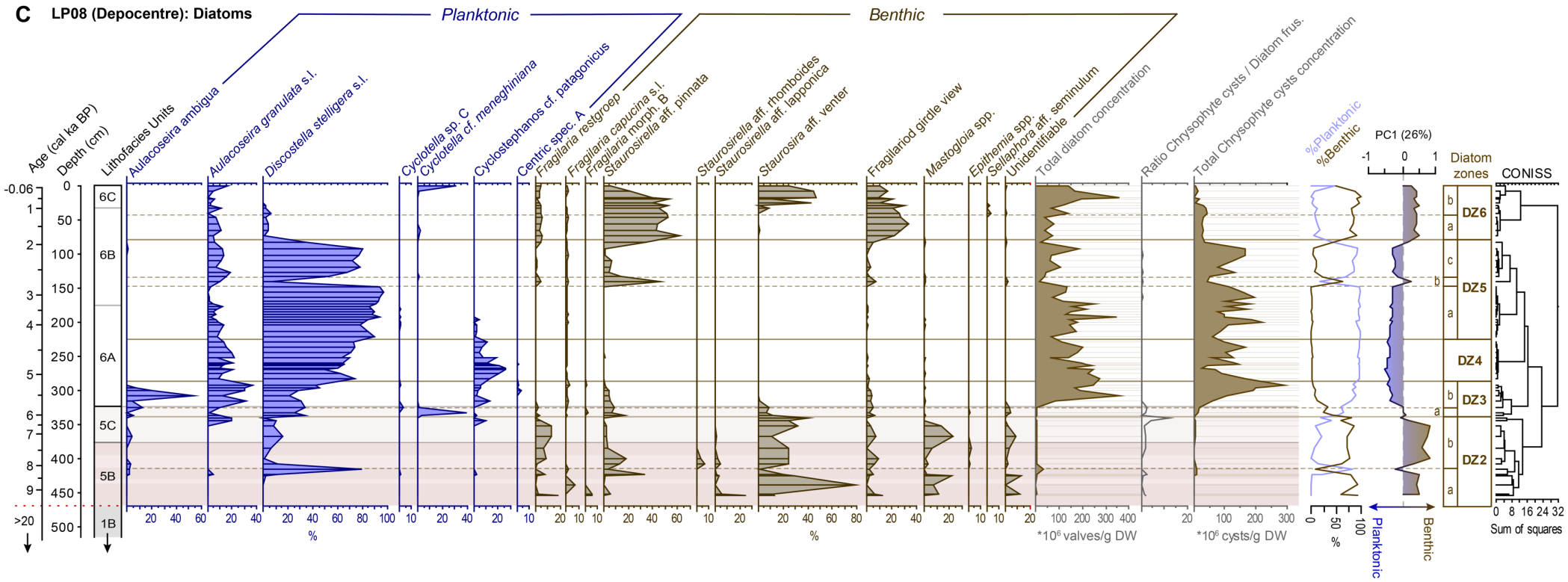
C
LP08 (Depocentre): Diatoms
Planktonic
Benthic
Age (cal ka BP)
Depth (cm)
Lithofacies Units
Aulacoseira ambigua
Aulacoseira granulata s.l.
Discostella stelligera s.l.
Cyclotella sp. C
Cyclotella cf. meneghiniana
Cyclostephanos cf. patagonicus
Centric spec. A
Fragilaria restgroep
Fragilaria capucina s.l.
Fragilaria morph. B
Staurosirella aff. pinnata
Staurosirella aff. rhomboides
Staurosirella aff. lapponica
Staurosira aff. venter
Fragilariod girdle view
Mastogloia spp.
Epithemia spp.
Sellaphora aff. seminulum
Unidentifiable
Total diatom concentration
Ratio Chrysophyte cysts / Diatom frus.
Total Chrysophyte cysts concentration
%Planktonic
%Benthic
PC1 (26%)
Diatom zones
CONISS
6C
6B
6A
5C
5B
1B
DZ6
DZ5
DZ4
DZ3
DZ2
%
*10⁶ valves/g DW
*10⁶ cysts/g DW
Planktonic
Benthic
Sum of squares

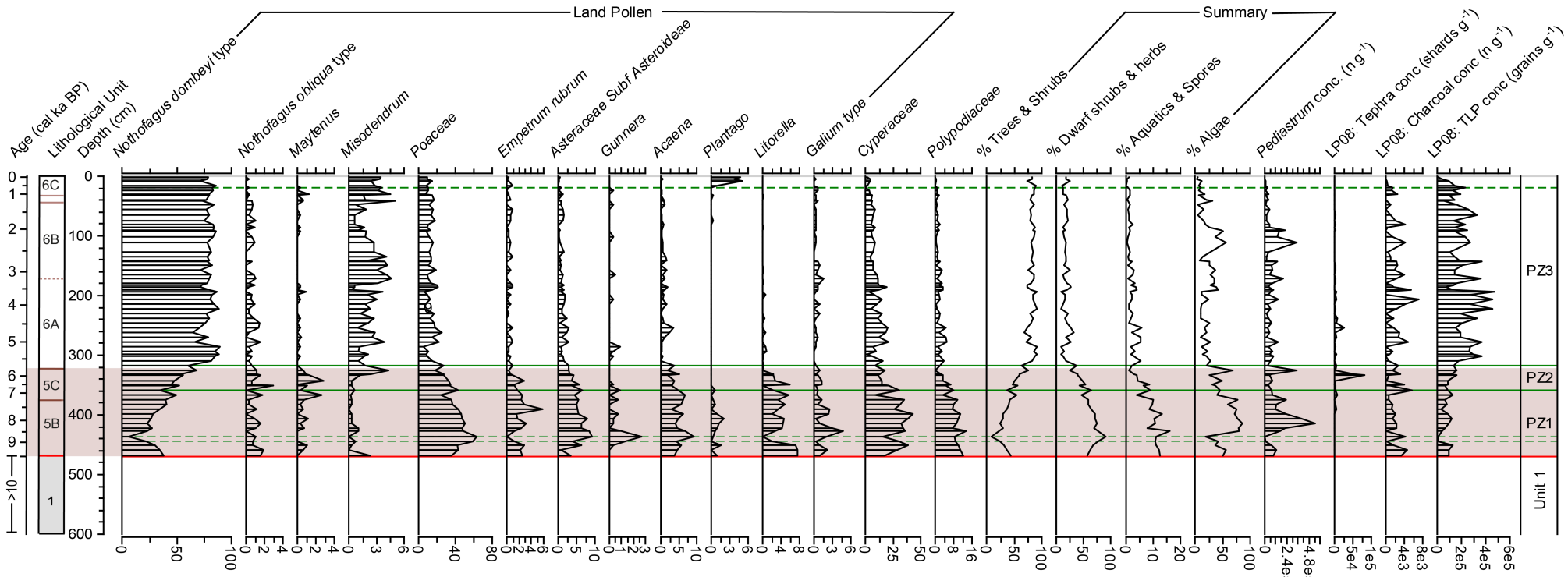

Figure S8. Full pollen count data for the LP08 record.

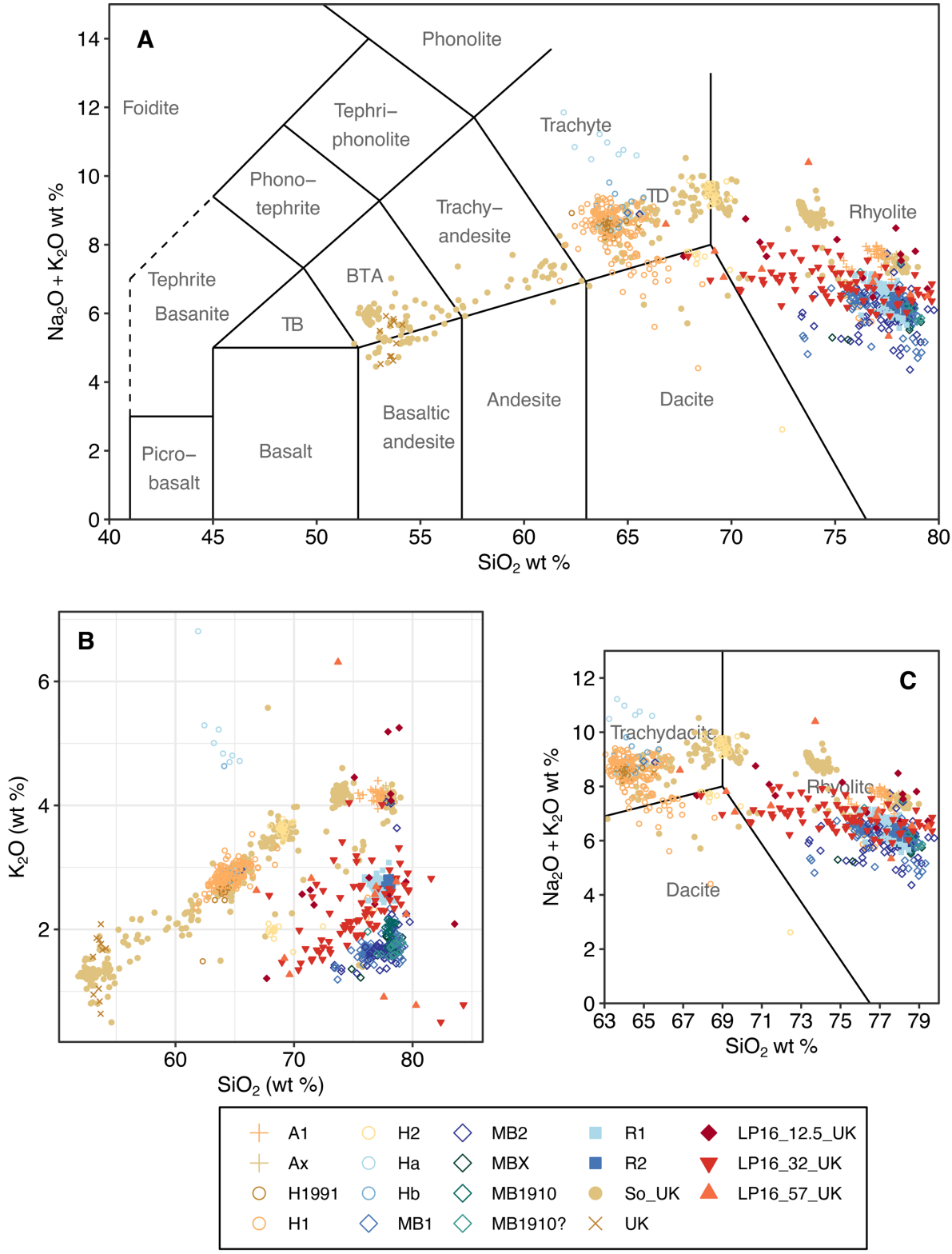

Figure S9. (A) Total Alkali Silica (TAS) (Le Bas et al., 1986) and **(B)** K_2O/SiO_2 biplots used to classify and assess potential correlatives for Lago Pato (LP) volcanic glass shard EPMA data ($n_{unfiltered}$ = 1138; $n_{filtered}$ = 1119; n_{ACID} = 967; n_{RHY} = 644; Supplementary Dataset) compared to key eruptions from the Southern South America volcanoes: A = Aguillera, H = Hudson, MB = Mount Burney, R = Reclus, So = Solipuli; UK = Unknown. TB is Trachybasalt TBA is Basalt-trachy-andesite. Data were filtered to remove totals <97% (<63% SiO_2) <95% (>63% SiO_2) and normalised to 100% on a water-free (H_2O_{TOTAL}) basis. **(C)** Zoom in of **(A).**

Figure S9. (D–G) Overpage.

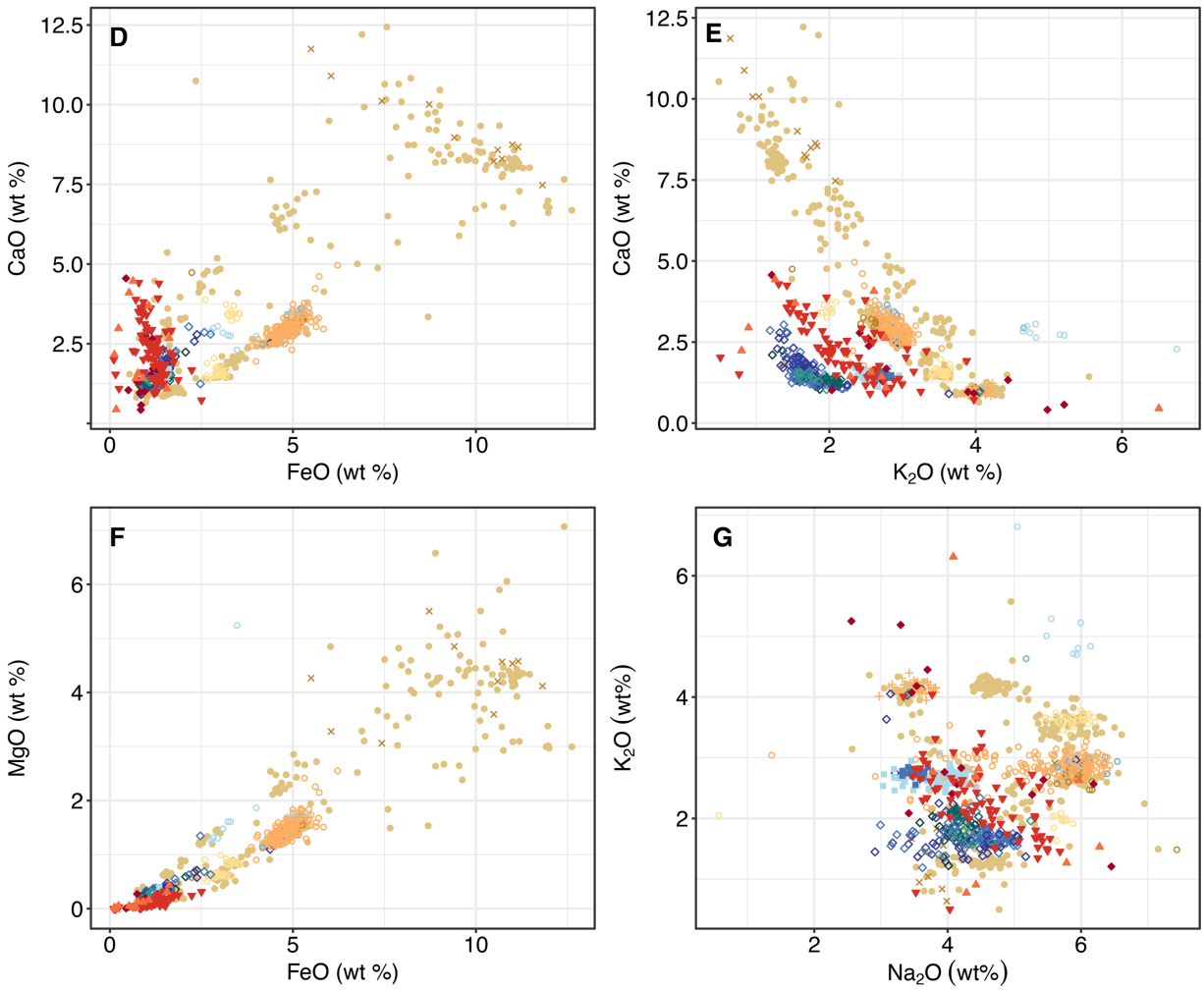

Figure S9 ***contd.*** Elemental biplots used to assess potential correlatives for the Lago Pato tephra EPMA shard data (Table S2) **(D)** CaO/FeO; **(E)** CaO/K_2O; **(F)** Na_2O/ K_2O; **(G)** FeO/TiO_2. Reference data and references can be found at: https://github.com/stever60/Lago_Pato

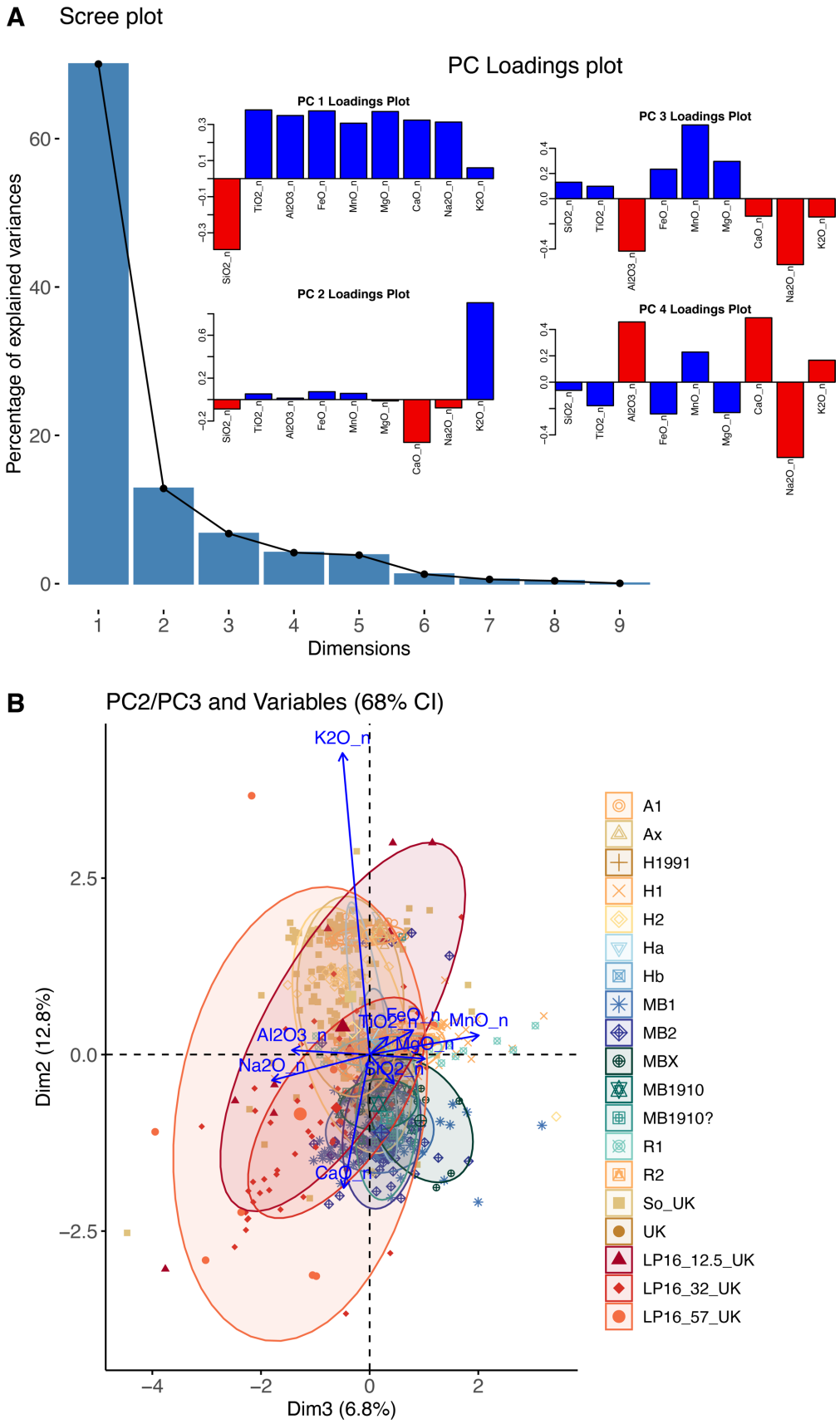

Figure S10. Principal components analysis of data showing: **(A)** Scree plot of variance explained by PC dimensions (axes) 1–9 and PC1–4 loadings. **(B)** PC2/ PC4 biplot of rhyolitic glass shards from Lago Pato (LP) volcanic glass shard EPMA data ($n_{unfiltered}$ = 1,138; $n_{filtered}$ = 1,119; n_{ACID} = 967; n_{RHY} = 644; Supplementary Dataset) compared to key eruptions from the Southern South America volcanoes: A = Aguillera, H = Hudson, MB = Mount Burney, R = Reclus, So = Solipuli; UK = Unknown. Data were filtered to remove totals <95%, normalised to 100%, square root transformed, and standardised and centered.

4. Supplementary Tables

Table S1 Correlation table and figure matrix comparing r^2 values, bi-plots and density distributions of 1 cm resolution, 4 cm interval subsample data and 1 cm resolution matched XRF-CS data for the LP08 record. GRD = GEOTEK-MSCL wet Gamma Ray Density; DW = Dry Weight; TOC_N = Total Organic Carbon undertaken at NIGL; LOI950_c = Loss on Ignition at 950 °C x 1.36 carbonate proxy; % of Total Scatter Normalised Ratio Sum (%TSN) for Ti, Br, and Ca; inc_coh = inc./coh ratio; coh_inc = coh./inc. ratio; TSN_RS = Total Scatter Normalised Ratio Sum. Pearson Correlation Coefficients r values: Corr = whole record; U1 = Unit1 (red), U5 = Unit 5 (green), and U6 (blue) = Unit 6; Significance test: *** p<0.0001; ** p<0.001; * p<0.05; . p<0.1; no symbol p>0.1.

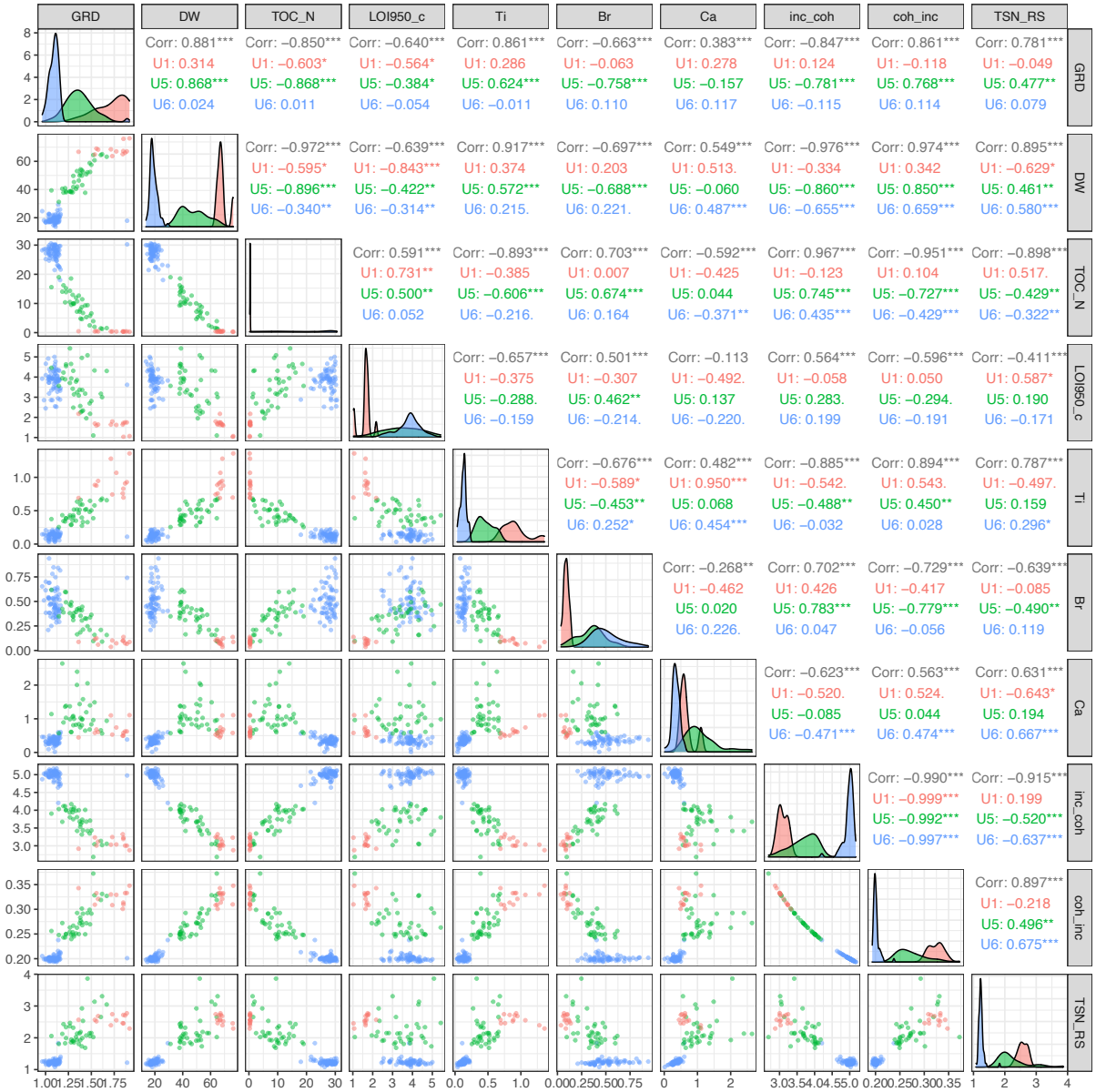

Table S2 Glass shard cryptotephra EPMA data for the Lago Pato LP16 record.

Lab_ID	Size_µm	Na_2O	Al_2O_3	MgO	SiO_2	K_2O	CaO	FeO	P_2O_5	TiO_2	MnO	Total
LP16_12.45	63-125	3.36	11.40	0.14	74.28	3.98	0.92	0.78	0.02	0.13	0.03	95.05
LP16_12.45	63-125	3.31	11.46	0.14	74.72	3.89	0.96	0.90	0.02	0.14	0.02	95.58
LP16_12.45	63-125	3.16	11.53	0.06	74.79	4.98	0.41	0.81	0.05	0.14	0.03	95.98
LP16_12.45	63-125	3.69	14.34	0.06	74.92	4.44	1.33	0.79	0.04	0.15	0.03	99.78
LP16_12.45	63-125	4.09	13.24	0.27	77.18	2.42	1.68	1.31	0.06	0.20	0.04	100.48
LP16_12.45	63-125	2.54	11.23	0.09	78.22	5.21	0.57	0.85	0.06	0.39	0.03	99.18
LP16_12.45	63-125	5.31	16.50	0.20	72.34	2.42	2.78	0.98	0.13	0.21	0.04	100.91
LP16_12.45	125-250	4.10	12.04	0.11	77.21	2.54	1.50	1.10	0.07	0.24	0.04	98.94
LP16_12.45	125-250	6.48	19.48	0.01	67.96	1.21	4.57	0.44	0.06	0.17	0.02	100.39
LP16_12.45	125-250	3.90	11.05	0.27	78.48	2.73	1.29	0.74	0.06	0.22	0.04	98.78
LP16_12.45	125-250	3.33	8.89	0.03	81.44	2.03	1.02	0.49	0.09	0.16	0.00	97.48
LP16_12.45	125-250	5.24	15.94	0.11	68.77	2.54	2.38	1.02	0.11	0.20	0.06	96.36
LP16_12.45	125-250	4.12	13.08	0.10	74.85	2.78	1.68	1.16	0.09	0.18	0.03	98.06
LP16_12.45	125-250	4.82	15.81	0.09	63.19	2.14	3.30	0.76	0.08	0.14	0.03	90.34
LP16_12.45	125-250	6.10	16.22	0.08	69.71	2.53	2.61	1.14	0.06	0.13	0.03	98.63
LP16_32.2	63-125	3.38	11.12	0.07	71.95	2.90	0.96	0.73	0.07	0.18	0.03	91.37
LP16_32.2	63-125	4.39	14.44	0.03	72.18	3.33	2.22	0.61	0.05	0.18	0.02	97.46
LP16_32.2	63-125	5.48	15.23	0.09	72.36	2.24	2.55	0.89	0.05	0.19	0.03	99.11
LP16_32.2	63-125	3.64	10.54	0.08	76.17	2.61	1.21	1.41	0.08	0.25	0.05	96.03
LP16_32.2	63-125	3.46	9.35	0.01	82.67	0.77	1.51	0.15	0.05	0.13	0.00	98.08
LP16_32.2	63-125	3.92	12.50	0.04	74.92	2.24	2.18	0.68	0.07	0.29	0.04	96.87
LP16_32.2	63-125	5.20	16.86	0.05	68.33	1.31	4.29	0.77	0.05	0.22	0.02	97.09
LP16_32.2	63-125	4.90	14.90	0.15	70.73	1.57	3.34	0.88	0.06	0.20	0.05	96.79
LP16_32.2	63-125	4.09	10.53	0.08	77.20	2.56	0.91	1.17	0.07	0.27	0.04	96.91
LP16_32.2	63-125	5.33	16.85	0.06	70.89	1.69	3.62	1.11	0.07	0.23	0.04	99.88
LP16_32.2	63-125	3.67	11.45	0.05	75.23	2.38	1.79	1.46	0.05	0.24	0.03	96.36
LP16_32.2	63-125	3.61	13.65	0.05	71.56	3.88	1.92	0.88	0.06	0.22	0.04	95.87
LP16_32.2	63-125	5.22	16.05	0.00	71.25	2.70	2.74	0.84	0.06	0.21	0.04	99.12
LP16_32.2	63-125	4.45	13.86	0.32	74.72	2.68	1.77	1.48	0.05	0.20	0.05	99.59
LP16_32.2	63-125	3.74	11.03	0.15	77.27	3.25	0.97	1.26	0.06	0.24	0.03	98.00
LP16_32.2	63-125	4.46	14.07	0.05	74.48	3.15	1.59	0.91	0.06	0.18	0.03	98.97
LP16_32.2	125-250	5.15	16.18	0.10	68.79	1.46	3.42	0.82	0.05	0.16	0.02	96.14
LP16_32.2	125-250	3.74	12.74	0.10	73.72	1.98	1.92	1.16	0.07	0.29	0.04	95.76
LP16_32.2	125-250	4.41	12.76	0.13	74.82	2.20	1.65	1.37	0.07	0.28	0.03	97.72
LP16_32.2	125-250	4.60	14.09	0.14	74.38	1.85	2.34	1.09	0.04	0.25	0.02	98.80
LP16_32.2	125-250	3.68	11.63	0.25	78.24	2.33	1.37	1.86	0.06	0.27	0.04	99.74
LP16_32.2	125-250	4.74	13.27	0.22	72.18	1.69	2.83	1.63	0.05	0.26	0.05	96.91
LP16_32.2	125-250	4.39	13.28	0.09	75.21	2.20	2.20	1.20	0.06	0.27	0.04	98.94
LP16_32.2	125-250	4.08	11.55	0.12	78.17	2.61	1.47	1.44	0.07	0.33	0.03	99.88
LP16_32.2	125-250	4.32	12.23	0.14	75.35	2.60	1.37	1.26	0.08	0.34	0.04	97.71
LP16_32.2	125-250	4.66	16.31	0.08	71.79	1.50	3.60	0.83	0.06	0.28	0.03	99.15
LP16_32.2	125-250	4.45	15.15	0.07	72.73	1.91	2.84	0.98	0.05	0.21	0.02	98.41
LP16_32.2	125-250	4.02	10.85	0.19	76.49	2.33	1.30	1.25	0.06	0.25	0.06	96.80
LP16_32.2	125-250	3.37	12.82	0.18	73.21	2.61	2.79	1.48	0.08	0.29	0.03	96.87
LP16_32.2	125-250	3.31	11.10	0.31	76.74	3.98	0.72	2.48	0.08	0.32	0.07	99.12
LP16_32.2	125-250	4.22	14.13	0.10	72.96	1.95	2.62	1.30	0.06	0.22	0.04	97.59
LP16_32.2	125-250	4.72	12.61	0.11	74.63	2.28	1.82	1.40	0.06	0.22	0.05	97.88
LP16_32.2	125-250	3.73	11.03	0.06	76.12	2.42	1.67	1.32	0.07	0.26	0.04	96.71
LP16_32.2	125-250	4.77	13.47	0.17	75.43	1.91	2.15	1.31	0.06	0.25	0.04	99.56
LP16_32.2	125-250	5.02	14.38	0.22	75.05	2.04	2.16	1.75	0.07	0.27	0.04	101.01
LP16_32.2	125-250	5.00	19.14	0.06	66.43	2.49	3.80	0.69	0.05	0.14	0.02	97.82
LP16_32.2	125-250	3.53	10.69	0.03	82.04	2.84	1.10	0.25	0.02	0.06	0.02	100.58
LP16_32.2	125-250	5.18	14.02	0.09	72.47	1.99	2.47	1.04	0.11	0.28	0.05	97.69
LP16_32.2	125-250	5.18	15.07	0.07	71.00	1.76	3.04	0.93	0.07	0.20	0.03	97.34
LP16_32	63-125	4.11	12.52	0.08	74.22	2.38	1.74	1.16	0.07	0.26	0.03	96.57
LP16_32	63-125	5.18	15.33	0.01	71.16	1.64	3.16	0.79	0.07	0.17	0.01	97.52
LP16_32	63-125	4.44	12.71	0.21	72.69	2.18	1.81	1.23	0.07	0.24	0.04	95.62
LP16_32	63-125	4.47	13.00	0.26	72.98	2.08	1.86	1.68	0.08	0.24	0.03	96.67
LP16_32	63-125	5.32	17.27	0.17	66.73	1.42	4.25	1.30	0.06	0.20	0.03	96.74
LP16_32	63-125	3.55	11.87	0.13	76.18	2.89	1.31	1.29	0.06	0.27	0.05	97.60

LP16_32	63-125	3.49	10.95	0.12	75.94	2.95	1.38	1.08	0.04	0.22	0.03	96.20
LP16_32	63-125	4.37	14.93	0.06	72.06	3.07	2.29	1.12	0.06	0.25	0.03	98.24
LP16_32	63-125	4.56	14.67	0.10	73.01	2.04	2.23	1.24	0.08	0.26	0.04	98.22
LP16_32	63-125	5.54	16.84	0.07	68.76	1.42	3.57	0.92	0.06	0.21	0.04	97.44
LP16_32	63-125	4.36	13.67	0.10	72.42	1.84	2.34	1.13	0.06	0.26	0.03	96.22
LP16_32	63-125	3.53	11.97	0.08	76.83	2.62	1.53	1.52	0.09	0.27	0.05	98.48
LP16_32	63-125	3.49	11.80	0.10	74.72	2.21	2.25	1.34	0.07	0.24	0.04	96.24
LP16_32	63-125	4.09	11.06	0.00	83.51	0.51	2.03	0.11	0.02	0.06	0.02	101.37
LP16_32	63-125	3.89	12.81	0.13	73.97	1.95	2.25	1.13	0.07	0.22	0.01	96.42
LP16_32	63-125	4.95	14.17	0.08	69.49	2.12	2.49	0.88	0.04	0.13	0.02	94.37
LP16_32	63-125	5.19	15.72	0.04	69.14	2.44	2.92	0.96	0.05	0.15	0.03	96.66
LP16_32	63-125	4.25	12.38	0.12	73.48	2.99	1.20	1.21	0.08	0.22	0.03	95.97
LP16_32	63-125	4.36	13.14	0.09	74.01	2.65	1.67	1.37	0.07	0.32	0.04	97.73
LP16_32	125-250	5.35	15.96	0.06	69.71	1.46	3.72	0.90	0.07	0.27	0.02	97.51
LP16_32	125-250	4.10	11.93	0.10	75.89	2.52	1.42	1.33	0.07	0.29	0.05	97.70
LP16_32	125-250	4.37	14.77	0.11	74.42	2.12	2.44	1.19	0.07	0.24	0.06	99.78
LP16_32	125-250	4.99	15.81	0.08	70.73	1.79	3.34	0.87	0.04	0.14	0.02	97.81
LP16_32	125-250	4.39	13.68	0.08	74.97	2.41	2.03	1.12	0.06	0.26	0.04	99.04
LP16_32	125-250	3.48	11.40	0.17	76.33	2.75	1.31	1.30	0.07	0.24	0.02	97.07
LP16_32	125-250	4.64	14.10	0.19	73.84	2.10	1.48	1.38	0.06	0.25	0.05	98.09
LP16_32	125-250	4.08	12.26	0.18	72.90	2.00	2.11	1.58	0.06	0.26	0.04	95.46
LP16_32	125-250	3.52	10.52	0.09	75.80	2.77	0.94	1.19	0.07	0.29	0.04	95.23
LP16_32	125-250	4.61	16.95	0.23	69.55	1.96	3.88	1.30	0.05	0.17	0.03	98.73
LP16_32	125-250	4.69	14.78	0.07	73.28	2.49	2.61	0.95	0.05	0.21	0.03	99.18
LP16_32	125-250	4.03	13.72	0.11	74.13	3.05	2.03	1.03	0.07	0.28	0.03	98.48
LP16_32	125-250	3.57	10.30	0.09	76.04	2.50	1.17	1.37	0.07	0.29	0.05	95.46
LP16_32	125-250	5.29	14.09	0.06	74.51	2.01	2.22	1.04	0.07	0.27	0.04	99.58
LP16_32	125-250	3.68	11.74	0.10	64.65	1.84	1.67	1.16	0.06	0.19	0.03	85.13
LP16_32	125-250	4.09	14.31	0.17	72.31	2.05	2.34	1.15	0.05	0.17	0.05	96.68
LP16_32	125-250	5.38	15.97	0.08	69.90	1.62	2.86	1.11	0.05	0.20	0.02	97.19
LP16_32	125-250	4.01	12.84	0.24	74.70	2.64	1.66	2.21	0.08	0.39	0.07	98.83
LP16_32	125-250	5.27	15.27	0.09	70.58	1.67	3.31	0.97	0.06	0.18	0.03	97.43
LP16_32	125-250	5.02	15.23	0.26	71.60	2.60	2.50	1.29	0.06	0.22	0.06	98.83
LP16_32	125-250	5.25	15.72	0.07	69.89	1.58	3.40	0.75	0.05	0.14	0.02	96.86
LP16_32	125-250	4.94	15.25	0.05	65.87	1.38	3.19	1.04	0.08	0.17	0.02	91.99
LP16_57	63-250	4.46	13.32	0.12	77.69	2.72	1.43	0.92	0.08	0.22	0.03	100.99
LP16_57	63-250	4.35	13.50	0.13	76.98	2.57	1.58	0.77	0.09	0.22	0.03	100.21
LP16_57	63-250	3.78	11.48	0.31	78.70	2.77	1.09	1.56	0.09	0.25	0.06	100.10
LP16_57	63-250	4.35	11.94	0.03	81.03	2.29	1.44	0.72	0.07	0.10	0.02	101.99
LP16_57	63-250	4.43	12.69	0.02	83.04	0.80	2.24	0.13	0.01	0.07	0.00	103.42
LP16_57	63-250	4.21	15.66	0.02	75.96	6.50	0.45	0.18	0.02	0.08	0.00	103.04
LP16_57	63-250	4.37	13.49	0.05	76.55	0.90	2.94	0.23	0.07	0.07	0.01	98.67
LP16_57	63-250	5.73	17.91	0.02	69.02	1.26	4.43	0.63	0.04	0.08	0.02	99.14
LP16_57	63-250	5.93	19.56	0.05	66.39	2.61	4.07	0.52	0.06	0.13	0.01	99.33
LP16_57	63-250	4.38	15.93	0.43	70.13	2.77	2.62	1.59	0.06	0.15	0.08	98.14
LP16_57	63-250	6.29	17.87	0.16	69.28	1.54	3.70	1.06	0.05	0.11	0.07	100.14
LP16_57	63-250	4.82	14.94	0.05	66.35	3.42	2.88	0.65	0.08	0.14	0.02	93.37

5. Supplementary References

Bennion, H., Sayer, C.D., Tibby, J., Carrick, H.J., Smol, J.P., and Stoermer, E.F. (2010). "Diatoms as indicators of environmental change in shallow lakes," in *The Diatoms,* eds. E.F. Stoermer & J.P. Smol. 2 ed (Cambridge: Cambridge University Press), 152-173.

Bertrand, S., Araneda, A., Vargas, P., Jana, P., Fagel, N., and Urrutia, R. (2012). Using the N/C ratio to correct bulk radiocarbon ages from lake sediments: Insights from Chilean Patagonia. *Quaternary Geochronology* 12**,** 23-29.

Bishop, T. (2021). itraxR: Itrax Data Analysis Tools. *https://CRAN.R-project.org/package = itraxR*.

Blaauw, M., and Christen, J.A. (2011). Flexible paleoclimate age-depth models using an autoregressive gamma process. *Bayesian Analysis* 6**,** 457-474.

Blaikie, J. (2020). *Palaeoenvironmental reconstruction of Late Glacial-Holocene environmental change for Patagonia, southern South America. Unpublished PhD thesis.* PhD.

Brown, E.T. (2011). Lake Malawi's response to "megadrought" terminations: Sedimentary records of flooding, weathering and erosion. *Palaeogeography, Palaeoclimatology, Palaeoecology* 303**,** 120-125.

Campos, H., Soto, D., Parra, O., Steffen, W., and Aguero, G. (1995). Limnological studies of Amarga Lagoon, Chile: A saline lake in Patagonian South America. *International Journal of Salt Lake Research* 4**,** 301-314.

Croudace, I.W., Rindby, A., and Rothwell, R.G. (2006). "ITRAX:descriptions and evealuation of new mulitfunction X-ray scanner," in *New Techniques in Sediment Core Analysis,* ed. R.G. Rothwell. G), 51-63.

Davies, B.J., Darvill, C.M., Lovell, H., Bendle, J.M., Dowdeswell, J.A., Fabel, D., García, J.-L., Geiger, A., Glasser, N.F., Gheorghiu, D.M., Harrison, S., Hein, A.S., Kaplan, M.R., Martin, J.R.V., Mendelova, M., Palmer, A., Pelto, M., Rodés, Á., Sagredo, E.A., Smedley, R.K., Smellie, J.L., and Thorndycraft, V.R. (2020). The evolution of the Patagonian Ice Sheet from 35 ka to the present day (PATICE). *Earth-Science Reviews* 204**,** 103152.

Davies, S.J., Lamb, H.F., and Roberts, S.J. (2015). "Micro-XRF Core Scanning in Palaeolimnology: Recent Developments," in *Micro-XRF Studies of Sediment Cores,* eds. I.W. Croudace & R.G. Rothwell. (Dordrecht: Springer Netherlands), 189-226.

Einarsson, Á., Stefánsdóttir, G., Jóhannesson, H., Ólafsson, J.S., Már Gíslason, G., Wakana, I., Gudbergsson, G., and Gardarsson, A. (2004). The ecology of Lake Myvatn and the River Laxá: Variation in space and time. *Aquatic Ecology* 38**,** 317-348.

Farias, M.E., Contreras, M., Rasuk, M.C., Kurth, D., Flores, M.R., Poire, D.G., Novoa, F., and Visscher, P.T. (2014). Characterization of bacterial diversity associated with microbial mats, gypsum evaporites and carbonate microbialites in thalassic wetlands: Tebenquiche and La Brava, Salar de Atacama, Chile. *Extremophiles* 18**,** 311-329.

Finkelstein, S.A., and Gajewski, K. (2008). Responses of Fragilarioid-dominated diatom assemblages in a small Arctic lake to Holocene climatic changes, Russell Island, Nunavut, Canada. *Journal of Paleolimnology* 40**,** 1079-1095.

Fontijn, K., Lachowycz, S.M., Rawson, H., Pyle, D.M., Mather, T.A., Naranjo, J.A., and Moreno-Roa, H. (2014). Late Quaternary tephrostratigraphy of southern Chile and Argentina. *Quaternary Science Reviews* 89**,** 70-84.

García, J.-L., Hall, B.L., Kaplan, M.R., Vega, R.M., and Strelin, J.A. (2014). Glacial geomorphology of the Torres del Paine region (southern Patagonia): Implications for glaciation, deglaciation and paleolake history. *Geomorphology* 204**,** 599-616.

Grimm, E.C. (1987). CONISS: a FORTRAN 77 program for stratigraphically constrained cluster analysis by the method of incremental sum of squares. *Computers & Geosciences* 13**,** 13-35.

Grimm, E.C., Maher Jr, L.J., and Nelson, D.M. (2009). The magnitude of error in conventional bulk-sediment radiocarbon dates from central North America. *Quaternary Research* 72**,** 301-308.

Grinsted, A., Moore, J.C., and Jevrejeva, S. (2004). Application of the cross wavelet transform and wavelet coherence to geophysical time series. *Nonlinear Processes in Geophysics* 11**,** 561-566.

Guerrero, J.M., and Echenique, R.O. (2002). Cyclostephanos Patagonicussp. Nov., a New Freshwater Diatom from Western Patagonia (Argentina). *Diatom Research* 17**,** 141-151.

Gunn, D.E., and Best, A.I. (1998). A new automated nondestructive system for high resolution multi-sensor core logging of open sediment cores. *Geo-Marine Letters* 18**,** 70-77.

Hodell, D.A., Turchyn, A.V., Wiseman, C.J., Escobar, J., Curtis, J.H., Brenner, M., Gilli, A., Mueller, A.D., Anselmetti, F., Ariztegui, D., and Brown, E.T. (2012). Late Glacial temperature and precipitation changes in the lowland Neotropics by tandem measurement of δ18O in biogenic carbonate and gypsum hydration water. *Geochimica et Cosmochimica Acta* 77**,** 352-368.

Hodgson, D.A., Roberts, S.J., Bentley, M.J., Carmichael, E.L., Smith, J.A., Verleyen, E., Vyverman, W., Geissler, P., Leng, M.J., and Sanderson, D.C.W. (2009). Exploring former subglacial Hodgson Lake, Antarctica. Paper II: palaeolimnology. *Quaternary Science Reviews* 28**,** 2310-2325.

Hogg, A.G., Heaton, T.J., Hua, Q., Palmer, J.G., Turney, C.S.M., Southon, J., Bayliss, A., Blackwell, P.G., Boswijk, G., Bronk Ramsey, C., Pearson, C., Petchey, F., Reimer, P., Reimer, R., and Wacker, L. (2020). SHCal20 Southern Hemisphere Calibration, 0–55,000 Years cal BP. *Radiocarbon* 62**,** 759-778.

Hua, Q., Barbetti, M., and Rakowski, A.Z. (2013). Atmospheric radiocarbon for the period 1950-2010. *Radiocarbon* 55**,** 1–14.

Jouve, G., Francus, P., Lamoureux, S., Provencher-Nolet, L., Hahn, A., Haberzettl, T., Fortin, D., and Nuttin, L. (2013). Microsedimentological characterization using image analysis and μ-XRF as indicators of sedimentary processes and climate changes during Lateglacial at Laguna Potrok Aike, Santa Cruz, Argentina. *Quaternary Science Reviews* 71**,** 191-204.

Juggins, S. (2007). "C2 Version 1.5 User Guide. Software for ecological and palaeoecological data analysis and visualisation". (Newcastle University).

Juggins, S. (2012). Rioja: Analysis of Quaternary Science Data, R package version (0.8-5).

Kylander, M.E., Ampel, L., Wohlfarth, B., and Veres, D. (2011). High-resolution X-ray fluorescence core scanning analysis of Les Echets (France) sedimentary sequence: new insights from chemical proxies. *Journal of Quaternary Science* 26**,** 109-117.

Lauterbach, S., Brauer, A., Andersen, N., Danielopol, D.L., Dulski, P., Hüls, M., Milecka, K., Namiotko, T., Obremska, M., and Von Grafenstein, U. (2011). Environmental responses to Lateglacial climatic fluctuations recorded in the sediments of pre-Alpine Lake Mondsee (northeastern Alps). *Journal of Quaternary Science* 26**,** 253-267.

Löwemark, L., Chen, H.F., Yang, T.N., Kylander, M., Yu, E.F., Hsu, Y.W., Lee, T.Q., Song, S.R., and Jarvis, S. (2011). Normalizing XRF-scanner data: A cautionary note on the interpretation of high-resolution records from organic-rich lakes. *Journal of Asian Earth Sciences* 40**,** 1250-1256.

Mansilla, C.A., Mcculloch, R.D., and Morello, F. (2016). Palaeoenvironmental change in Southern Patagonia during the Lateglacial and Holocene: Implications for forest refugia

and climate reconstructions. *Palaeogeography, Palaeoclimatology, Palaeoecology* 447**,** 1-11.

Mansilla, C.A., Mcculloch, R.D., and Morello, F. (2018). The vulnerability of the Nothofagus forest-steppe ecotone to climate change: Palaeoecological evidence from Tierra del Fuego (~53°S). *Palaeogeography, Palaeoclimatology, Palaeoecology* 508**,** 59-70.

Mcculloch, R.D., Bentley, M.J., Tipping, R.M., and Clapperton, C.M. (2005). Evidence for late-glacial ice dammed lakes in the central Strait of Magellan and Bahia Inutil, southernmost South America. *Geografiska Annaler Series a-Physical Geography* 87A**,** 335-362.

Mcculloch, R.D., Blaikie, J., Jacob, B., Mansilla, C.A., Morello, F., De Pol-Holz, R., San Román, M., Tisdall, E., and Torres, J. (2020). Late glacial and Holocene climate variability, southernmost Patagonia. *Quaternary Science Reviews* 229**,** 106131.

Mcculloch, R.D., and Davies, S.J. (2001). Late-glacial and Holocene palaeoenvironmental change in the central Strait of Magellan, southern Patagonia. *Palaeogeography Palaeoclimatology Palaeoecology* 173**,** 143-173.

Mcculloch, R.D., Figuerero Torres, M.J., Mengoni Goñalons, G.L., Barclay, R., and Mansilla, C. (2017). A Holocene record of environmental change from Río Zeballos, central Patagonia. *The Holocene* 27**,** 941-950.

Mcculloch, R.D., Mansilla, C.A., Martin, F., Borrero, L., Staff, R.A., and Tisdall, E.W. (2021). The nature and timing of landscape change at Cerro Benítez, Última Esperanza, southern Patagonia (52°S): New insights into the history of megafaunal extinctions and human occupation. *Quaternary International* 601**,** 116-129.

Mcculloch, R.D., Mansilla, C.A., Morello, F., De Pol-Holz, R., San Román, M., Tisdall, E., and Torres, J. (2019). Late glacial and Holocene landscape change and rapid climate and coastal impacts in the Canal Beagle, southernmost Patagonia. *Journal of Quaternary Science* 34**,** 674-684.

Melles, M., Brigham-Grette, J., Minyuk, P.S., Nowaczyk, N.R., Wennrich, V., Deconto, R.M., Anderson, P.M., Andreev, A.A., Coletti, A., Cook, T.L., Haltia-Hovi, E., Kukkonen, M., Lozhkin, A.V., Rosen, P., Tarasov, P., Vogel, H., and Wagner, B. (2012). 2.8 million years of Arctic climate change from Lake El'gygytgyn, NE Russia. *Science* 337**,** 315-320.

Mueller, A.D., Islebe, G.A., Hillesheim, M.B., Grzesik, D.A., Anselmetti, F.S., Ariztegui, D., Brenner, M., Curtis, J.H., Hodell, D.A., and Venz, K.A. (2017). Climate drying and associated forest decline in the lowlands of northern Guatemala during the late Holocene. *Quaternary Research* 71**,** 133-141.

Oksanen, J. (2014). "Vegan: Community Ecology Package. R package version 2.3-0.". (http://cran.r-project.org/web/packages/vegan/index.html).

Olsen, J., Anderson, N.J., and Leng, M.J. (2013). Limnological controls on stable isotope records of late-Holocene palaeoenvironment change in SW Greenland: a paired lake study. *Quaternary Science Reviews* 66**,** 85-95.

Ramsey, C.B. (2009). Bayesian Analysis of Radiocarbon Dates. *2009***,** 24.

Roberts, S.J., Monien, P., Foster, L.C., Loftfield, J., Hocking, E.P., Schnetger, B., Pearson, E.J., Juggins, S., Fretwell, P., Ireland, L., Ochyra, R., Haworth, A.R., Allen, C.S., Moreton, S.G., Davies, S.J., Brumsack, H.J., Bentley, M.J., and Hodgson, D.A. (2017). Past penguin colony responses to explosive volcanism on the Antarctic Peninsula. *Nat Commun* 8**,** 14914.

Rothwell, R.G., and Croudace, I.W. (2015). "Micro-XRF Studies of Sediment Cores: A Perspective on Capability and Application in the Environmental Sciences," in *Micro-XRF Studies of Sediment Cores,* eds. I.W. Croudace & R.G. Rothwell. (Dordrecht: Springer Netherlands), 1-21.

Rumrich, U., Lange-Bertalot, H., and Rumrich, M. (2000). Diatoms of the Andes: from Venezuela to Patagonia/Tierra del Fuego. *Iconographia Diatomologica* 9.

Sagredo, E.A., Moreno, P.I., Villa-Martínez, R., Kaplan, M.R., Kubik, P.W., and Stern, C.R. (2011). Fluctuations of the Última Esperanza ice lobe (52°S), Chilean Patagonia, during the last glacial maximum and termination 1. *Geomorphology* 125**,** 92-108.

Saunders, K.M., Roberts, S.J., Perren, B., Butz, C., Sime, L., Davies, S., Van Nieuwenhuyze, W., Grosjean, M., and Hodgson, D.A. (2018). Holocene dynamics of the Southern Hemisphere westerly winds and possible links to CO2 outgassing. *Nature Geoscience* 11**,** 650-655.

Smith, R.E., Smith, V.C., Fontijn, K., Gebhardt, A.C., Wastegård, S., Zolitschka, B., Ohlendorf, C., Stern, C., and Mayr, C. (2019). Refining the Late Quaternary tephrochronology for southern South America using the Laguna Potrok Aike sedimentary record. *Quaternary Science Reviews* 218**,** 137-156.

Solari, M.A., Le Roux, J.P., Herve, F., Airo, A., and Calderon, M. (2012). Evolution of the Great Tehuelche Paleolake in the Torres del Paine National Park of Chilean Patagonia during the Last Glacial Maximum and Holocene. *Andean Geology* 39**,** 1-21.

Stern, C., Moreno, P., Henríquez, W., Villa-Martínez, R., Sagredo, E., Aravena, J., and De Pol-Holz, R. (2015). Holocene tephrochronology around Cochrane (~47° S), southern Chile. *Andean Geology* 43**,** 1-19.

Stevenson, R.J., Pan, Y., Stoermer, E.F., and Smol, J.P. (1999). "Assessing environmental conditions in rivers and streams with diatoms," in *The Diatoms,* eds. E.F. Stoermer & J.P. Smol. (Cambridge: Cambridge University Press), 11-40.

Stevenson, R.J., Pan, Y., Van Dam, H., Smol, J.P., and Stoermer, E.F. (2010). "Assessing environmental conditions in rivers and streams with diatoms," in *The Diatoms,* eds. E.F. Stoermer & J.P. Smol. 2 ed (Cambridge: Cambridge University Press), 57-85.

Wennrich, V., Minyuk, P.S., Borkhodoev, V., Francke, A., Ritter, B., Nowaczyk, N.R., Sauerbrey, M.A., Brigham-Grette, J., and Melles, M. (2014). Pliocene to Pleistocene climate and environmental history of Lake El'gygytgyn, Far East Russian Arctic, based on high-resolution inorganic geochemistry data. *Climate of the Past* 10**,** 1381-1399.

Westover, K.S., Fritz, S.C., Blyakharchuk, T.A., and Wright, H.E. (2006). Diatom Paleolimnological Record of Holocene Climatic and Environmental Change in the Altai Mountains, Siberia. *Journal of Paleolimnology* 35**,** 519-541.

Wilhelms-Dick, D., Westerhold, T., Röhl, U., Wilhelms, F., Vogt, C., Hanebuth, T.J.J., Römmermann, H., Kriews, M., and Kasten, S. (2012). A comparison of mm scale resolution techniques for element analysis in sediment cores. *Journal of Analytical Atomic Spectrometry* 27**,** 1574-1584.